ALMA MATER STUDIORUM
UNIVERSITÀ DI BOLOGNA

DEPARTMENT OF PHYSICS AND ASTRONOMY "A. RIGHI"

SECOND CYCLE DEGREE

PHYSICS

# Lowest Order Constrained Variational approximation for ultracold Bose-Fermi mixtures

Supervisor
Prof. Pierbiagio Pieri

Co-supervisor
Dr. Leonardo Pisani

Defended by
Pietro Cordioli

---

Graduation Session July/2025

Academic Year 2024/2025

# Abstract

In this thesis, we investigate ultracold Bose-Fermi mixtures in both two and three dimensions using a non-perturbative approach based on the Lowest Order Constrained Variational (LOCV) method. This variational technique, originally developed in the context of nuclear matter, is applied here to dilute quantum gases at zero temperature, allowing for an accurate treatment of two-body correlations beyond perturbative limits.

We begin by analysing Bose-Fermi mixtures near a broad Fano-Feshbach resonance, which enables precise tuning of the interspecies interaction strength. Particular attention is devoted to the low-dimensional case, where quantum fluctuations are enhanced and experimental realizations have become increasingly accessible. While the three-dimensional problem serves as a useful benchmark, the two-dimensional Bose-Fermi mixture presents unique challenges. Notably, no prior non-perturbative studies exist on its mechanical stability.

A central goal of this work is to determine the conditions under which the 2D Bose-Fermi mixture remains mechanically stable as the boson-fermion attraction is increased. Our results demonstrate that the LOCV approach captures the relevant physics from weak to moderate coupling, offering a complementary perspective to perturbative methods or alternative non-perturbative approaches such as the T-matrix formalism. In this coupling range, we identify the critical strength of boson-boson repulsion necessary to prevent phase separation or collapse, thereby providing the first theoretical variational prediction of a stability phase diagram in this two dimensional regime.

Overall, this work fills a gap in the literature and provides a useful reference point for future theoretical and experimental studies of strongly interacting Bose-Fermi systems in reduced dimensionality.

# Contents

# Introduction

At the beginning of the last century, brilliant minds such as Albert Einstein, Max Planck, among others, ignited the rise of a revolutionary theory in physics: quantum mechanics. Our established deterministic conception of reality was challenged by concepts such as wave-functions, superposition of states and quantum statistics. The effects of these new ideas usually defy human classical expectations. A branch of modern physics densely populated by quantum phenomena is condensed matter physics, displaying, just to cite a few, superconductivity and superfluidity. The reason being, matter is made up of a huge number of particles, which are fully quantum, interacting with each other in a vast variety of ways.

Depending on their intrinsic angular momentum, called spin, particles are classified into into *bosons* or *fermions*, as a direct consequence of quantum mechanics. Bosons, possessing integer spin, obey Bose-Einstein statistics and can macroscopically occupy the ground state at the same time, leading to *Bose-Einstein condensation* below a critical temperature [1]. Fermions, with half-integer spin, are subject to the *Pauli exclusion principle*, which forbids multiple particles from sharing the same quantum state, giving rise to Fermi degeneracy pressure and the structure of atomic matter itself [2].

With the advent of the possibility of experimenting with *ultracold atomic gases*, it has become possible to realize idealized quantum systems in laboratory settings [3, 4]. New techniques such as laser or evaporative cooling enables temperatures in the nano-Kelvin regime, where quantum statistical effects dominate. One of the most powerful tools in this field is the *Fano-Feshbach resonance* [3], which allows experimentalists to tune interatomic interactions by adjusting an external magnetic field. This precise control has opened up rich possibilities for studying *strongly interacting Bose-Fermi mixtures* [5, 6, 7, 8, 9], where bosons and fermions coexist and influence each other's dynamics.

At low-temperature and in the dilute limit, the interactions between atoms can be effectively described by a single parameter, the *s-wave scattering length*, which encapsulates the low-energy behaviour of two-body collisions [4, 10]. A proper theoretical framework for describing such systems must account for both quantum statistics and the non-trivial correlations induced by interactions.

Many approaches exist for modelling interacting mixtures, such as *perturbative expansions* [2], the T-matrix formalism [11, 12, 9] and quantum Monte Carlo methods [13, 14, 15, 16, 6, 8]. In this thesis, we adopt a *non-perturbative* approach: the *Lowest Order Constrained Variational (LOCV)* method. Originally developed in the context of nuclear matter [17, 18], and now applied to ultracold atomic mixtures [19, 20, 21, 22, 5]. The LOCV method is a first approximation to a fully ab-initio non perturbative approach, such as quantum Monte Carlo. LOCV captures two-body correlations through a variational principle, allowing one to obtain meaningful results even in the strongly interacting regime, while remaining computationally efficient.

Specifically, we apply the LOCV method to the study of *Bose-Fermi mixtures* in both *three* and *two dimensions*. The three-dimensional case has been widely studied and offers a solid benchmark for our results [5, 6, 12, 7, 9]. The two-dimensional case, especially concerning the *mechanical stability* of the mixture remains instead largely unexplored [8]. This thesis aims to fill that gap by providing, to the best of our knowledge, the first non-perturbative analysis of the stability of 2D Bose-Fermi mixtures, with results that may inform and guide future experimental and theoretical investigations.

The structure of the thesis is as follows:

- **Chapter 1** introduces ultracold quantum gases and provides an overview of quantum scattering theory, focusing on s-wave scattering and the definition of the scattering length as a key parameter; moreover the physics of Fano-Feshbach resonances is clarified, emphasizing their role in tuning interspecies interactions.

- **Chapter 2** develops the formalism of the LOCV method, detailing its application to interacting Bose-Fermi systems.

- **Chapter 3** presents the results obtained for the Bose-Fermi mixtures in both 3D and 2D geometries, with particular attention to the conditions under which the B-F mixtures remain stable.

- **Conclusions and Perspectives**

# Chapter 1

# Ultracold atomic gases and scattering theory

## 1.1 General properties

The field of ultracold atomic physics has opened a unique window into the quantum world, enabling unprecedented control over atomic systems at nanokelvin temperatures. When the temperature of an atomic gas is lowered below approximately $1\,\mu$K, the thermal de Broglie wavelength of the atoms becomes comparable to or larger than the average inter-particle separation, and quantum effects begin to dominate the system's behaviour [1]. In this regime, classical Maxwell-Boltzmann statistics fail to provide an accurate description, and one must instead resort to quantum statistics appropriate for bosons and fermions.

In a Bose gas, composed of atoms with integer spin, the indistinguishability of particles and the absence of the Pauli exclusion principle allow a macroscopic number of atoms to occupy the lowest energy state. Below a critical temperature, this results in Bose-Einstein condensation (BEC), a purely quantum phenomenon characterized by the formation of a coherent macroscopic wave-function. In contrast, fermionic atoms (with half-integer spin) are subject to the Pauli exclusion principle, which forbids them from occupying the same quantum state. At low temperatures, fermions fill all available single-particle states up to the Fermi energy, forming a degenerate Fermi gas.

The behaviour of ultracold gases is governed by three fundamental length scales: the *thermal de Broglie wavelength*

$$\lambda_T = \sqrt{\frac{2\pi}{mT}},$$

which characterizes the spatial extent of a quantum wave-packet; the *average inter-particle distance* $l \sim n^{-1/D}$, where $n$ is the particle density and $D$ the dimensionality; and the *interaction range* $r_0$, determined by the specifics of the interatomic potential. Throughout this work, we set $\hbar = 1$ for simplicity. Quantum degeneracy is achieved when $\lambda_T \gtrsim l$, and a gas can be considered dilute when $r_0 \ll l$, ensuring that two-body interactions dominate and the system remains gaseous rather than crystallizing [23].

In the dilute limit, where $r_0 \ll l$ and $r_0 \ll \lambda_T$, a remarkable simplification arises: the microscopic details of the interatomic potential become irrelevant, and the interaction between atoms can be effectively described by a *contact potential*. In this case, the dominant contribution to low-energy scattering comes from the s-wave channel, and the interaction can be fully characterized by a single parameter, called *s-wave scattering length* $a$ [10]. This universality is one of the most powerful features of ultracold atomic gases and underpins much of the theoretical work in the field.

At ultracold temperatures, interatomic collisions are well-described by two-body scattering processes, since the inter-particle spacing is much larger than the range of the interaction. The internal states of the atoms, including spin, hyperfine level, and species identity, define a scattering *channel*, and interactions often involve multiple such channels. Of particular interest are *Feshbach resonances* [4], which occur when a bound state in a closed channel becomes resonant with the scattering threshold of an open channel. The result is a strong modification of the scattering amplitude in the open channel.

These *Fano-Feshbach resonances* are a cornerstone of modern cold atom experiments. They enable the experimental tuning of the interaction strength, including the sign and magnitude of the scattering length, through external magnetic fields. This control allows the exploration of a wide range of interaction regimes, from weak coupling to the strongly interacting regime, and plays a crucial role in the study of Bose-Fermi mixtures. In particular, the ability to access both attractive and repulsive interactions with high precision makes it possible to engineer and probe new quantum phases of matter in both three and two dimensions.

In what follows, we will present a more detailed discussion of quantum scattering theory in both 3D and 2D, with an emphasis on the role of the scattering length as an effective parameter. We will then examine the mechanism and theoretical description of Fano-Feshbach resonances, setting the stage for the application of variational methods to interacting Bose-Fermi mixtures in subsequent chapters.

## 1.2 3D scattering theory

Understanding interactions between particles at low energy is essential for describing ultracold atomic systems. In this context, scattering theory provides a powerful framework for analysing how particles interact, especially when the energy of the system is sufficiently low that only a few partial waves contribute significantly to the scattering process. In the ultracold regime, the s-wave ($\ell = 0$) scattering channel dominates due to the suppression of higher angular momentum contributions.

### 1.2.1 Scattering wave function and scattering amplitude

We begin by considering two particles of mass $m_1$ and $m_2$ interacting via a central potential $V(\vec{r})$. Moving to the center of mass frame, the problem reduces to the motion of a particle with reduced mass $m_r = \frac{m_1 m_2}{m_1+m_2}$ in the potential $V(\vec{r})$. The time-independent Schrödinger equation for the relative motion is then

$$\left[-\frac{1}{2m_r}\nabla^2 + V(\vec{r})\right]\psi(\vec{r}) = \left[H_0 + V(\vec{r})\right]\psi(\vec{r}) = E\psi(\vec{r}), \tag{1.1}$$

where $E$ is the energy of the relative motion and $H_0 = -\frac{1}{2m_r}\nabla^2$. We are interested in elastic processes, we can thus fix $E = \frac{k^2}{2m_r}$. Assuming a short ranged potential, such that exists a characteristic length $r_0$ above which the potential can be neglected, equation (1.1) becomes the an homogenous Schroedinger equation for every $r > r_0$, whose general solution is given by a superposition of plane waves $\phi_k(\vec{r}) = e^{i\vec{k}\cdot\vec{r}}$ which can be added to any particular solution of the equation.

The formal solution to the Schrödinger equation (1.1) in terms of the Green's function leads us to the integral formulation of the scattering problem. Introducing the free-particle casual Green's function

$$G_0(E, \vec{r}, \vec{r}\,') = \langle\vec{r}|\,\frac{1}{E - H_0 + i\epsilon}\,|\vec{r}\,'\rangle \tag{1.2}$$

one obtains the integral form of the wave-function:

$$\psi_k(\vec{r}) = \phi_k(\vec{r}) + \int d^3r'\, G_0(E, \vec{r}, \vec{r}\,')V(\vec{r}\,')\psi_k(\vec{r}\,'). \tag{1.3}$$

This is the *Lippmann-Schwinger equation*, a fundamental equation of scattering theory that expresses the total wave-function in terms of the incident wave $\phi_k(\vec{r})$ and the effect of the potential through the Green's function.

In 3D the free particle Green's function (1.2), after a contour integration in the complex plane, takes the form

$$G_0(k, \vec{r}, \vec{r}\,') = -\frac{m_r}{2\pi} \frac{e^{ik|\vec{r}-\vec{r}\,'|}}{|\vec{r}-\vec{r}\,'|}, \tag{1.4}$$

where $k = \sqrt{2m_r E}$; thus we can write the particular piece of (1.3) as

$$\int d^3r'\, G_0(E, \vec{r}, \vec{r}\,') V(\vec{r}\,') \psi_k(\vec{r}\,') = -\frac{m_r}{2\pi} \int d^3r'\, \frac{e^{ik|\vec{r}-\vec{r}\,'|}}{|\vec{r}-\vec{r}\,'|} V(\vec{r}\,') \psi_k(\vec{r}\,'). \tag{1.5}$$

We assumed a priori that the potential $V(\vec{r})$ is short ranged, moreover we are interested on the behaviour of the scattering wave-function at distances that are large with respect to this range; therefore we can write the interatomic distance for $r \gg r'$ as:

$$|\vec{r}-\vec{r}\,'| = \sqrt{r^2 - 2\vec{r}\cdot\vec{r}\,' + r'^2} = r\sqrt{1 - \frac{2\vec{r}\cdot\vec{r}\,'}{r^2} + \frac{r'^2}{r^2}} \simeq r - \frac{\vec{r}\cdot\vec{r}\,'}{r}. \tag{1.6}$$

Now we define a scattered wave vector

$$\vec{k}\,' = k\frac{\vec{r}}{r}, \tag{1.7}$$

which has the same magnitude as the incident wave vector $\vec{k}$ (elastic scattering), and which also points from the scatterer to the observer. Then

$$k|\vec{r}-\vec{r}\,'| = kr - \vec{k}\,'\cdot\vec{r}\,' \tag{1.8}$$

Thanks to this, in 3 dimensions, we write the Lippmann-Schwinger equation (1.3) as

$$\psi_k(\vec{r}) = \phi_k(\vec{r}) - \frac{m_r}{2\pi r} e^{ikr} \int d^3r'\, e^{-i\vec{k}\,'\cdot\vec{r}\,'} V(\vec{r}\,') \psi_k(\vec{r}\,'), \tag{1.9}$$

where in the denominator we expanded $|\vec{r}-\vec{r}\,'|$ at lowest order. The integral is now independent of the magnitude of $\vec{r}$ , but depends on its direction through $\vec{k}\,'$. The scattered wave has the form of $e^{ikr}/r$ times a function of the scattering angle, that is, the asymptotic wave-function can be written as

$$\psi_k(\vec{r}) = e^{i\vec{k}\cdot\vec{r}} + \frac{e^{ikr}}{r} f(\vec{k}, \vec{k}\,'), \tag{1.10}$$

where $f(\vec{k}, \vec{k}\,')$ is the *scattering amplitude.* We have obtained the important result that, at distances much larger than the range of the interaction, the total wave-function can be written as the sum of an incoming plane wave and an outgoing spherical wave. Now we understand the presence of $+i\epsilon$ factor in the (1.2), a small negative imaginary factor $-i\epsilon$ would have led to an incoming spherical wave. i.e. a description of the time-reversed scattering process. By comparing (1.9) and (1.10) we can read of an expression for the scattering amplitude

$$f(\vec{k},\vec{k}\,') = -\frac{m_r}{2\pi}\int d^3r'\, e^{-i\vec{k}\,'\cdot\vec{r}\,'}V(\vec{r}\,')\psi_k(\vec{r}\,'). \tag{1.11}$$

### 1.2.2 Partial-wave expansion

To further evaluate the scattering wave function in (1.10), we assume the interacting potential to be spherical thus $V(\vec{r}) = V(r)$, which depends only on the distance between atoms. As a consequence, the elastic scattering amplitude is determined by the magnitude $k$ of the incoming momentum $\vec{k}$ and a single angle $\theta$ with the outgoing momentum $\vec{k}\,'$, i.e $f(\vec{k},\vec{k}\,') = f(k,\theta)$. Therefore we can expand the scattering amplitude using the method of partial wave decomposition:

$$f(k,\theta) = \sum_{\ell=0}^{\infty}(2\ell+1)f_\ell(k)P_\ell(\cos\theta), \tag{1.12}$$

where the factors $f_\ell(k)$ are called partial wave amplitudes, while $P_\ell(x)$ are the Legendre polynomials. To understand the meaning of the partial wave amplitudes $f_\ell(k)$ , we can take advantage of the following identity:

$$e^{i\vec{k}\cdot\vec{r}} = \sum_{\ell=0}^{\infty}(2\ell+1)i^\ell j_\ell(kr)P_\ell(\cos\theta), \tag{1.13}$$

where, by sending $r\to\infty$, we can exploit the asymptotic behaviour of the spherical Bessel function $j_\ell(kr)$:

$$e^{i\vec{k}\cdot\vec{r}} \xrightarrow{r\to\infty} \sum_{\ell=0}^{\infty}(2\ell+1)\left(\frac{e^{ikr}-e^{-i(kr-\pi\ell)}}{2ikr}\right)P_\ell(\cos\theta), \tag{1.14}$$

we have now expressed the plane wave part of (1.10) as a superposition of incoming and outgoing spherical waves. Now by using (1.12) and (1.14) we can rewrite the asymptotic wave-function (1.10) at large $r \gg r_0$ as

$$\begin{aligned}\psi_k(\vec{r}) &\simeq \sum_{\ell=0}^{\infty}(2\ell+1)\left[\left(\frac{e^{ikr}-e^{-i(kr-\pi\ell)}}{2ikr}\right)+\frac{e^{ikr}}{r}f_\ell(k)\right]P_\ell(\cos\theta)\\ &= \sum_{\ell=0}^{\infty}(2\ell+1)\left[\frac{e^{ikr}}{r}(1+2ikf_\ell(k))-\frac{e^{-i(kr-\pi\ell)}}{2ikr}\right]P_\ell(\cos\theta).\end{aligned} \tag{1.15}$$

By looking at this expression we have just shown that the presence of an interaction potential changes the coefficient of the outgoing spherical waves according to:

$$\frac{e^{ikr}}{r} \to (1 + 2ikf_\ell(k))\frac{e^{ikr}}{r}. \tag{1.16}$$

Moreover, due to the conservation of probability flux, the square-modulus of the term $(1 + 2ikf_\ell(k))$ as to be exactly equal to 1, which implies

$$1 + 2ikf_\ell(k) = e^{2i\delta_\ell(k)}, \tag{1.17}$$

for some real number $\delta_\ell(k)$ called *phase shift*.

Summarizing, we have found that at large distances, the scattering process is simply reflected by a phase shift of every outgoing spherical partial wave that composed the incident wave $\phi_k(\vec{r})$. The deal is that in ultracold gases the momentum $k$ of the atoms can be so small that only one partial wave is dominant and all the others can be neglected, since one can show that $\delta_\ell(k) \propto k^{2\ell+1}$ for small $k$. Typical momenta of the atoms scale with the inverse of the thermal de Broglie wavelength $\lambda_T$, if they are bosons, or at least up to $k_F$ if they are fermions; momenta will thus be very small for ultracold gases, and only the partial wave with zero angular momentum ($\ell = 0$) will contribute significantly. As a result the complex details of the interatomic potential can be effectively encoded in a single parameter called *s-wave scattering length*:

$$a = -\lim_{k \longrightarrow 0} \frac{\delta_0(k)}{k} \tag{1.18}$$

This parameter plays a central role in the theoretical description of dilute ultracold gases. It determines the strength and nature (repulsive or attractive) of low-energy interactions, enters the effective contact potential used in many-body theories, and can be tuned experimentally using Fano-Feshbach resonances. In the following chapters, $a$ will appear repeatedly as the key quantity governing the interaction properties of Bose-Fermi mixtures in three dimensions.

## 1.3 Fano-Feshbach Resonances

A central reason for the study of ultracold atomic gases in modern quantum physics lies in the extraordinary degree of experimental control they allow, including the ability to manipulate their interaction strength in a reversible way. The key technique enabling this level of control is the use of *Fano-Feshbach resonances*, which provide a method to tune the $s$-wave scattering length, hence the low-energy effective interaction, via external magnetic fields.

The physical mechanism behind a Feshbach resonance is rooted in the multi-channel nature of atom-atom interactions in alkali gases. Because of the hyperfine coupling between the nuclear and electronic spins, the internal energy levels of two colliding atoms define a variety of spin configurations and each configuration corresponds to a scattering channel. When two atoms collide in a given spin state that is energetically allowed at low energy, we say they are in an *open channel.* Conversely, other spin configurations may support bound states at low energy but not allow free scattering; these are referred to as *closed channels.*

A Feshbach resonance occurs when a bound molecular state in a closed channel becomes energetically close to the scattering threshold of an open channel. Even if the coupling between the channels is weak, such proximity allows for strong mixing of the open and closed channel wave-functions. This mixing drastically modifies the scattering properties, especially the scattering length. What makes this phenomenon experimentally useful is that the energy difference between the closed-channel bound state and the open-channel scattering threshold can be tuned using a magnetic field, provided the two configurations have different magnetic moments.

In this case, the scattering length becomes a function of the applied magnetic field $B$ [4], and near the resonance it can be expressed as

$$a(B) = a_{\text{bg}} \left( 1 - \frac{\Delta}{B - B_0} \right) . \tag{1.19}$$

Here, $a_{\text{bg}}$ is the so-called background scattering length, i.e., the value of the scattering length far from the resonance, $B_0$ is the resonance position where $a(B)$ diverges, and $\Delta$ is the width of the resonance, which characterizes the strength of the coupling between the open and closed channels. This tunability allows one to explore a wide range of interaction regimes, from weakly to strongly interacting gases, and even to reach the so-called unitary limit where $|a| \to \infty$.

Feshbach resonances are typically classified as *broad* or *narrow*, depending on the size of $\Delta$ and the coupling strength. In a broad resonance, the coupling is strong and the closed-channel amplitude is negligible, meaning that the system can be effectively described by a single-channel model with a tunable contact interaction. In contrast, narrow resonances require a more accurate two-channel model, where

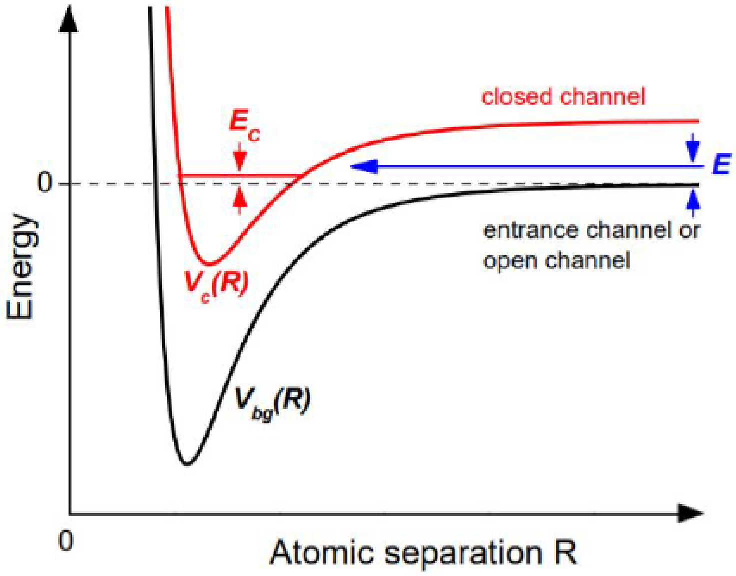

Figure 1.1: Schematic illustration of a magnetically tunable Fano-Feshbach resonance. Two atoms interact via an open channel potential $V_{\mathrm{bg}}(R)$, while a bound state in the closed channel potential $V_c(R)$ lies near the scattering threshold. By tuning the external magnetic field $B$, the energy of the bound state can be shifted to resonate with the open-channel threshold, leading to a strong modification of the scattering length $a(B)$. Figure reproduced from Ref. [3].

the population of the closed-channel molecular state plays an active role in the system's dynamics.

It is also instructive to contrast Feshbach resonances with shape resonances. A shape resonance occurs when a weakly bound state exists in the same potential as the open-channel scattering states. Because the magnetic moments of the colliding atoms and the bound state are the same, a magnetic field cannot shift their relative energy. This makes shape resonances largely inaccessible to magnetic control. In contrast, Feshbach resonances rely on the difference in internal spin states between channels, allowing precise energy tuning of the bound state relative to the continuum, and thus providing a powerful knob to control the interaction strength.

In summary, Fano-Feshbach resonances form the theoretical and experimental backbone of tunable interactions in ultracold atomic systems. By coupling open and closed scattering channels through spin-dependent interactions and tuning their energy separation via an external magnetic field, one can precisely control the $s$-wave scattering length $a(B)$. This ability to engineer interatomic interactions has had far-reaching consequences, enabling studies of strongly correlated phases, molecular condensation, BEC-BCS crossover physics, and beyond.

## 1.4 2D scattering theory

Scattering in two dimensions exhibits a number of striking differences compared to its three-dimensional counterpart, both conceptually and technically. In 3D, the scattering amplitude has a well-defined partial wave expansion, with the low-energy behaviour dominated by the s-wave component and characterized by a single length scale $a$, the scattering length. In 2D, however, the situation is more subtle: the logarithmic behaviour of the Green's function at small distances leads to a qualitatively different structure of the scattering amplitude. As a result, the notion of a scattering length in 2D must be redefined in a way that reflects the logarithmic energy dependence of the amplitude.

Another challenge arises from the fact that bound states are more generic in two dimensions, even an arbitrarily weak attractive potential can support a bound state. This fundamentally alters the threshold behaviour of scattering processes and makes certain approximation schemes less straightforward than in 3D. Moreover, due to the dimensional reduction, the phase shift formalism requires careful reinterpretation.

As we have done in 3D we begin by writing the Schroedinger equation of two bodies with mass $m_1$ and $m_2$ interacting via a central potential $v(\vec{r})$ , in their center of mass frame

$$\left[-\frac{1}{2m_r}\nabla^2 + v(\vec{r})\right]\psi(\vec{r}) = \left[H_0 + v(\vec{r})\right]\psi(\vec{r}) = E\psi(\vec{r}), \tag{1.20}$$

As usual, the equation can be solved using the free particle causal Green's function

$$G_0(E, \vec{r}, \vec{r}\,') = \langle \vec{r}|\, \frac{1}{E - H_0 + i\epsilon}\, |\vec{r}\,'\rangle\,, \tag{1.21}$$

to express the general solution as

$$\psi_k(\vec{r}) = \phi_k(\vec{r}) + \int d^2r'\, G_0(E, \vec{r}, \vec{r}\,')v(\vec{r}\,')\psi_k(\vec{r}\,'); \tag{1.22}$$

recovering the Lippmann-Schwinger equation.

In 2D, after the usual contour integration in the complex plane, the Green function reads:

$$G_0(k, \vec{r}, \vec{r}\,') = \frac{m_r}{2i} H_0^1(k|\vec{r} - \vec{r}\,'|), \tag{1.23}$$

where $H_0^1(x)$ is the Hankel function of the first type B.1.1, while $k = \sqrt{2m_r E}$. Thus the particular piece of (1.22) reads now

$$\int d^2r'\, G_0(E, \vec{r}, \vec{r}\,')v(\vec{r}\,')\psi_k(\vec{r}\,') = \frac{m_r}{2i}\int d^2r'\, H_0^1(k|\vec{r} - \vec{r}\,'|)v(\vec{r}\,')\psi_k(\vec{r}\,'). \tag{1.24}$$

By using the asymptotic expression of the Hankel functions for large $z$

$$H_n^1(z) \xrightarrow{z\to\infty} \sqrt{\frac{2}{\pi z}} e^{i(z-n\frac{\pi}{2}-\frac{\pi}{4})}, \tag{1.25}$$

we can write the asymptotic wave-function as

$$\psi_k(\vec{r}) \simeq e^{i\vec{k}\cdot\vec{r}} + \frac{m_r}{2i}\int d^2r' \sqrt{\frac{2}{\pi k|\vec{r}-\vec{r}\,'|}} e^{i(k|\vec{r}-\vec{r}\,'|-\frac{\pi}{4})} v(\vec{r}\,')\psi_k(\vec{r}\,') \tag{1.26}$$

and finally by using (1.6),(1.7) and (1.8) as we have done in the three dimensional case we get

$$\psi_k(\vec{r}) \simeq e^{i\vec{k}\cdot\vec{r}} - \frac{im_r}{\sqrt{2\pi kr}} e^{i(kr-\frac{\pi}{4})}\int d^2r'\, e^{-i\vec{k}\,'\cdot\vec{r}\,'} v(\vec{r}\,')\psi_k(\vec{r}\,'). \tag{1.27}$$

Again the integral is now independent of the magnitude of $\vec{r}$ , but depends on its direction through $\vec{k}\,'$. The scattered wave has the form of a circular wave $e^{ikr}/\sqrt{r}$ times a function of the scattering angle, that is, for large $r$ the scattered wave function can be written as

$$\psi_k(\vec{r}) = e^{i\vec{k}\cdot\vec{r}} + \frac{e^{ikr}}{\sqrt{r}} f(\vec{k},\vec{k}\,'), \tag{1.28}$$

where $f(\vec{k},\vec{k}\,')$ is the 2D scattering amplitude, which as we explained for the $3D$ case, can be expressed as $f(k,\theta)$ for a circular potential $v(\vec{r}) = v(r)$ . By comparing (1.27) and (1.28) we can easily read off

$$f(\vec{k},\vec{k}\,') = -m_r\sqrt{\frac{i}{2\pi k}}\int d^2r'\, e^{-i\vec{k}\,'\cdot\vec{r}\,'} v(\vec{r}\,')\psi_k(\vec{r}\,'). \tag{1.29}$$

### 1.4.1 Partial wave solution and the phase shift

In 2D, the Green's function and thus the scattering amplitude $f(\vec{k},\vec{k}')$ have a logarithmic divergence at low energy. This makes a naive partial wave expansion ill-defined unless the correct asymptotic form is derived explicitly. To address this, we expand the solution in angular momentum eigenstates and identify how the phase shift $\delta_m$ naturally arises in the large-$r$ limit, following [24].

Consider equation (1.20) with a certain solution $\psi_k(r)$, we can expand the solution in terms of partial wave-functions $\varphi_m(k,r)$ (angular momentum eigenstates) as

$$\psi_k(\vec{r}) = \sum_{m=-\infty}^{\infty} \varphi_m(k,\vec{r}). \tag{1.30}$$

Each partial wave-function, in polar coordinates $(r, \theta)$, separates as

$$\varphi_m(\vec{r}, k) = R_m(r, k) e^{im\theta}, \quad m \in \mathbb{Z} \tag{1.31}$$

and $R_m(r, k)$ solves the radial Schroedinger problem

$$\left[\frac{d^2}{dr^2} + \frac{1}{r}\frac{d}{dr} + \left(k^2 - \frac{m^2}{r^2}\right)\right] R_m(r, k) = 0, \quad r > r_0 \tag{1.32}$$

outside the potential range. The general solution is a linear combination of Bessel functions:

$$R_m(r, k) = A_m(k) J_m(kr) + B_m(k) Y_m(kr), \tag{1.33}$$

where $J_m$ is the Bessel function of the first kind and $Y_m$ of the second kind.

At large distances, these have the asymptotic form:

$$J_m(kr) \sim \sqrt{\frac{2}{\pi kr}} \cos\left(kr - m\tfrac{\pi}{2} - \tfrac{\pi}{4}\right), \tag{1.34}$$

$$Y_m(kr) \sim \sqrt{\frac{2}{\pi kr}} \sin\left(kr - m\tfrac{\pi}{2} - \tfrac{\pi}{4}\right). \tag{1.35}$$

Therefore, the radial solution for $r \gg r_0$ can be written as:

$$R_m(r, k) \approx \sqrt{\frac{2}{\pi kr}} \Big[A_m(k) \cos\alpha_m(kr) + B_m(k) \sin\alpha_m(kr)\Big], \quad \alpha_m(kr) = kr - m\frac{\pi}{2} - \frac{\pi}{4}. \tag{1.36}$$

Using the standard identity $A_m \cos\alpha + B_m \sin\alpha = C_m \cos(\alpha + \delta_m)$, with $C_m = \sqrt{A_m^2 + B_m^2}$ and $\tan\delta_m = B_m/A_m$, we obtain the familiar asymptotic form:

$$R_m(r) \approx C_m(k) \sqrt{\frac{2}{\pi kr}} \cos\big(kr - m\tfrac{\pi}{2} - \tfrac{\pi}{4} + \delta_m(k)\big). \tag{1.37}$$

The phase shift $\delta_m(k)$ encodes the effect of the potential on the $m$-th angular momentum component and determines how the exact wave-function deviates from the free-particle solution at large distances.

Matching this solution with the exact solution inside the well fixes the ratio $B_m/A_m$ and thus the phase shift, which ultimately controls the scattering properties in two dimensions.

Putting all together we have

$$\psi_k(\vec{r}) \xrightarrow[r\to\infty]{} \sum_{m=-\infty}^{\infty} C_m(k) \sqrt{\frac{2}{\pi kr}} \cos\big(kr - m\tfrac{\pi}{2} - \tfrac{\pi}{4} + \delta_m(k)\big) e^{im\theta}, \tag{1.38}$$

which can be rewritten as incoming plus an outgoing circular wave as

$$\psi_k(\vec{r}) \approx \sum_{m=0}^{\infty} C_m \sqrt{\frac{1}{2\pi kr}} \left[ e^{i\left(kr - m\frac{\pi}{2} - \frac{\pi}{4} + \delta_m\right)} + e^{-i\left(kr - m\frac{\pi}{2} - \frac{\pi}{4} + \delta_m\right)} \right] \cos(m\theta), \tag{1.39}$$

where $C_m = C_{-m}$ was also assumed to hold.

Now the incident plane wave has expansion

$$e^{ikr\cos\theta} = \sum_{m=0}^{\infty} \epsilon_m i^m \cos(m\theta) J_m(kr), \quad \text{with} \quad \epsilon_0 = 1\,,\, \epsilon_{m\neq 0} = 2, \tag{1.40}$$

which in the asymptotic limit reads

$$\begin{aligned} e^{ikr\cos\theta} &\approx \sum_{m=0}^{\infty} \epsilon_m\, i^m \sqrt{\frac{2}{\pi kr}} \cos\left(kr - m\tfrac{\pi}{2} - \tfrac{\pi}{4}\right) \cos(m\theta) \\ &= \sum_{m=0}^{\infty} \epsilon_m\, i^m \sqrt{\frac{1}{2\pi kr}} \left[ e^{i(kr - m\frac{\pi}{2} - \frac{\pi}{4})} + e^{-i(kr - m\frac{\pi}{2} - \frac{\pi}{4})} \right] \cos(m\theta). \end{aligned} \tag{1.41}$$

Now by looking at (1.28), we see that the incoming circular wave part of $\psi_k(\vec{r})$ must match the incoming circular part of the incoming plane wave thus we can read of the coefficients $C_m(k)$

$$C_m(k) = \epsilon_m i^m e^{i\delta_m(k)} \tag{1.42}$$

instead by matching the outgoing part, following (1.28) and using the expression for the coefficients $C_m$, we get

$$\begin{aligned} \sum_{m=0}^{\infty} \epsilon_m\, i^m\, e^{i\delta_m} \sqrt{\frac{1}{2\pi kr}}\, e^{i\left(kr - m\frac{\pi}{2} - \frac{\pi}{4} + \delta_m\right)} \cos(m\theta) = \sum_{m=0}^{\infty} \epsilon_m\, i^m \sqrt{\frac{1}{2\pi kr}}\, e^{i(kr - m\frac{\pi}{2} - \frac{\pi}{4})} \cos(m\theta) \\ + \frac{e^{ikr}}{\sqrt{r}}\, f(k,\theta). \end{aligned} \tag{1.43}$$

From the above equation we can read off

$$f(k,\theta) = \sqrt{\frac{1}{2\pi k}} \sum_{m=0}^{\infty} \epsilon_m i^m (e^{2i\delta_m} - 1) \cos(m\theta), \tag{1.44}$$

and using $e^{2i\delta_m} - 1 = 2ie^{i\delta_m} \sin\delta_m$ obtain

$$f(k,\theta) = \sqrt{\frac{2}{\pi k}} \sum_{m=0}^{\infty} \epsilon_m i^{m+1} e^{i\delta_m} \sin\delta_m \cos(m\theta). \tag{1.45}$$

For the case of an s-wave scattering the expression reduces to

$$f(k,\theta) \to i\sqrt{\frac{2}{\pi k}}e^{i\delta_0}\sin\delta_0. \tag{1.46}$$

The results shows explicitly how the scattering amplitude must be expanded in two dimensions. Unlike the straightforward partial-wave decomposition in 3D, in 2D one must carefully derive the correct angular momentum expansion and the role of the phase shifts $\delta_m(k)$. As in the three-dimensional case, the effect of the interaction is to shift the phase of each outgoing circular partial wave by $\delta_m(k)$. This phase shift encapsulates all the information about how the potential modifies the scattering process for each angular momentum channel.

In the ultracold regime, typical atomic momenta $k$ are so small that only the lowest partial waves contribute significantly. One can show that for $m \neq 0$, the phase shifts vanish rapidly as $\delta_m(k) \propto k^{2m}$. The dominant contribution therefore comes from the $m = 0$ (s-wave) channel.

However, in two dimensions the s-wave phase shift behaves quite differently: for small $k$, it has a characteristic logarithmic dependence on the scattering length $a_{2D}$,

$$\delta_0(k) \approx \frac{\pi}{2[\ln(ka_{2D}) + \gamma_E - \ln 2]} + O(k^2), \quad k \to 0. \tag{1.47}$$

where $\gamma_E \sim 0.577$ is the Euler-Mascheroni constant. This relation defines the *2D scattering length.* Its appearance reflects the peculiar logarithmic nature of two-dimensional scattering, which fundamentally distinguishes it from the power-law behaviour in three dimensions.

It is important to state that this way of defining the two dimensional s-wave scattering length is just a convention, in other works it is defined through the expression

$$\delta_0(k) \approx \frac{\pi}{2\ln(k\tilde{a}_{2D})} + O(k^2). \quad k \to 0. \tag{1.48}$$

The two conventions are thus related via

$$\tilde{a}_{2D} = \frac{e^{\gamma_E}}{2}a_{2D}. \tag{1.49}$$

In what follows, $a_{2D}$ will play a central role as the effective interaction parameter for Bose-Fermi mixtures confined to two dimensions.

## 1.5 The spherical square-well potential

A simple but instructive model to understand low-energy scattering and the formation of bound states is the spherical square-well potential, defined as

$$V(r) = \begin{cases} -V_0, & r < r_0, \\ 0, & r > r_0, \end{cases} \tag{1.50}$$

where $V_0 > 0$ sets the depth of the well and $r_0$ its range.

### 1.5.1 Radial Schrödinger equation in dimension D

The time-independent Schrödinger equation for a spherically symmetric potential in $D$ spatial dimensions reads:

$$-\frac{1}{2m_r}\nabla^2\psi(\vec{r}) + V(r)\psi(\vec{r}) = E\psi(\vec{r}), \tag{1.51}$$

where $m_r$ is the reduced mass of the interacting particles.

For s-wave scattering (zero orbital angular momentum), the wave-function depends only on $r = |\vec{r}|$. In spherical coordinates, the Laplacian is

$$\nabla^2\psi(r) = \frac{1}{r^{D-1}}\frac{\partial}{\partial r}\left(r^{D-1}\frac{\partial\psi}{\partial r}\right). \tag{1.52}$$

Thus, the radial equation reads

$$-\frac{1}{2m_r}\left[\frac{\partial^2\psi}{\partial r^2} + \frac{D-1}{r}\frac{\partial\psi}{\partial r}\right] + V(r)\psi(r) = E\psi(r). \tag{1.53}$$

To simplify the structure of the equation and eliminate the first derivative term, it is standard to define the reduced radial function $u(r)$ by

$$\psi(r) = \frac{u(r)}{r^{(D-1)/2}}. \tag{1.54}$$

Substituting this into the radial equation yields a one-dimensional Schrödinger equation for $u(r)$:

$$-\frac{1}{2m}\frac{d^2u}{dr^2} + V_{\text{eff}}(r)u(r) = Eu(r), \tag{1.55}$$

with the effective potential

$$V_{\text{eff}}(r) = V(r) + \frac{1}{2m_r}\frac{(D-1)(D-3)}{4r^2}. \tag{1.56}$$

This shows that, for general $D$, the centrifugal-like term appears even for s-wave due to the dimensionality. In particular:

- For $D = 3$, $(D-1)(D-3) = 0$, so the effective potential reduces to $V(r)$, and the equation for $u(r)$ is simply:

$$-\frac{1}{2m_r}\frac{d^2u}{dr^2} + V(r)u(r) = Eu(r). \tag{1.57}$$

- For $D = 2$, there remains a nonzero effective angular term:

$$(D-1)(D-3) = -1, \qquad \Longrightarrow V_{\text{eff}}(r) = V(r) - \frac{1}{8m_r r^2}.$$

Therefore the form with the explicit first derivative appears naturally when using $\psi(r)$ directly, while the reduced radial function $u(r)$ absorbs the geometric factor, yielding a standard 1D-like Schrödinger equation with an effective centrifugal term. This formulation is extremely convenient for matching boundary conditions and defining the scattering length at low energies.

### 1.5.2 Bound state condition

For $E < 0$, define the wave numbers

$$k = \sqrt{2m_r(V_0 - |E|)}, \quad \kappa = \sqrt{2m|E|}. \tag{1.58}$$

The regular solution inside the square well is

$$u_{\text{in}}(r) = A\, r^{-\frac{D-2}{2}} J_{(D-2)/2}(kr), \tag{1.59}$$

while outside the well (for a bound state with $E < 0$),

$$u_{\text{out}}(r) = B\, r^{-\frac{D-2}{2}} K_{(D-2)/2}(\kappa r), \tag{1.60}$$

where $J_\alpha$ and $K_\alpha$ are Bessel functions of the first and second kind (B.1) respectively, while $A$ and $B$ are normalization constants.

Matching $u$ and $u'$ at $r = r_0$ yields a transcendental equation whose solutions give the allowed bound state energies.

### 1.5.3 Low-energy limit and the scattering length

To understand the physical meaning of the scattering length and its relation to bound states, we examine the zero-energy limit ($E \approx 0$).

**3D case.** In three dimensions, the reduced radial wave-function for $r > r_0$ satisfies:

$$\frac{d^2u}{dr^2} = 0. \tag{1.61}$$

Its general solution is linear:

$$u(r) = B(r - a), \tag{1.62}$$

where $a$ is the scattering length, defined so that the free solution extrapolates to zero at $r = a$. Keep in mind that this form is valid only in the low-energy limit, where the detailed shape of the potential does not appear explicitly. Thus, the external wave-function is

$$\psi(r) = \frac{u(r)}{r} = B\left(1 - \frac{a}{r}\right), \quad r > r_0. \tag{1.63}$$

Inside the well, for $E \approx 0$:

$$u(r) = A\sin(kr), \quad k^2 = 2m_rV_0. \tag{1.64}$$

Continuity at $r = r_0$ gives:

$$A\sin(kr_0) = B(r_0 - a), \tag{1.65}$$

$$Ak\cos(kr_0) = B. \tag{1.66}$$

Solving for $a$ yields the standard relation:

$$a = r_0\left[1 - \frac{\tan(kr_0)}{kr_0}\right]. \tag{1.67}$$

This shows explicitly:

- For weak attraction ($V_0$ small), expanding $\tan(kr_0) \simeq kr_0 + \frac{1}{3}(kr_0)^3$ gives $a < 0$.
- When $kr_0 = \pi/2$, tan diverges: the scattering length jumps discontinuously from $-\infty$ to $+\infty$; this marks the threshold where the first bound state appears at $E = 0$.
- For $V_0$ larger than this first threshold, the well supports at least one bound state and the scattering length initially becomes positive and large. As the depth increases further the scattering length smoothly decreases, can become negative again, and eventually diverges once more when the well is deep enough to support an additional bound state (at $kr_0 = \frac{3\pi}{2}, \frac{5\pi}{2}, \ldots$).

Importantly, in this regime, the binding energy is directly related to $a$ [3, 4]:

$$E_B = -\frac{1}{2m_r a^2}, \quad \text{valid only if } a > 0. \tag{1.68}$$

Therefore, the sign of $a$ unambiguously indicates whether a bound state exists:

$$\boxed{\begin{aligned} a < 0 &\implies \text{No bound state,} \\ a = \pm\infty &\implies \text{Threshold,} \\ a > 0 &\implies E_B < 0. \end{aligned}}$$

**2D case.** In two dimensions ($D = 2$), the situation differs: even an arbitrarily shallow attractive potential always supports a bound state.

For $E < 0$, the bound-state solution inside the well is

$$u_{\text{in}}(r) = AJ_0(kr), \quad k^2 = 2m_r(V_0 - |E|), \tag{1.69}$$

while outside the well it behaves logarithmically:

$$\psi(r) \sim \ln\left(\frac{r}{a_{2D}}\right), \quad r > r_0. \tag{1.70}$$

By matching the wave-function and its derivative at $r = r_0$ in the limit of a very shallow bound state ($|E| \to 0$), one finds the relation

$$\ln\left(\frac{r_0}{a_{2D}}\right) = \frac{1}{kr_0}\frac{J_1(kr_0)}{J_0(kr_0)} \simeq \frac{1}{kr_0}\tan(kr_0), \quad k^2 = 2m_r V_0. \tag{1.71}$$

In 2D, this equation always admits a solution $a_{2D} > 0$ for any $V_0 > 0$, implying that an attractive potential always supports at least one bound state.

As the well becomes deeper, $\tan(kr_0)$ can diverge at $kr_0 = \pi/2, 3\pi/2, \ldots$, which corresponds to the appearance of additional bound states (excited levels).

In the limit of a very shallow well ($V_0$ small), the resulting $a_{2D}$ is exponentially large, leading to a weak bound state with energy [25]

$$E_B^{(2D)} = -\frac{4}{m_r a_{2D}^2} e^{-2\gamma}. \tag{1.72}$$

Thus, the sign and scale of $a_{2D}$ are consistent with the existence of a bound state for any attractive potential in 2D.

These results clarify that in $3D$ the sign and value of the scattering length reveal whether the potential is strong enough to bind, while in $2D$ there is always at least one bound state for any attractive well.

When $r_0 \to 0, V_0 \to \infty$ with $V_0 r_0$ fixed, the square well becomes a Dirac well (zero-range pseudopotential): the only relevant parameter is the scattering length. This limit justifies replacing the detailed short-range potential with the Bethe–Peierls boundary condition, which encodes the same low-energy physics.

## 1.6 Bethe-Peierls Boundary Conditions

In ultracold atomic systems, the details of the short-range interatomic potential are usually irrelevant, since the inter-particle distance is much larger than the range of the potential. Instead, the low-energy scattering properties can be encoded by effective boundary conditions on the wave-function at short distances, known as *Bethe-Peierls boundary conditions* [26].

### 1.6.1 Three Dimensions

In three dimensions, for two particles interacting via a short-range potential, the asymptotic behaviour of the relative wave-function $\psi(\vec{r})$ at small inter-particle distance $|\vec{r}| = r$ is determined solely by the $s$-wave scattering length $a_{3D}$. The Bethe-Peierls boundary condition [26, 4, 2] reads

$$\lim_{r\to 0} \frac{(r\psi(r))'}{r\psi(r)} = -\frac{1}{a_{3D}}. \tag{1.73}$$

This condition replaces the need to specify the full microscopic interaction potential, simplifying the description of low-energy scattering processes.

Physically, it corresponds to an asymptotic form of the wave-function near $r = 0$ given by

$$\psi(r) \sim A\left(\frac{1}{r} - \frac{1}{a_{3D}}\right), \quad \text{for } r \to 0, \tag{1.74}$$

where $A$ is a normalization constant. The divergence $1/r$ is a consequence of the three-dimensional Green's function behaviour (1.4), while $a_{3D}$ encodes the effects of interactions.

### 1.6.2 Two Dimensions

In two dimensions, the $s$-wave solution of the free Schrödinger equation behaves logarithmically at small distances, reflecting the different dimensionality of space. The Bethe-Peierls boundary condition [25] in two dimensions reads

$$\lim_{r\to 0}\left[r\frac{d}{dr} - \frac{1}{\ln(r/a_{2D})}\right]\psi(r) = 0, \tag{1.75}$$

where $a_{2D}$ is the two-dimensional scattering length.

Physically, this condition corresponds to a short-distance behaviour of the wave-function of the form

$$\psi(r) \sim A\ln\left(\frac{r}{a_{2D}}\right), \quad \text{for } r \to 0, \tag{1.76}$$

where $A$ is a normalization constant.

Compared to the three-dimensional case, the logarithmic divergence at short distance makes the 2D scattering problem more delicate.

# Chapter 2

# The Lowest Order Constrained Variational (LOCV) Approximation

## 2.1 Historical Background and Motivation

The Lowest Order Constrained Variational (LOCV) method was originally introduced in the context of nuclear physics, particularly for describing strongly interacting nucleon systems where short-range repulsion makes standard perturbative treatments unreliable. Early developments by Pandharipande, Bethe, and others aimed to formulate a variational approach that could capture essential two-body correlations in a dense many-body environment while remaining computationally tractable.

The key innovation of the LOCV approach lies in its systematic truncation of the cluster expansion [19, 27, 28] of the variational energy at the level of two-body correlations, together with a physically motivated constraint that serves a dual purpose. Firstly, it guarantees physically meaningful behaviour of the pair correlation function by enforcing its healing to unity at large distances, an essential condition rigorously discussed by Krotscheck [27] for any truncated variational theory. Secondly, the constraint statistically incorporates the influence of subleading higher-order correlations in an effective manner through the introduction of an average potential field and the associated healing length [17, 18]. This makes it particularly useful for systems where short-range correlations dominate, such as nuclear matter and liquid helium. Over time, the method was extended and adapted to other strongly correlated quantum systems, including ultracold atomic gases, where the availability of Feshbach resonances allows experimentalists to probe regimes of strong interactions and non-perturbative physics.

In the context of ultracold gases, the LOCV method offers a valuable compromise between simplicity and accuracy. It captures leading-order correlation effects without invoking uncontrolled approximations or computationally intensive techniques such as quantum Monte Carlo. This balance makes it especially appealing for exploring fundamental questions about stability, collective behaviour, and equation of state in many-body systems with tunable interactions.

## 2.2 Formalism and Physical Content of the LOCV Method

In the LOCV framework, the many-body wave-function is assumed to take the Jastrow-Slater correlated form

$$\Psi(\vec{r}_1, \vec{r}_2, \ldots, \vec{r}_N) = \prod_{i<j} f(r_{ij})\, \Phi_{\text{sym/antisym}}(\vec{r}_1, \vec{r}_2, \ldots, \vec{r}_N), \tag{2.1}$$

where $\Phi_{\text{sym/antisym}}$ denotes a properly symmetrized or antisymmetrized product of single-particle states, and $f(r)$ is a two-body correlation function introducing short-range correlations into the system.

The LOCV method is built upon a key approximation: the truncation of the cluster expansion of the energy functional at the two-body level. That is, when evaluating the expectation value of the Hamiltonian, only contributions arising from isolated correlated pairs are retained, while three-body and higher-order correlations are systematically neglected. This truncation is justified when the system is dilute and dominated by short-range interactions, as higher-order correlations are suppressed by both geometric factors and the additional imposed constraint.

The correlation function $f(r)$ satisfies the Euler-Lagrange equation

$$-\frac{1}{2m_r}\nabla^2 f(r) + V(r) f(r) = \lambda f(r), \tag{2.2}$$

associated to the energy density functional

$$\frac{E}{V} = \rho_1 \rho_2 \int \left( V(r) - \frac{1}{2m_r} \frac{\nabla^2 f(r)}{f(r)} \right) f(r)^2 d^D r \tag{2.3}$$

where $V(r)$ is the interaction potential between two particles, $\rho_1$ and $\rho_2$ the densities of the interacting species, $m_r$ is the reduced mass of the interacting pair, and $\lambda$ is a Lagrange multiplier introduced to enforce a constraint on the average number of correlated particles.

In the LOCV scheme, the constraint is formulated by requiring that, on average, within a ball of radius $d$ (called the *healing distance*) around a given particle of species 1, there is only one other correlated particle of species 2 or vice versa ($1 \longleftrightarrow 2$). This is expressed by the condition

$$\rho_2 \int_{|\vec{r}| \leq d} d^D r \, f^2(r) = 1, \tag{2.4}$$

where $D$ is the spatial dimension. This constraint ensures the validity of the pairwise approximation and prevents the overlap of multiple strong two-body correlations within the same region.

At short distances, where the scattering properties of the interaction dominate, the function $f(r)$ must correctly reproduce two-body physics, independent of the specific microscopic form of the potential. This is ensured by imposing Bethe-Peierls boundary conditions, as discussed in Chapter 1.6. These conditions capture the low-energy scattering behaviour crucial for ultracold systems.

At larger distances, where inter-particle interactions become negligible, the correlation function must smoothly match the uncorrelated many-body background. This is enforced by the healing conditions at $r = d$,

$$f(d) = 1, \quad \left.\frac{df}{dr}\right|_{r=d} = 0, \tag{2.5}$$

ensuring continuity and smooth matching to the free-particle behaviour beyond the healing length.

Once the correlation function $f(r)$ has been determined, it is used to compute the expectation value of the kinetic and potential energy terms in the Hamiltonian. At leading order, the energy per particle is obtained by integrating these contributions over correlated pairs. Due to the imposed constraint, the main contributions arise from isolated two-body terms, which allows for an immediate and accurate estimate of the ground-state energy.

It is important to recognize a fundamental limitation of the LOCV approach when using a Jastrow-Slater ansatz, since by construction, it prevents the formation of tightly bound molecular states. Consequently, the LOCV approximation remains valid only within a metastable atomic phase, and fails to capture any phase transition to a molecular or deeply bound state that may occur at strong coupling. For instance, if the system undergoes a transition from an atomic gas to a molecular gas at a critical interaction strength $\eta_c$, the LOCV energy functional will not reflect this transition, as it does not include variational freedom to describe bound dimers.

In conclusion, the LOCV method provides a robust framework for studying interacting quantum systems with short-range correlations, particularly in dilute and moderately interacting regimes. It will serve as the foundation for our analysis of Bose-Fermi mixtures in the following chapter.

**Note on observables.** In the LOCV framework, the function $f(r)$ is the two-body correlation factor used to build the variational wave-function. The physically measurable quantity is the pair correlation function $g(r) = f^2(r)$, which describes the probability density of finding two particles separated by a distance $r$ [19].

### 2.2.1 On the Constraint Choice in Variational Jastrow Theory

As emphasized by Krotscheck in his foundational work on Jastrow theory [27], the choice of constraint in variational calculations plays a critical role in determining the physical validity of the resulting theory. In the LOCV approximation, the constraint

$$\rho_2 \int_{|\vec{r}|\leq d} d^D r \, f^2(r) = 1 \tag{2.6}$$

ensures that on average only one particle, of the other species, is correlated within the healing volume. This condition effectively prevents overlap between multiple correlated pairs, thus justifying the truncation at the two-body level.

Krotscheck noted, however, that such a constraint is not unique. One could in principle constrain other functionals of $f(r)$, such as $\int dr f(r)$ or even terms involving derivatives of $f(r)$, depending on the physical quantity one aims to control. Nonetheless, the LOCV constraint has the important advantage of enforcing "normalization of probability density" in a two-body sense, making it physically transparent.

### 2.2.2 On the Small Parameters in the Theory

In order to justify expansions of the energy functional within the LOCV framework, it is useful to define small parameters that quantify the deviation of the correlation function $f(r)$ from the uncorrelated limit $f(r) \to 1$. Two such parameters are:

$$\delta_h \equiv \rho_2 \int_{|\vec{r}|\leq d} d^D r \, \left[f^2(r) - 1\right] \equiv \rho_2 \int_{|\vec{r}|\leq d} d^D r \, h(r), \tag{2.7}$$

$$\delta_\ell \equiv \rho_2 \int_{|\vec{r}|\leq d} d^D r \, [f(r) - 1] \equiv \rho_2 \int_{|\vec{r}|\leq d} d^D r \, \ell(r). \tag{2.8}$$

These parameters remain small in the dilute limit, where the typical inter-particle distance greatly exceeds the range of the interaction. In this regime, $f(r)$ differs from unity only in a narrow shell around $r = 0$, and therefore both $h(r)$ and $\ell(r)$ have small integrated weight.

From a physical standpoint, these integrals quantify the extent to which the two-body correlations distort the many-body wave-function from the uncorrelated limit. Their smallness reflects the fact that significant correlations occur only within a limited volume around each particle, justifying the LOCV assumption that dominant contributions arise from isolated pairwise interactions.

In practical terms, the smallness of $\delta_\ell$ supports the validity of using a linear approximation in $\ell(r)$ when evaluating the expectation value of additional perturbations $V_{int}$, which may be applied to the system. Similarly, the smallness of $\delta_h$ reinforces the idea that the total effect of Bose-Fermi correlations remains localized and dilute, which underlies the entire LOCV framework.

### 2.2.3 Physical constraints on the sign of $\eta$ in the repulsive and attractive regimes

In the LOCV framework, the interspecies interaction is conveniently parametrized (in $3D$) by the dimensionless coupling

$$\eta = \frac{1}{ak_F}, \tag{2.9}$$

where $a$ is the $3D$ $s$-wave scattering length and $k_F$ is the Fermi wave-vector.

The sign and value of $a$ directly reflect the physical nature of the interaction at low energies:

- $a < 0$: the potential is attractive but too weak to support a bound state. The scattering phase shift at low energy is positive, signalling an effectively attractive interaction.
- $a > 0$: the potential is strong enough to support a bound state (strongly correlated pair).

This duality allows one to distinguish between two regimes:

1. **Attractive branch (ground state).** Here, the pair wave-function describes the actual ground state. One can explore both $a < 0$ and $a > 0$ consistently. In this case, $\eta$ can take both negative and positive values, covering the entire crossover from weak to strong coupling.
2. **Repulsive branch (excited state).** This corresponds to the so-called *upper branch*: an excited scattering state in the presence of an attractive well. Physically, it represents atomic pairs that avoid forming the bound "molecular" state and instead scatter with positive energy. In this context, it is meaningful only if $a > 0$:

   $$E > 0 \quad \Longrightarrow \quad a > 0 \quad \Longrightarrow \eta > 0.$$

   Allowing $\eta < 0$ for this excited state would imply switching back to a situation with no bound state and no well-defined upper branch.

This physical constraint is naturally seen in the phase shift for positive energy:

$$\tan \delta_0(k) = -ka. \tag{2.10}$$

For $a > 0$, the phase shift is negative, implying an effectively repulsive low-energy behaviour.

In summary, the sign of $\eta$ must respect the physical nature of the branch under study:

$$\boxed{\begin{array}{rl} \text{Attractive (ground) branch:} & \eta \in (-\infty, +\infty) \\ \text{Repulsive (upper) branch:} & \eta \in (0, +\infty). \end{array}}$$

This clarifies why, in all plots and calculations for the repulsive regime, one must restrict $\eta$ to positive values only, while the attractive branch can span the entire range.

### Sign of $\eta$ in two dimensions

In two dimensions, the natural dimensionless coupling is defined as

$$\eta = \ln\left(\frac{1}{k_F a_{2D}}\right) = -\ln(k_F a_{2D}). \tag{2.11}$$

Since any attractive potential in 2D always supports at least one bound state, the scattering length $a_{2D}$ is always positive. The logarithmic form allows both signs for $\eta$:

- $\eta \gg 0$ corresponds to a strongly correlated pair ($a_{2D} \ll 1/k_F$).
- $\eta \ll 0$ corresponds to a weakly bound pair ($a_{2D} \gg 1/k_F$).

Therefore also in $2D$ one can distinguish between two regimes:

1. **Attractive branch (ground state).** This describes the physical ground state. It is meaningful for all $\eta$ (both positive and negative).
2. **Repulsive branch (excited state).** This describes an excited scattering-like solution built above the bound state by enforcing a correlation function with one node. Physically, it represents a higher-energy configuration where particles avoid forming the lowest bound state but still feel the underlying potential.

   In two dimensions, unlike in three dimensions, this excited branch can be formally defined for all $\eta$. However, for sufficiently negative $\eta$ the potential becomes too weak to support a true excited level: the LOCV wave-function still exists mathematically but no longer corresponds to a physical resonance. In this regime ($\eta < 0$), the energy gap between the excited (repulsive) branch and the attractive branch becomes very small compared to the well-defined splitting for $\eta > 0$. In a many-body setting, this means that particles occupying the repulsive branch for negative $\eta$ can more readily decay into the lower-energy attractive branch, making this portion of the repulsive solution only meta-stable within the LOCV framework. Therefore, while $\eta$ can take any real value, the physically meaningful regime for a repulsive branch is mainly $\eta > 0$.

Thus, in two dimensions (in a many-body theory) we have:

$$\boxed{\begin{array}{rl} \text{Ground branch:} & \eta \in (-\infty, +\infty) \\ \text{Repulsive branch:} & \eta \in (0, +\infty). \end{array}}$$

This reflects the special feature of two-dimensional scattering: an arbitrarily weak attractive interaction always supports a bound state, and the LOCV formalism mathematically permits the excited (repulsive) $2D$ solution to extend across the entire range of $\eta$. However, while this is well-defined at the two-body level, in a many-body context its interpretation becomes questionable for large negative $\eta$, where the repulsive branch is meta-stable and particles can more easily decay into the true ground state.

**Conventions for $\eta$ in two dimensions** As already highlighted in Section 1.4, there exist two main conventions on how to define the two dimensional s-wave scattering length $a_{2D}$. This convention naturally extends to the interaction parameter $\eta = -\ln(k_F a_{2D})$ and using (1.49) the other possible choice reads

$$\tilde{\eta} = \eta + \ln 2 - \gamma_E. \tag{2.12}$$

Throughout this work $\tilde{\eta}$ will appear when comparing results with data or perturbative benchmarks associated to the other convention.

## 2.3 B-F ground state energy functional

Before applying the LOCV formalism to specific Bose-Fermi systems, it is useful to first derive the general expression for the ground state energy functional of a Bose-Fermi mixture in $D$ spatial dimensions. This derivation, based on a Jastrow-Slater variational ansatz, establishes the foundation upon which the LOCV equations will later be formulated.

The main objective of this section is the derivation of the ground state energy density of an interacting Bose-Fermi mixture in $D$ dimensions at 0 Kelvin in the thermodynamic limit, expressed in terms of the correlation function $f(x)$ between bosons and fermions; we will completely neglect boson-boson and fermion-fermion correlations.

Let us start by considering $N_B$ massive bosons with mass $m_B$ and $N_F$ massive fermions with mass $m_F$ in a volume $V$ not interacting with each other, the (free) Hamiltonian describing the system takes the form:

$$H_0 = \sum_{i=1}^{N_B} -\frac{1}{2m_B}\nabla_i^2 + \sum_{j=1}^{N_F} -\frac{1}{2m_F}\nabla_j^2. \tag{2.13}$$

At $T = 0\ K$ the Bose gas ground state is a condensate and each boson has zero momentum, so the wave-function is a uniform distribution

$$\Phi_{BG}(\vec{r}_1, \ldots, \vec{r}_{N_B}) = \left(\frac{1}{V}\right)^{\frac{N_B}{2}}. \tag{2.14}$$

The fermionic ground state instead has the lowest $N_F$ single particle states (plane waves) $\phi_k(\vec{R}) = \frac{1}{\sqrt{V}} e^{i\vec{k}\cdot\vec{R}}$ occupied by a single fermion; this is because we are considering spinless fermions (fermionic atoms with the same specific hyperfine state). Since we are dealing with spinless fermions the antisymmetrization of the wave-function is by necessity performed on the spacial part and this is done via a Slater determinant $\|...\|$; so the Fermi gas wave-function reads

$$\Phi_{FG}(\vec{R}_1, \ldots, \vec{R}_{N_F}) = \left(\frac{1}{V}\right)^{\frac{N_F}{2}} \|e^{i\vec{k}_n\cdot\vec{R}_m}\| = \left\langle \mathbf{R} \middle| \Phi_{FG} \right\rangle. \tag{2.15}$$

Now in the presence of an interaction between bosons and fermions, the Hamiltonian reads

$$H_{BF} = \sum_{i=1}^{N_B} -\frac{1}{2m_B}\nabla_i^2 + \sum_{j=1}^{N_F} -\frac{1}{2m_F}\nabla_j^2 + \sum_{i=1}^{N_B}\sum_{j=1}^{N_F} U_{BF}(\vec{r}_i - \vec{R}_j). \tag{2.16}$$

We assume that the interaction potential $U_{BF}(r)$ is short-ranged, central, and spherically symmetric. This assumption allows us to make use of well-established results from quantum scattering theory and to apply the Bethe-Peierls boundary condition at short distances, as discussed in Section 1.6.

With an Hamiltonian of this form, an analytical solution for the wave-function is not available; we will use a variational wave-function $\Psi$ of the Jastrow-Slater type as discussed in Chapter 2

$$\Psi(\vec{\mathbf{r}}, \vec{\mathbf{R}}) = \prod_{i,j} f(|\vec{r}_i - \vec{R}_j|)\Phi_{BG}(\vec{\mathbf{r}})\Phi_{FG}(\vec{\mathbf{R}}), \tag{2.17}$$

where $\vec{\mathbf{r}} = (\vec{r}_1, \dots, \vec{r}_{N_B})$ are the bosonic coordinates and $\vec{\mathbf{R}} = (\vec{R}_1, \dots, \vec{R}_{N_F})$ the fermionic ones. As we said in the previous chapter, $f(x)$ is a still unknown function of the relative coordinates between bosons and fermions; it dictates the correlation among the two particles as a function of the distance between them. If $f(x) = 1$ for some distance $x$ then there is no correlation between the particles; indeed if all $f(r_i - R_j) = f_{ij}$ could be equal to 1 then the wave-function $\Psi$ would tend to the wave-function of the free system $\Phi_{BG}\Phi_{FG}$.

We call with $d$ the healing distance, the minimum distance such that $f(d) = 1$; this will be one of the boundary conditions that we need to impose on the system. Moreover since $f(r > d) = 1$ we want $f(r)$ to be flat at $d$, so $f'(d) = 0$ must be imposed as well as a boundary condition.

In numerical techniques such as quantum Monte Carlo, the healing distance $d$ is often treated as a variational parameter. In contrast, within the LOCV framework, $d$ is not varied but rather plays the role of a constraint scale for the validity of the two-body correlation approximation. The true variational "parameter" in LOCV is the functional form of $f(r)$ itself.

In bra-ket notation we write $\Psi$ as

$$|\Psi\rangle \equiv \prod f \, |\Phi_{BG}\rangle \, |\Phi_{FG}\rangle \equiv \prod f \, |\Phi\rangle \,, \tag{2.18}$$

where $|\Phi_{BG}\rangle$,$|\Phi_{FG}\rangle$ are properly normalized: $\langle\Phi_{BG}|\Phi_{BG}\rangle = \langle\Phi_{FG}|\Phi_{FG}\rangle = 1$; thus also the free B-F mixture wave-function $\langle\Phi|\Phi\rangle = 1$.

We write the energy density expectation value as

$$\begin{aligned}
\frac{\langle H_{BF}\rangle}{V} =& \frac{1}{V}\frac{\langle\Psi| H_{BF} |\Psi\rangle}{\langle\Psi|\Psi\rangle} = \frac{1}{V}\frac{\langle\Phi| \prod f H_{BF} \prod f |\Phi\rangle}{\langle\Phi| \prod f \prod f |\Phi\rangle} \\
=& -\frac{1}{V}\frac{\sum_i \frac{1}{2m_B} \langle\Phi| \prod f \nabla_i^2 \prod f |\Phi\rangle + \sum_j \frac{1}{2m_F} \langle\Phi| \prod f \nabla_j^2 \prod f |\Phi\rangle}{\langle\Phi| \prod f \prod f |\Phi\rangle} \\
&+ \frac{1}{V}\frac{\sum_{ij} \langle\Phi| \prod f U_{ij} \prod f |\Phi\rangle}{\langle\Phi| \prod f \prod f |\Phi\rangle}.
\end{aligned} \tag{2.19}$$

Now the Laplacian operators will act as follows

$$\nabla_n^2 \prod f \left|\Phi\right\rangle = (\nabla_n^2 \prod f) \left|\Phi\right\rangle + 2(\nabla_n \prod f) \cdot \nabla_n \left|\Phi\right\rangle + (\prod f) \nabla_n^2 \left|\Phi\right\rangle . \tag{2.20}$$

For the bosonic indices $n = i$ only the first of the three terms survives since $\nabla_i \left|\Phi_{BG}\right\rangle = 0$, while for the fermionic ones $n = j$ all three of them contribute. Let us focus on the middle term $\propto \nabla_j \left|\Phi_{FG}\right\rangle$, when $\nabla_j$ acts on the fermi sphere $\left|\Phi_{FG}\right\rangle$ it brings down a wave-vector $\vec{k}_j$ as an eigenvalue, that has a certain direction, so considering the sum on all the fermions eventually the term will be proportional to $\sum_j \vec{k}_j$ which in the thermodynamic limit goes to zero since there aren't preferable directions taken by the fermions. The last term instead will be exactly proportional to the energy of the free fermi gas $N_F E_{FG}$ and we have $-\frac{1}{2m_F}\nabla_j^2 \left|\Phi_{FG}\right\rangle = E_{FG} \left|\Phi_{FG}\right\rangle$. Thus we can write (2.19) as

$$\begin{aligned} \frac{\left\langle H_{BF}\right\rangle}{V} = \frac{N_F}{V} E_{FG} &- \frac{1}{2m_B} \sum_i \frac{\left\langle\Phi\right| \prod f (\nabla_i^2 \prod f) \left|\Phi\right\rangle}{V \left\langle\Phi\right| \prod f \prod f \left|\Phi\right\rangle} \\ &- \frac{1}{2m_F} \sum_j \frac{\left\langle\Phi\right| \prod f (\nabla_j^2 \prod f) \left|\Phi\right\rangle}{V \left\langle\Phi\right| \prod f \prod f \left|\Phi\right\rangle} \\ &+ \sum_{ij} \frac{\left\langle\Phi\right| \prod f U_{ij} \prod f \left|\Phi\right\rangle}{V \left\langle\Phi\right| \prod f \prod f \left|\Phi\right\rangle} . \end{aligned} \tag{2.21}$$

For the next step we want to express everything in terms of the relative coordinates $\vec{x}_{ij} = \vec{r}_i - \vec{R}_j$ between bosons and fermions, by carefully manipulating the expressions one finds

$$\begin{aligned} \frac{1}{2m_B} \sum_i (\nabla_i^2 \prod f) + \frac{1}{2m_F} \sum_j (\nabla_j^2 \prod f) = &\sum_{ij} \left[ (\frac{1}{2m_B}\nabla_i^2 + \frac{1}{2m_F}\nabla_j^2) f_{ij} \right] (\prod_{\alpha\beta \neq ij} f_{\alpha\beta}) \\ &+ \frac{1}{2m_B} \sum_{ij} \left\{ (\nabla_i f_{ij}) \sum_{\sigma \neq j} \left[ (\nabla_i f_{i\sigma}) (\prod_{\alpha \neq i; \beta \neq j, \sigma} f_{\alpha\beta}) \right] \right\} \\ &+ \frac{1}{2m_F} \sum_{ij} \left\{ (\nabla_j f_{ij}) \sum_{\rho \neq i} \left[ (\nabla_j f_{\rho j}) (\prod_{\alpha \neq i, \rho; \beta \neq j} f_{\alpha\beta}) \right] \right\} . \end{aligned} \tag{2.22}$$

The last two terms give information on three-body correlations which are neglected in the LOCV approximation, so we will retain only the first term.

Using the standard change of variables

$$(\vec{r}_i, \vec{R}_j) \rightarrow (\vec{X}_{CM} = \frac{m_B \vec{r}_i + m_F \vec{R}_j}{m_B + m_F}, \vec{x}_{ij} = \vec{r}_i - \vec{R}_j) \tag{2.23}$$

to the center of mass coordinate and relative coordinate, one finds that the kinetic energy of a B-F pair, which appears in the first term of the right hand side of (2.22), gets rewritten as

$$\frac{1}{2m_B}\nabla_i^2 + \frac{1}{2m_F}\nabla_j^2 \to \frac{1}{2M}\nabla_{CM}^2 + \frac{1}{2m_r}\nabla_{ij}^2, \tag{2.24}$$

where $M = m_B + m_F$ and $m_r = (m_B m_F)/(m_B + m_F)$ is the reduced mass of a Bose-Fermi pair. Moreover since the correlation function $f(|\vec{x}_{ij}|)$ depends only on the relative coordinate and not on the center of mass coordinate we can neglect the Laplacian $\nabla_{CM}^2$ and write

$$\frac{1}{2m_B}\sum_i(\nabla_i^2 \prod f) + \frac{1}{2m_F}\sum_j(\nabla_j^2 \prod f) \xrightarrow{LOCV} \frac{1}{2m_r}\sum_{ij}(\nabla_{ij}^2 f_{ij})(\prod_{\alpha\beta\neq ij} f_{\alpha\beta}). \tag{2.25}$$

Thus within LOCV (in the thermodynamic limit), after another little manipulation the energy density (2.19) reads

$$\frac{\langle H_{BF}\rangle}{V} = \frac{N_F}{V}E_{FG} + \sum_{ij} \frac{\langle\Phi|\,[f_{ij}(-\frac{1}{2m_r}\nabla_{ij}^2 + U_{ij})f_{ij}](\prod_{\alpha\beta\neq ij} f_{\alpha\beta})^2\,|\Phi\rangle}{V\,\langle\Phi|\prod f \prod f\,|\Phi\rangle}. \tag{2.26}$$

In order to proceed we now employ an expansion in the small parameter $h \equiv f^2 - 1$ up to the first order, thus

$$(\prod_{\alpha\beta\neq ij} f_{\alpha\beta})^2 = \prod_{\alpha\beta\neq ij} f_{\alpha\beta}^2 = \prod_{\alpha\beta\neq ij}(1 + h_{\alpha\beta}) \simeq 1 + \sum_{\alpha\beta\neq ij} h_{\alpha\beta} + O(h^2). \tag{2.27}$$

The same kind of expansion is performed also in the denominator, we have

$$(\prod f)(\prod f) = \prod_{\alpha\beta} f_{\alpha\beta}^2 = \prod_{\alpha\beta}(1 + h_{\alpha\beta}) \simeq 1 + \sum_{\alpha\beta} h_{\alpha\beta} + O(h^2), \tag{2.28}$$

where now the sum runs on all possible couples without excluding the $ij$ one as in the numerator.

Making explicit $|\Phi\rangle$ back as $|\Phi_{BG}\rangle\,|\Phi_{FG}\rangle$, the energy density now takes the form

$$\begin{aligned}\frac{\langle H_{BF}\rangle}{V} &= \frac{N_F}{V}E_{FG} + \\ &+ \frac{1}{V}\sum_{ij} \frac{\langle\Phi_{FG}|\,\langle\Phi_{BG}|\,f_{ij}(-\frac{1}{2m_r}\nabla_{ij}^2 + U_{ij})f_{ij}(1 + \sum_{\alpha\beta\neq ij} h_{\alpha\beta})\,|\Phi_{BG}\rangle\,|\Phi_{FG}\rangle}{1 + \langle\Phi_{FG}|\,\langle\Phi_{BG}|\sum_{\alpha\beta} h_{\alpha\beta}\,|\Phi_{BG}\rangle\,|\Phi_{FG}\rangle}.\end{aligned} \tag{2.29}$$

Using Slater rules (A.13) the above expression is equal to

$$\begin{aligned}\frac{\langle H_{BF}\rangle}{V} =& \frac{N_F}{V}E_{FG} + \frac{1}{V^3}\sum_{ij}\frac{\int d^Dr_i d^DR_j[f_{ij}(-\frac{1}{2m_r}\nabla^2_{ij}+U_{ij})f_{ij}](1+\frac{1}{V^2}\sum_{\alpha\beta\neq ij}\int d^Dr_\alpha d^DR_\beta h_{\alpha\beta})}{1+\frac{1}{V^2}\sum_{\alpha\beta}\int d^Dr_\alpha d^DR_\beta h_{\alpha\beta}} \\ =& \frac{N_F}{V}E_{FG} + \frac{1}{V^2}\sum_{ij}\frac{\int d^Dx_{ij}[f_{ij}(-\frac{1}{2m_r}\nabla^2_{ij}+U_{ij})f_{ij}](1+\frac{1}{V}\sum_{\alpha\beta\neq ij}\int d^Dx_{\alpha\beta}h_{\alpha\beta})}{1+\frac{1}{V}\sum_{\alpha\beta}\int d^Dx_{\alpha\beta}h_{\alpha\beta}} \\ =& \frac{N_F}{V}E_{FG} + \frac{1}{V^2}\sum_{ij}\frac{\int d^Dxf(x)[-\frac{1}{2m_r}\nabla^2_x+U_{BF}(x)]f(x)}{1+\frac{1}{V}\sum_{\alpha\beta}\int d^Dyh(y)}[1+\frac{1}{V}\sum_{\alpha\beta\neq ij}\int d^3yh(y)].\end{aligned} \tag{2.30}$$

Now assuming $\left|\frac{1}{V}\sum_{\alpha\beta\neq ij}\int d^Dyh(y)\right| < 1$ we can use the geometric series $\frac{1}{1-x} \simeq 1 + x + O(x^2)$ to bring the denominator above and be able to make cancellations

$$\begin{aligned}\frac{1+\frac{1}{V}\sum_{\alpha\beta\neq ij}\int d^Dyh(y)}{1+\frac{1}{V}\sum_{\alpha\beta}\int d^Dyh(y)} &\simeq [1+\frac{1}{V}\sum_{\alpha\beta\neq ij}\int d^Dyh(y)][1-\frac{1}{V}\sum_{\alpha\beta}\int d^Dyh(y)] \\ &\simeq 1-\frac{1}{V}\int d^Dyh(y)+O(h^2).\end{aligned} \tag{2.31}$$

As this term tends to 1 in the thermodynamic limit, we are left with

$$\begin{aligned}\frac{\langle H_{BF}\rangle}{V} =& \frac{N_F}{V}E_{FG} + \frac{1}{V^2}\sum_{ij}\int d^Dxf(x)[-\frac{1}{2m_r}\nabla^2_x+U_{BF}(x)]f(x) \\ =& \frac{N_F}{V}E_{FG} + \frac{N_BN_F}{V^2}\int d^Dxf(x)[-\frac{1}{2m_r}\nabla^2_x+U_{BF}(x)]f(x).\end{aligned} \tag{2.32}$$

Therefore, within the LOCV approximation, the variational expectation value for the energy density of a Bose-Fermi mixture at $T = 0\ K$ reads

$$\begin{aligned}\frac{\langle H_{BF}\rangle}{V} &= n_FE_{FG} + n_Bn_F\int d^Dxf(x)[-\frac{1}{2m_r}\nabla^2_x+U_{BF}(x)]f(x) \\ &= \mathcal{E}^0_F + \mathcal{E}_{BF},\end{aligned} \tag{2.33}$$

where we made explicit the dependence on the boson and fermion densities $n_B = N_B/V$, $n_F = N_F/V$.

# Chapter 3

# Variational Study of Bose-Fermi Mixtures Using the LOCV Approach

The study of Bose-Fermi mixtures has attracted considerable attention due to the rich interplay between bosonic coherence and fermionic statistics. In this chapter, we apply the Lowest Order Constrained Variational (LOCV) method, introduced in the previous chapter, to explore the behaviour of such mixtures in both three and two spatial dimensions.

We focus on how two-body Bose-Fermi correlations influence the properties of the system by solving the LOCV equations derived from a Jastrow-Slater variational ansatz. This approach captures the atomic (non-molecular) phase of the mixture and provides direct access to the correlation functions $f(r)$ and associated energetic quantities.

## 3.1 3D LOCV equation

Although we do not yet possess an explicit analytic expression for the Bose-Fermi correlation function $f(x)$, we can exploit its known qualitative behaviour. In particular, since $f(x)$ becomes flat beyond the healing distance $d$, we can confidently assume that

$$\nabla_x^2 f(x) \to 0 \qquad \forall x > d. \tag{3.1}$$

Furthermore, considering that the Bose-Fermi potential $U_{BF}(x)$ is short-ranged, it is reasonable to neglect the contribution of the interaction energy beyond the healing distance. In other words, we assume

$$\int_{|\vec{x}|=d}^{\infty} d^3x\, f(x)^2 U_{BF}(x) \approx 0. \tag{3.2}$$

This allows us to treat $d$ as an effective cut-off for the interaction energy integral $\mathcal{E}_{BF}$ between bosons and fermions.

$$\mathcal{E}_{BF} \to n_B n_F \int_{|\vec{x}|\leq d} d^3x f(x)[-\frac{1}{2m_r}\nabla_x^2 + U_{BF}(x)]f(x). \tag{3.3}$$

Now if we interpret $f(r)$ as the wave-function of a Bose-Fermi pair, we can express the average number of fermions within distance $d$ of a boson with

$$P(d) = n_F \int_{|\vec{x}|\leq d} d^3x |f(x)|^2. \tag{3.4}$$

We want to set $P(d) \equiv 1$ as a constraint, such that on average only one fermion lies in a sphere with radius $d$ around a boson.

We act now on $\mathcal{E}_{BF}$ (3.3) with a functional derivative $\frac{\delta}{\delta f(x)}$ imposing such constraint with $\lambda n_B$ as a Lagrange multiplier and the derivative will then be set to zero in order to find the Euler-Lagrange equation for the $f(x)$ that minimizes the variational energy density of the mixture. By doing so we get the LOCV equation of the B-F mixture, which reads

$$\big[-\frac{1}{2m_r}\nabla_x^2 + U_{BF}(x)\big]f(x) = \lambda f(x), \tag{3.5}$$

where it is straightforward to interpret $\lambda$ as the pair interaction energy.

In 3 dimensions the LOCV equation can be easily rewritten as a one dimensional Schroedinger problem via the substitution $u(x) = xf(x)$ leading to

$$\big[-\frac{1}{2m_r}\frac{d^2}{dx^2} + U_{BF}(x)\big]u(x) = \lambda u(x), \tag{3.6}$$

which is much easier to tackle.

The LOCV (healing) boundary conditions get now reframed into:

$$f(d) = 1, \quad f'(d) = 0 \to u(d) = d, \quad u'(d) = 1. \tag{3.7}$$

For non trivial finite range potentials, the solution of the LOCV equation can be obtained by numerical integration methods; however in the dilute limit the details of the interaction can be ignored, as discussed in Section 1.6, hence simplifying the potential as a contact interaction $U_{BF}(x) = U_0\delta(x)$ is a valid choice. The Schroedinger problem can be recast as that of a free particle with a specific boundary condition at the origin, called Bethe-Peierls boundary condition [26], which reads

$$\frac{(rf)'}{rf}\bigg|_0 = \frac{u'(0)}{u(0)} = -\frac{1}{a}, \tag{3.8}$$

where $a$ is the $3D$ s-wave scattering length of the B-F interaction.

### 3.1.1 Attractive regime

In the attractive scenario ($\lambda < 0$) the general solution of the equation (3.6) with the LOCV boundary conditions (3.7) reads

$$u(r) = \frac{1}{2}\big[\big(d + \frac{1}{k}\big)e^{k(r-d)} + \big(d - \frac{1}{k}\big)e^{-k(r-d)}\big], \tag{3.9}$$

where $k = \sqrt{-2m_r\lambda}$. It is important to notice that this wave-function does not intersect the $r$-axis, that is it has 0 nodes.

The Bethe-Peierls boundary condition gives now the dependence of $k$ on $d$ through the scattering length $a$, so we get

$$e^{-2\gamma d} = \frac{1-ka}{1+ka}\,\frac{1-kd}{1+kd}. \tag{3.10}$$

Lastly, the constrain $P(d) = 1$ imposes

$$\big(d - \frac{1}{k}\big)^2 e^{2kd} - \big(d + \frac{1}{k}\big)^2 e^{-2kd} + 4kd^3 = \frac{2k}{\pi n_F}. \tag{3.11}$$

The density of the (spinless) fermion gas is set to $n_F = \frac{k_F^3}{6\pi^2}$, so by introducing to the dimensionless parameters $\eta = \frac{1}{k_F a}$, $\bar{d} = dk_F$, $\bar{k} = \frac{k}{k_F}$ we can write the following dimensionless constraints:

$$e^{-2\bar{k}\bar{d}} = \frac{1-\frac{\bar{k}}{\eta}}{1+\frac{\bar{k}}{\eta}}\,\frac{1-\bar{k}\bar{d}}{1+\bar{k}\bar{d}}, \tag{3.12}$$

$$\big(\bar{d} - \frac{1}{\bar{k}}\big)^2 e^{2\bar{k}\bar{d}} - \big(\bar{d} + \frac{1}{\bar{k}}\big)^2 e^{-2\bar{k}\bar{d}} + 4\bar{k}\bar{d}^3 = 12\pi\bar{k}. \tag{3.13}$$

We can numerically solve these two coupled equations as $\eta$ varies from weak to strong coupling, obtaining $\bar{d}(\eta)$, $\bar{k}(\eta)$ as functions of the single variable $\eta$.

Once the numerical solutions for $\bar{d}(\eta)$ and $\bar{k}(\eta)$ are obtained, they can be inserted into (3.9) to generate, upon dividing by $r$, the explicit correlation functions $f_\eta(r)$ for each value of $\eta$. These functions are shown in Fig. 3.1.

In Fig. 3.2, the rescaled plot as a function of $r/d$ clearly demonstrates that the Bethe-Peierls boundary condition is correctly enforced. Specifically, in the limit $r \to 0$, the correlation function diverges as const$/r$, so that the product $rf(r)$ tends to a finite constant.

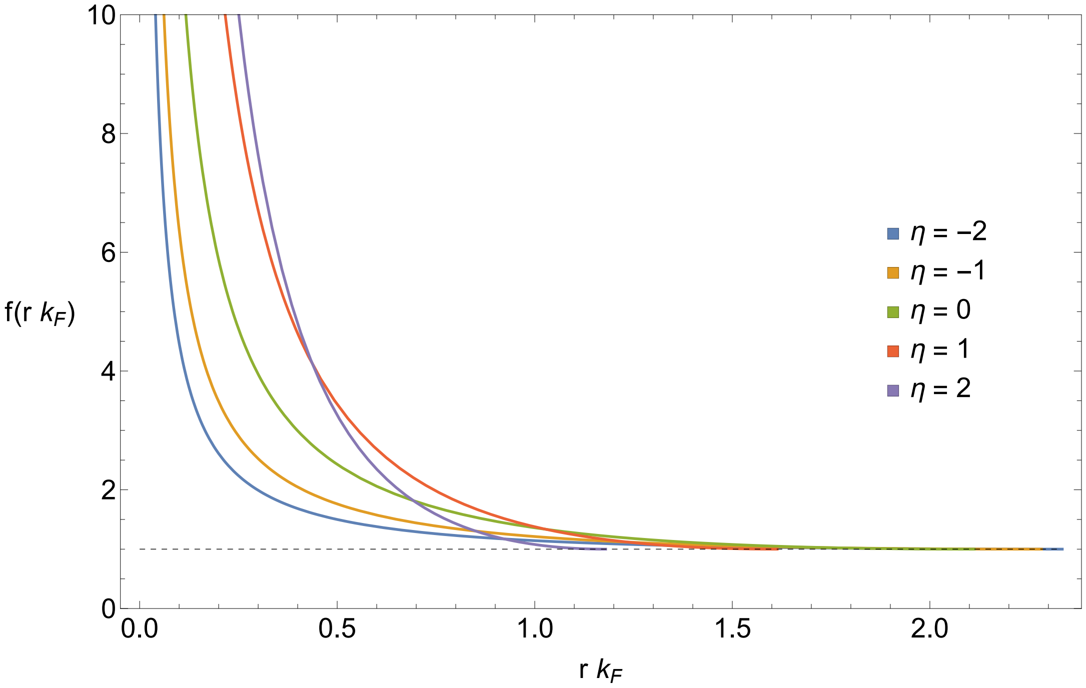

Figure 3.1: Correlation function $f(r)$ for the attractive regime in three dimensions, shown for five representative interaction strengths: from $\eta = -2$ (weak attraction) to $\eta = 2$ (strong attraction). The plots illustrate how increasing attraction enhances the short-range structure and causes the healing length to become progressively shorter.

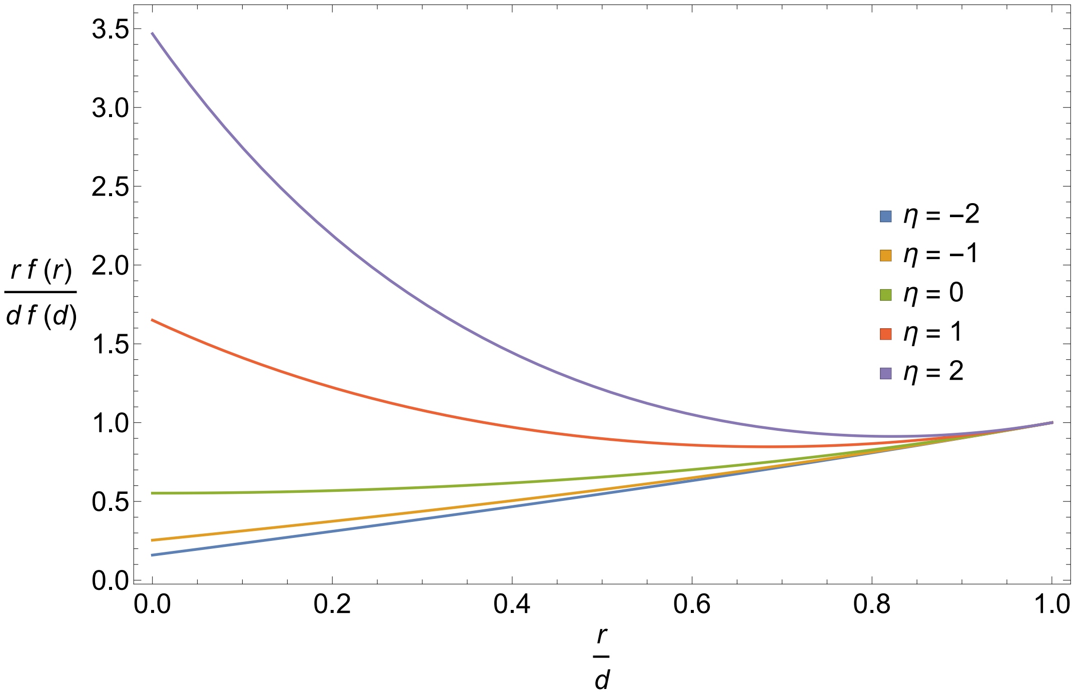

Figure 3.2: Rescaled correlation function $\frac{r}{d}\frac{f(r)}{f(d)}$ plotted as a function of the normalized distance $r/d$ for the attractive regime in three dimensions. The curves are shown for five representative values of $\eta$ ranging from $-2$ to 2. All curves are normalized to end at the common point $(1, 1)$.

### 3.1.2 Repulsive regime

In the repulsive scenario ($\lambda > 0$) the general solution of the $3D$ LOCV equation, with the healing boundary conditions applied, reads

$$u(r) = d\cos[\kappa(r-d)] - \frac{1}{\kappa}\sin[\kappa(r-d)], \tag{3.14}$$

where $\kappa = \sqrt{2m_r\lambda}$; this solution can be easily derived from (3.9) by sending $k \to -i\kappa$. This wave-function intersects the $r$-axis once and these are the 1-node solutions. Other repulsive solutions with more than 1 node could exist and they would describe other excited states.

By following the same procedure performed above we get the dimensionless constraints:

$$\frac{\eta}{\bar{\kappa}} = \frac{\cos\big(\bar{d}\bar{\kappa}\big) + \bar{d}\bar{\kappa}\sin\big(\bar{d}\bar{\kappa}\big)}{\sin\big(\bar{d}\bar{\kappa}\big) - \bar{d}\bar{\kappa}\cos\big(\bar{d}\bar{\kappa}\big)}, \tag{3.15}$$

$$2(\bar{d}\bar{\kappa})^3 + 2(\bar{d}\bar{\kappa})\cos\big(2\bar{d}\bar{\kappa}\big) + [(\bar{d}\bar{\kappa})^2 - 1]\sin\big(2\bar{d}\bar{\kappa}\big) = 6\pi\bar{\kappa}^3. \tag{3.16}$$

As in the attractive regime, we can numerically solve these two coupled equations as $\eta$ varies from weak to strong coupling, obtaining $\bar{\kappa}(\eta)$, $\bar{d}(\eta)$ as functions of the single variable $\eta$, now associated to the repulsive case.

Once the numerical solutions for $\bar{d}(\eta)$ and $\bar{\kappa}(\eta)$ are obtained, they can be inserted into (3.14) to generate, upon dividing by $r$, the explicit correlation functions $f_\eta(r)$ for each value of $\eta$. These functions are shown in Fig. 3.3.

In Fig. 3.4, the rescaled plot as a function of $r/d$ clearly demonstrates that the Bethe-Peierls boundary condition is correctly enforced. Specifically, in the limit $r \to 0$, the correlation function diverges as const$/r$, so that the product $rf(r)$ tends to a finite constant.

In addition to the LOCV correlation functions, we also compare the resulting pair correlation function $g(r) = f(r)^2$ with quantum Monte Carlo (QMC) data from Ref. [16], as shown in Fig. 3.5.[1] The comparison is performed at $\eta = 2$, where the LOCV framework is expected to be most reliable. The excellent agreement confirms the accuracy of the variational ansatz in capturing two-body correlations within the

---

[1] The comparison between the LOCV Bose-Fermi framework and quantum Monte Carlo data of a Fermi-Fermi mixture at finite concentration needs to be justified properly. The physical motivation of why this comparison holds lies in the fact that at weak coupling the dominant correlations in the quantum Monte Carlo simulation [16] are the inter-species correlations ($\uparrow$ fermions with $\downarrow$ fermions) while the intra-species correlations generate sub-leading terms. In our LOCV approach we have completely neglected intra-species correlations and only focused on the inter-species correlations, which are not affected by the underlying statistics of the particles. Therefore comparing the pair correlation function of a Bose-Fermi pair with the one of a Fermi $\uparrow\downarrow$ pair is reasonable, at least in weak coupling.

repulsive regime, and validates the LOCV method as a consistent approximation in the weak-coupling limit.

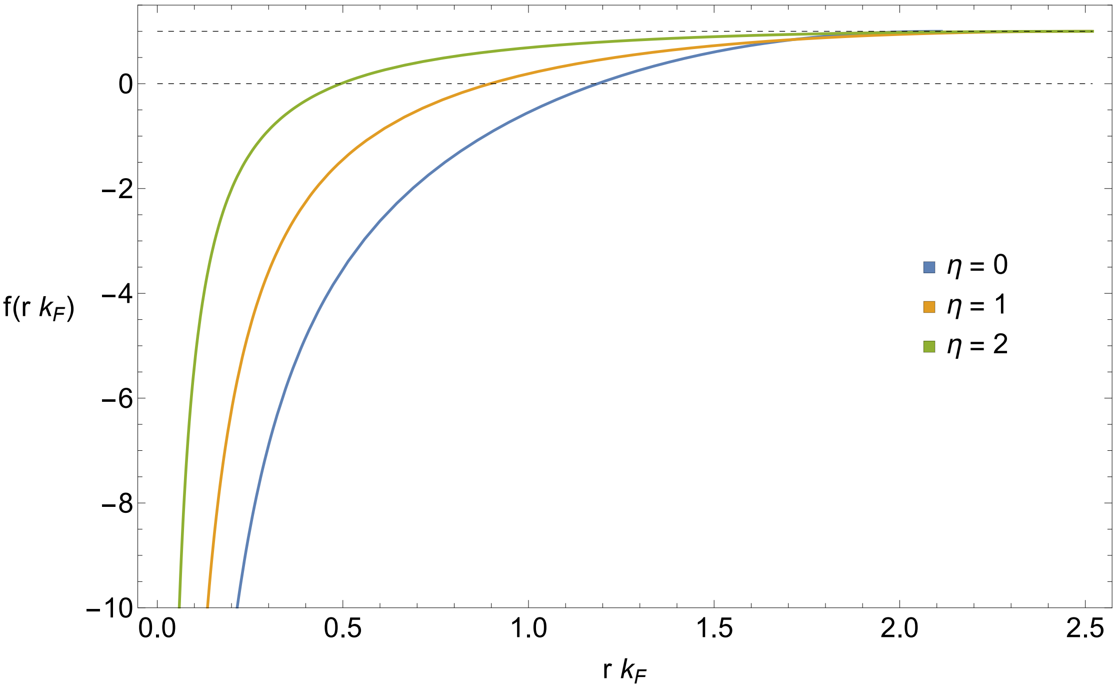

Figure 3.3: Correlation function $f(r)$ for the repulsive regime in three dimensions, shown for three representative interaction strengths: from $\eta = 0$ (strong repulsion) to $\eta = 2$ (weak repulsion). The plots illustrate how repulsive interactions induce a node in $f(r)$ and enhance short-range exclusion as the repulsion increases shifting the node to the right.

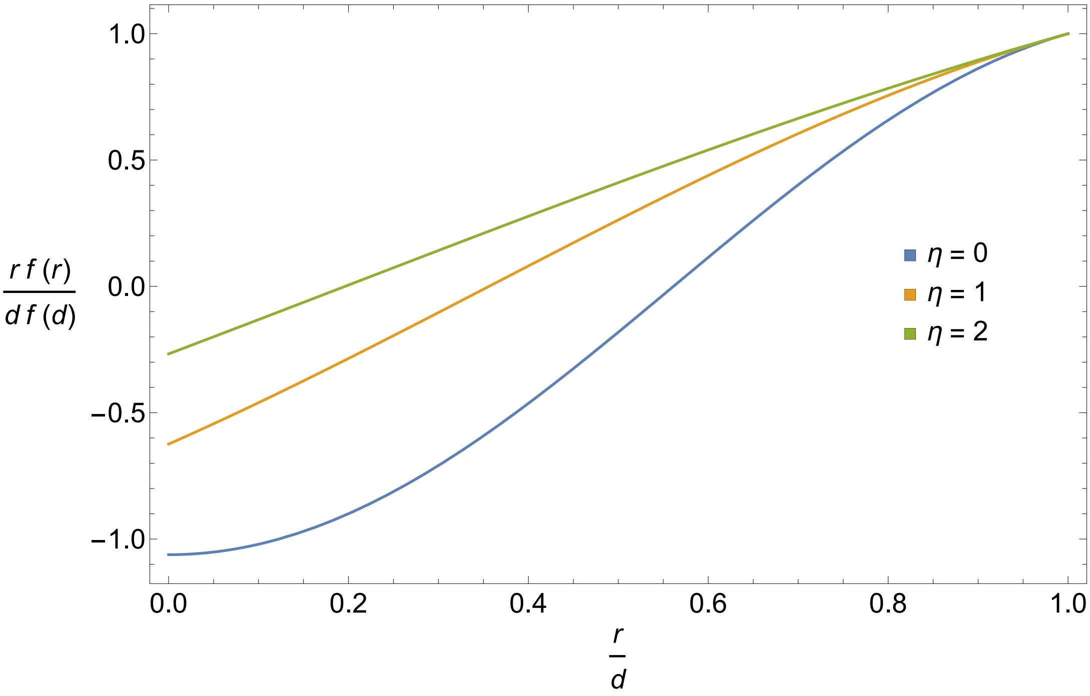

Figure 3.4: Rescaled correlation function $\frac{r}{d}\frac{f(r)}{f(d)}$ plotted as a function of the normalized distance $r/d$ for the repulsive regime in three dimensions. The curves are shown for three representative values of $\eta$ ranging from 0 to 2. All curves are normalized to end at the common point $(1, 1)$.

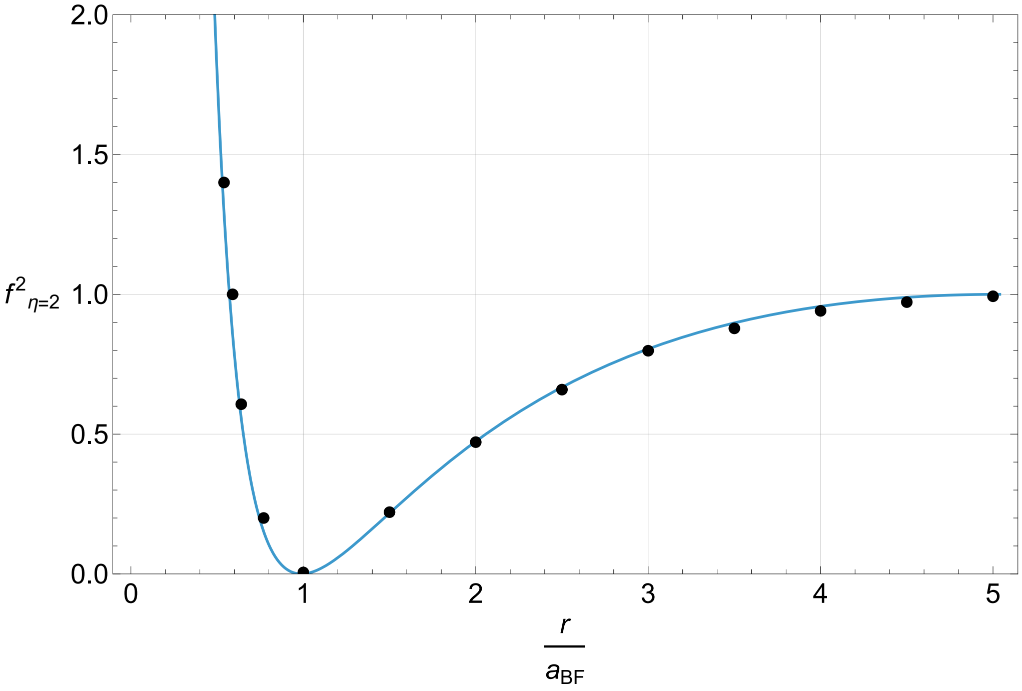

Figure 3.5: Comparison of the pair correlation function $g(r) = f(r)^2$ in the repulsive 3D case, evaluated at $\eta = 2$, with quantum Monte Carlo data points from [16].The horizontal axis is expressed in units of the scattering length $a_{BF}$ associated with $\eta = 2$.

## 3.2 3D Energy Branches

We now illustrate the behaviour of the energy branches in a 3D Bose-Fermi mixture by applying the LOCV approximation across interaction regimes.

From the energy density expression in Eq. (2.33), making use of the LOCV equation and the constraint $P(d) = 1$, we can express the energy density as

$$\begin{aligned}\frac{\langle H_{BF}\rangle}{V} &= \mathcal{E}_F^0 + n_B n_F \int d^3x\, f(x)\left(-\frac{1}{2m_r}\nabla_x^2 + U_{BF}(x)\right) f(x)\\ &= \mathcal{E}_F^0 + n_B n_F \lambda \int d^3x\, f^2(x) = \mathcal{E}_F^0 + n_B\lambda,\end{aligned} \tag{3.17}$$

where $\lambda$ is the pair interaction energy extracted from the effective two-body problem.

In the attractive regime, the solution corresponds to a bound state with energy

$$\lambda^- = -\frac{k^2}{2m_r} = \frac{1+b}{2b} A^-(\eta)\,\epsilon_F, \qquad A^-(\eta) = -2\bar{k}^2, \tag{3.18}$$

while in the repulsive regime, the scattering state gives

$$\lambda^+ = \frac{\kappa^2}{2m_r} = \frac{1+b}{2b} A^+(\eta)\,\epsilon_F, \qquad A^+(\eta) = 2\bar{\kappa}^2. \tag{3.19}$$

Here, $b = m_B/m_F$ is the boson-to-fermion mass ratio, $\epsilon_F = k_F^2/(2m_F)$ is the Fermi energy, and $\bar{k} = k/k_F$, $\bar{\kappa} = \kappa/k_F$ are the dimensionless wave-vectors corresponding to the attractive and repulsive solutions, respectively.

The function $A(\eta)$, expressed in terms of the interaction parameter $\eta = 1/(a_{BF}k_F)$, determines the energy shift due to the Bose-Fermi interaction. The branches $A^-(\eta)$ and $A^+(\eta)$ correspond to solutions of the LOCV equation with zero and one node, respectively, in the two-body wave-function $f(r)$. $A^-(\eta)$, in particular, represents the dimensionless polaron binding energy [29],[5]. Higher branches exist in principle, corresponding to higher order excited states (more nodes), but they are generally less relevant for the ground-state physics and are not shown here. The two lowest energy branches obtained within LOCV are shown in Fig. 3.6. Both the $A^+(\eta)$ and $A^-(\eta)$ curves show good agreement with the known perturbative benchmarks [30]

$$A^+(\eta) \to \frac{4}{3\pi\eta}\left(1 + \frac{3}{2\pi\eta}\right) \quad \text{for} \quad \eta \gg 1, \tag{3.20}$$

$$A^-(\eta) \to \frac{4}{3\pi\eta}\left(1 + \frac{3}{2\pi\eta}\right) \quad \text{for} \quad \eta \ll 1, \tag{3.21}$$

in the weak coupling regime.

In particular, the $A^-(\eta)$ curve approaches the binding energy

$$A^-(\eta) \to E_B = -2\eta^2 \quad \text{for} \quad \eta \gg 1, \tag{3.22}$$

in the strong coupling limit.

To further validate the LOCV predictions, we compare the repulsive branch $A^+(\eta)$ with experimental measurements reported in Ref. [31]. As shown in Fig. 3.7, the LOCV result accurately reproduces the experimental data in the weakly interacting regime ($\eta \gtrsim 1$), confirming the reliability of the method in this perturbative limit. However, as the interaction strength increases and $\eta \to 0^+$, a growing discrepancy emerges: the LOCV curve overestimates the interaction energy, predicting a value more than twice as large as that observed in the experiment. This deviation highlights the limitations of the LOCV approach near the unitary regime, where correlations beyond the two-body level become increasingly relevant; moreover the discrepancy is likely due to neglected dynamical effects involving the average momentum of the impurity, which in this work is set to zero.

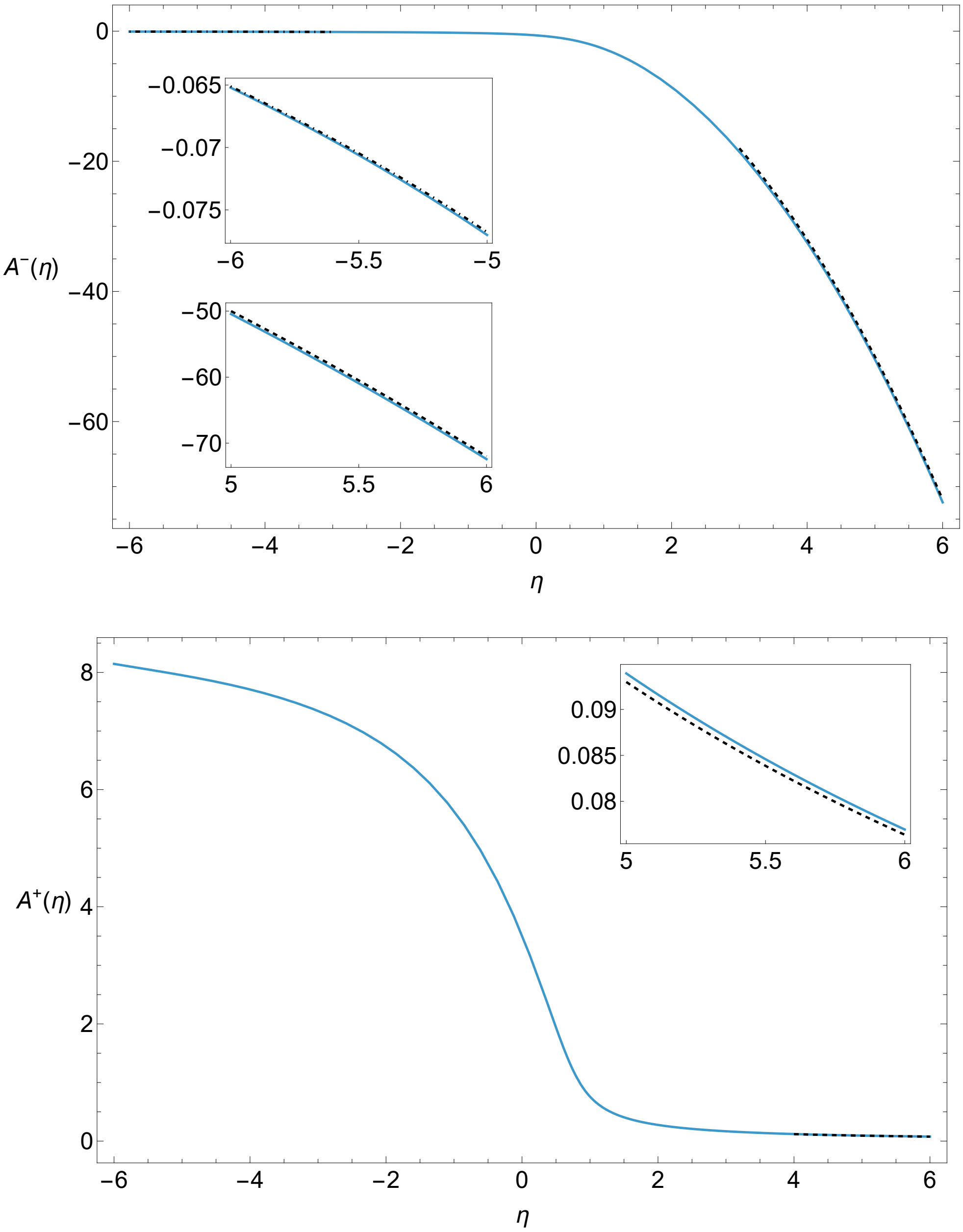

Figure 3.6: Dimensionless interaction energy per Bose-Fermi pair in the attractive ($A^{-}(\eta)$, top) and repulsive ($A^{+}(\eta)$, bottom) regimes, plotted as functions of the interaction parameter $\eta = 1/(a_{BF}k_F)$. These curves represent the first two solutions of the LOCV equation corresponding to correlation functions with zero and one node. The various insets highlight weak and strong coupling regions. The dashed curves show the weak coupling perturbative benchmarks (3.20,3.21). The dot-dashed curve shows the binding energy benchmark at strong coupling (3.22).

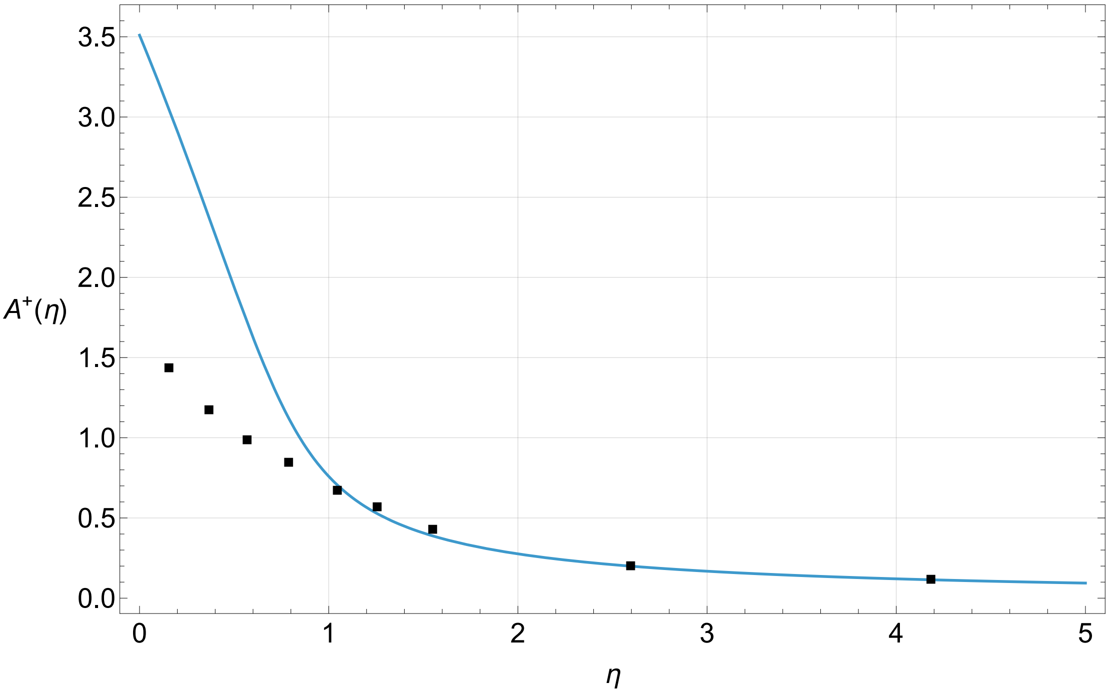

Figure 3.7: Comparison of the LOCV repulsive branch in the 3D case with experimental data points from [31]. The theoretical curve shows good agreement with the experimental data in the weak coupling regime, while a discrepancy is observed approaching the unitary limit.

## 3.3 3D Mixture stability

The Bose-Fermi mixture described by the Hamiltonian (2.16) is unstable at zero temperature, as the total energy can be indefinitely lowered by compressing the system, that is by reducing the volume. To prevent this collapse and ensure mechanical stability, it is necessary to include an additional boson-boson interaction term, $H_{BB}$, which provides sufficient repulsion among the bosons.

In the dilute limit, where the average inter-particle distance is much larger than the range of the interaction, it is sufficient to model the boson-boson interaction as a contact potential. The corresponding Hamiltonian takes the form

$$H_{BB} = \frac{1}{2}\sum_{\sigma\neq\sigma'} U_{BB}(\vec{r}_\sigma - \vec{r}_{\sigma'}) \xrightarrow{\text{dilute limit}} \frac{1}{2} g_{BB} \sum_{\sigma\neq\sigma'} \delta^{(3)}(\vec{r}_\sigma - \vec{r}_{\sigma'}), \tag{3.23}$$

where $g_{BB}$ is the effective boson-boson coupling constant, typically related to the scattering length via standard Born approximation.

### 3.3.1 Boson-Boson Interaction Energy and Depletion Effects

We now evaluate the expectation value of the boson-boson interaction term $H_{BB}$ using the Jastrow-Slater variational wave-function $|\Psi\rangle$. Specifically, we compute the quantity

$$\frac{\langle\Psi| H_{BB} |\Psi\rangle}{\langle\Psi|\Psi\rangle}.$$

This calculation goes beyond the pure mean-field approximation, incorporating the leading correction due to correlations between bosons and fermions. Instead of expanding in the small parameter $h \equiv f^2 - 1$ as was done for the calculation of (2.19), it is more convenient here to expand in $\ell \equiv f - 1$, which captures linearly the deviation of the correlation function from unity (the same calculation can be done also via an expansion in the parameter $h$ and gives the same result, it does however involve more steps).

Starting from the numerator, we find

$$\begin{aligned}\langle\Psi| H_1 |\Psi\rangle &= \int \Big(\prod_{\alpha=1}^{N_B} d^3 r_\alpha\Big) \frac{1}{V^{N_B}} \langle\Phi_{FG}| \Big(\prod_{ij} f_{ij}\Big) \sum_{\sigma\sigma'} \frac{1}{2} g_{BB} \delta^{(3)}(\vec{r}_\sigma - \vec{r}_{\sigma'}) \Big(\prod_{ij} f_{ij}\Big) |\Phi_{FG}\rangle \\ &= \frac{1}{V^{N_B}} \langle\Phi_{FG}| \Big[\frac{1}{2} g_{BB} \int \Big(\prod_{\alpha=1}^{N_B} d^3 r_\alpha\Big)\Big(\prod_{ij} f_{ij}\Big) \sum_{\sigma\sigma'} \delta^{(3)}(\vec{r}_\sigma - \vec{r}_{\sigma'}) \Big(\prod_{ij} f_{ij}\Big)\Big] |\Phi_{FG}\rangle .\end{aligned} \tag{3.24}$$

Now out of all the integrals on the bosonic coordinates, let us just consider the integration on the single variable $\vec{r}_{\sigma'}$ in order to get rid of the $\delta^{(3)}(\vec{r}_\sigma - \vec{r}_{\sigma'})$; so neglecting terms involving more than two bodies we get

$$
\begin{aligned}
&\frac{1}{2}g_{BB}\int d^3r_{\sigma'}\big(\prod_{ij} f_{ij}\big)\sum_{\sigma\sigma'}\delta^{(3)}(\vec{r}_\sigma-\vec{r}_{\sigma'})\big(\prod_{ij} f_{ij}\big) = \frac{1}{2}g_{BB}\sum_{\sigma\sigma'}\prod_{j}\big[f_{\sigma j}^2\prod_{i\neq\sigma\sigma'} f_{ij}\big]^2 \\
&= \frac{1}{2}g_{BB}\sum_{\sigma\sigma'}\prod_{j}\big[f_{\sigma j}^4\prod_{i\neq\sigma\sigma'} f_{ij}^2\big] = \frac{1}{2}g_{BB}\sum_{\sigma\sigma'}\prod_{j}\big[(1+l_{\sigma j})^4\prod_{i\neq\sigma\sigma'}(1+l_{ij})^2\big] \\
&= \frac{1}{2}g_{BB}\sum_{\sigma\sigma'}\prod_{j}\big[(1+4l_{\sigma j}+6l_{\sigma j}^2+O(l^3))\prod_{i\neq\sigma\sigma'}(1+2l_{ij}+l_{ij}^2)\big] \\
&\simeq \frac{1}{2}g_{BB}\sum_{\sigma\sigma'}\prod_{j}\big[(1+4l_{\sigma j}+6l_{\sigma j}^2)(1+\sum_{i\neq\sigma\sigma'}(2l_{ij}+l_{ij}^2))\big] \\
&\simeq \frac{1}{2}g_{BB}\sum_{\sigma\sigma'}\prod_{j}\big[1+4l_{\sigma j}+6l_{\sigma j}^2+\sum_{i\neq\sigma\sigma'}(2l_{ij}+l_{ij}^2)\big] \\
&\simeq \frac{1}{2}g_{BB}\sum_{\sigma\sigma'}\big[1+\sum_{j}(4l_{\sigma j}+6l_{\sigma j}^2+\sum_{i\neq\sigma\sigma'}(2l_{ij}+l_{ij}^2))\big]
\end{aligned}
\tag{3.25}
$$

Now we must apply the Slater rules (A.13) in order to calculate the expectation value of these contributions on the Fermi sphere

$$
\begin{aligned}
\langle\Psi|\,H_{BB}\,|\Psi\rangle &= \frac{1}{V^{N_B}}\,\langle\Phi_{FG}|\,\big[\frac{1}{2}g_{BB}\int\big(\prod_{\alpha=1}^{N_B}d^3r_\alpha\big)\big(\prod_{ij} f_{ij}\big)\sum_{\sigma\sigma'}\delta^{(3)}(\vec{r}_\sigma-\vec{r}_{\sigma'})\big(\prod_{ij} f_{ij}\big)\big]\,|\Phi_{FG}\rangle \\
&\simeq \frac{1}{V^{N_B}}\int\big(\prod_{\alpha\neq\sigma'}d^3r_\alpha\big)\,\langle\Phi_{FG}|\,\frac{1}{2}g_{BB}\sum_{\sigma\sigma'}\big[1+\sum_{j}(4l_{\sigma j}+6l_{\sigma j}^2+\sum_{i\neq\sigma\sigma'}(2l_{ij}+l_{ij}^2))\big]\,|\Phi_{FG}\rangle \\
&= \frac{1}{2}g_{BB}\frac{1}{V^{N_B}}\int\big(\prod_{\alpha\neq\sigma'}d^3r_\alpha\big)\sum_{\sigma\sigma'}\big[1+\frac{1}{V}\int d^3R_j\sum_{j}(4l_{\sigma j}+6l_{\sigma j}^2+\sum_{i\neq\sigma\sigma'}(2l_{ij}+l_{ij}^2))\big] \\
&= \frac{1}{2V}g_{BB}\sum_{\sigma\sigma'}\big[1+\frac{1}{V^2}\sum_{j}\int d^3r_\sigma d^3R_j(4l_{\sigma j}+6l_{\sigma j}^2)+\frac{1}{V^2}\sum_{j}\sum_{i\neq\sigma\sigma'}\int d^3r_i d^3R_j(2l_{ij}+l_{ij}^2))\big] \\
&= \frac{1}{2V}g_{BB}\sum_{\sigma\sigma'}\big[1+\frac{1}{V}\sum_{j}\int d^3r[4l(r)+6l(r)^2]+\frac{1}{V}\sum_{j}\sum_{i\neq\sigma\sigma'}\int d^3r[2l(r)+l(r)^2]\big] \\
&= \frac{1}{2}g_{BB}\frac{N_B^2}{V}\big[1+\frac{N_F}{V}\int d^3r[4l(r)+6l(r)^2]+\frac{N_F(N_B-2)}{V}\int d^3r[2l(r)+l(r)^2]\big]
\end{aligned}
\tag{3.26}
$$

The denominator is much easier to tackle and the calculation goes as

$$\begin{aligned}
\langle\Psi|\Psi\rangle &= \int \big(\prod_{\alpha=1}^{N_B} d^3r_\alpha\big)\frac{1}{V^{N_B}}\,\langle\Phi_{FG}|\,\big(\prod_{ij} f_{ij}\big)\big(\prod_{ij} f_{ij}\big)\,|\Phi_{FG}\rangle \\
&= \frac{1}{V^{N_B}}\int \big(\prod_{\alpha=1}^{N_B} d^3r_\alpha\big)\,\langle\Phi_{FG}|\prod_{ij}\big(1+l_{ij}\big)^2\,|\Phi_{FG}\rangle \\
&\simeq \frac{1}{V^{N_B}}\int \big(\prod_{\alpha=1}^{N_B} d^3r_\alpha\big)\,\langle\Phi_{FG}|\,\big(1+\sum_{ij}(2l_{ij}+l_{ij}^2)\big)\,|\Phi_{FG}\rangle \\
&= \frac{1}{V^{N_B}}\int \big(\prod_{\alpha=1}^{N_B} d^3r_\alpha\big)\big(1+\frac{1}{V}\sum_{ij}\int d^3R_j(2l_{ij}+l_{ij}^2)\big) \\
&= 1+\frac{1}{V^2}\sum_{ij}\int d^3r_i d^3R_j(2l_{ij}+l_{ij}^2) = 1+\frac{N_BN_F}{V}\int d^3r[2l(r)+l(r)^2]
\end{aligned} \tag{3.27}$$

The contribution from the integral of $l(r)$ and $l(r)^2$ is small, so using the geometric series we can write

$$\frac{1}{\langle\Psi|\Psi\rangle} \simeq 1-\frac{N_BN_F}{V}\int d^3r[2l(r)+l(r)^2] \tag{3.28}$$

Putting all together most of the terms cancel each other exactly and we are left with

$$\begin{aligned}
\frac{1}{V}\frac{\langle\Psi|\,H_{BB}\,|\Psi\rangle}{\langle\Psi|\Psi\rangle} &= \frac{1}{2}g_{BB}\frac{N_B^2}{V^2}\big[1+\frac{N_F}{V}\int d^3r[4l(r)+6l(r)^2]+ \\
&+\frac{N_F(N_B-2)}{V}\int d^3r[2l(r)+l(r)^2]-\frac{N_BN_F}{V}\int d^3r[2l(r)+l(r)^2]\big] \\
&= \frac{1}{2}g_{BB}\frac{N_B^2}{V^2}\big[1+4\frac{N_F}{V}\int d^3r\,l(r)^2\big] \\
&= \frac{1}{2}g_{BB}n_B^2\big[1+4n_F\int d^3r\,l(r)^2\big].
\end{aligned} \tag{3.29}$$

Now the integral that we are left with is related, in first approximation, to the quantum depletion of bosons $n_{dep}$ ([5][20],[32]) as a function of the B-F coupling

$$D(\eta) = \frac{n_{dep}}{n_B} = n_F\int d^3r\,l(r)^2 = n_F\int d^3r\,[f(r)-1]^2, \tag{3.30}$$

By using (3.9), we get that in the attractive case the fraction of depleted bosons reads

$$D^{-}(\eta) = 1 + \frac{2[(\bar{d}\bar{k})^3 - 6\bar{d}\bar{k}\cosh \bar{d}\bar{k} + 6\sinh \bar{d}\bar{k}]}{9\pi\bar{k}^3}, \tag{3.31}$$

while using (3.14), in the repulsive regime the depletion is

$$D^{+}(\eta) = 1 + \frac{2[(\bar{d}\bar{\kappa})^3 + 6\bar{d}\bar{\kappa}\cos \bar{d}\bar{\kappa} - 6\sin \bar{d}\bar{\kappa}]}{9\pi\bar{\kappa}^3}, \tag{3.32}$$

the plots of the curves are shown in Fig. 3.8.

The functions $D^{+}(\eta)$ and $D^{-}(\eta)$ describe the boson depletion across all coupling regimes. In the weak coupling regime, these functions follow the benchmarks [30]

$$D^{+}(\eta) \to \frac{2}{\pi^2\eta^2} \quad \text{for} \quad \eta \gg 1, \tag{3.33}$$

$$D^{-}(\eta) \to \frac{2}{\pi^2\eta^2} \quad \text{for} \quad \eta \ll 1, \tag{3.34}$$

A slight discrepancy can be observed when examining the functions in more detail. In particular, the depletion in the repulsive case exceeds unity at $\eta \approx 0.2$, which is unphysical. These discrepancies are likely due to the approximated formula (3.30) used for calculating the condensate fraction.

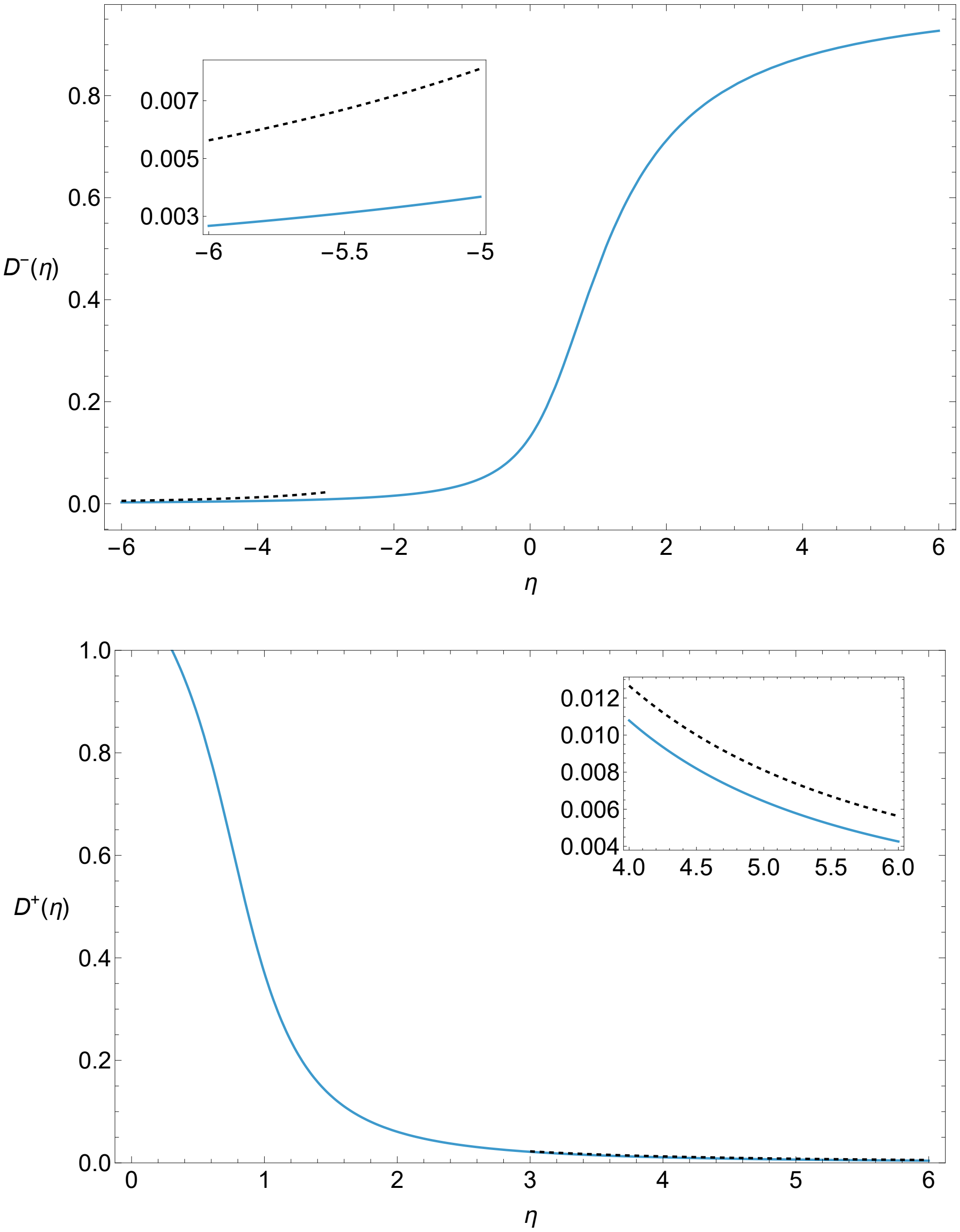

Figure 3.8: Relative quantum depletion of bosons in the attractive ($D^-(\eta)$, top) and repulsive ($D^+(\eta)$, bottom) regimes, plotted as functions of the interaction parameter $\eta = 1/(a_{BF}k_F)$. The insets highlight weak coupling regions. The dashed curves show the weak coupling perturbative benchmarks (3.33,3.34)

### 3.3.2 Chemical Potentials and Mechanical Stability

Including the perturbative correction due to boson-boson repulsion, the total energy density of the $3D$ Bose-Fermi mixture can be written as

$$\frac{E}{V}=\frac{3}{5}\epsilon_F n_F+\frac{1+b}{2b}A(\eta)\,\epsilon_F n_B+\frac{1}{2}g_{BB}n_B^2\left[1+4D(\eta)\right], \tag{3.35}$$

where the first term corresponds to the kinetic energy of the ideal Fermi gas, the second to the Bose-Fermi interaction energy as obtained via the LOCV method, and the third to the boson-boson interaction, corrected by the fermion-induced depletion through the function $D(\eta)$.

To compute the chemical potentials, we introduce the boson-to-fermion density ratio $x\equiv n_B/n_F$, and define the dimensionless parameter $\zeta\equiv k_F a_{BB}$, with the boson-boson coupling given by $g_{BB}=(4\pi a_{BB})/m_B$ [2]. Differentiating the energy density with respect to $n_F$ and $n_B$, we obtain the chemical potentials:

$$\mu_F=\frac{\partial}{\partial n_F}\left(\frac{E}{V}\right)=\epsilon_F\left\{1+\frac{1+b}{6b}\left[2A(\eta)-A'(\eta)\eta\right]x-\frac{8\zeta\eta}{9\pi b}D'(\eta)x^2\right\}, \tag{3.36}$$

$$\mu_B=\frac{\partial}{\partial n_B}\left(\frac{E}{V}\right)=\epsilon_F\left\{\frac{1+b}{2b}A(\eta)+\frac{4\zeta}{3\pi b}\left[1+4D(\eta)\right]x\right\}. \tag{3.37}$$

These expressions reflect how the chemical potentials depend on the interaction strength $\eta$, the mass ratio $b\equiv m_B/m_F$, the relative concentrations $x$, and the boson-boson scattering length via $\zeta$. The chemical potentials are shown in Fig. 3.9 and Fig. 3.10 for fixed $b=1$, $x=1$ and $\zeta=0.1$; in this regime their perturbative benchmarks for the weak coupling [30] read

$$\frac{\mu_F}{\epsilon_F}\to 1+\frac{4}{3\pi\eta}+\frac{8}{3\pi^2\eta^2}, \tag{3.38}$$

$$\frac{\mu_B}{\epsilon_F}\to\frac{4}{3\pi}0.1+\frac{4}{3\pi\eta}\left(1+\frac{3}{2\pi\eta}\right), \tag{3.39}$$

the LOCV curves show excellent agreement.

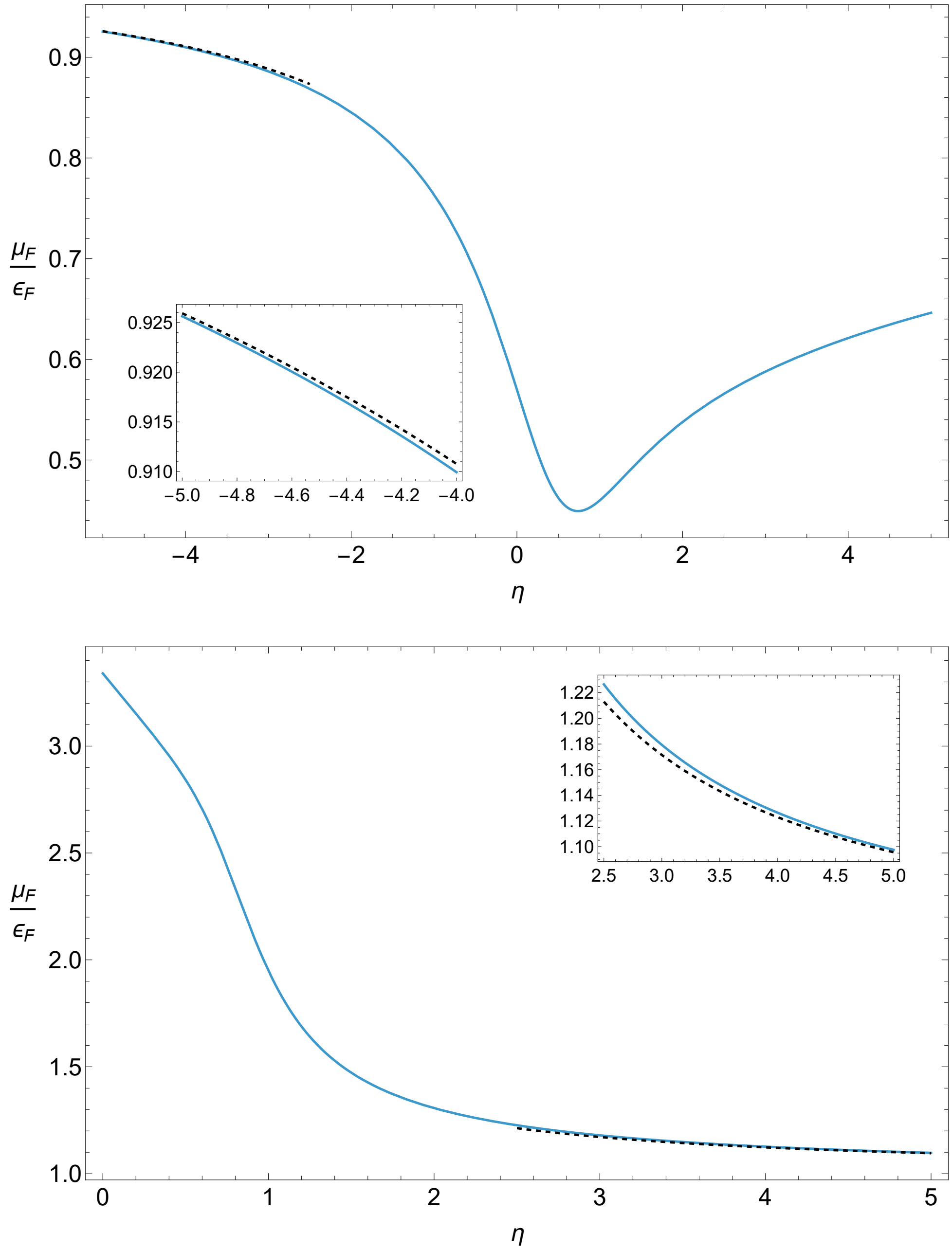

Figure 3.9: Fermionic chemical potential in the attractive (top) and repulsive (bottom) regimes, shown as functions of the interaction parameter $\eta$, with $b = 1$, $x = 1$ and $\zeta = 0.1$. The insets highlight weak coupling regions. The dashed curves show the weak coupling perturbative benchmark (3.38).

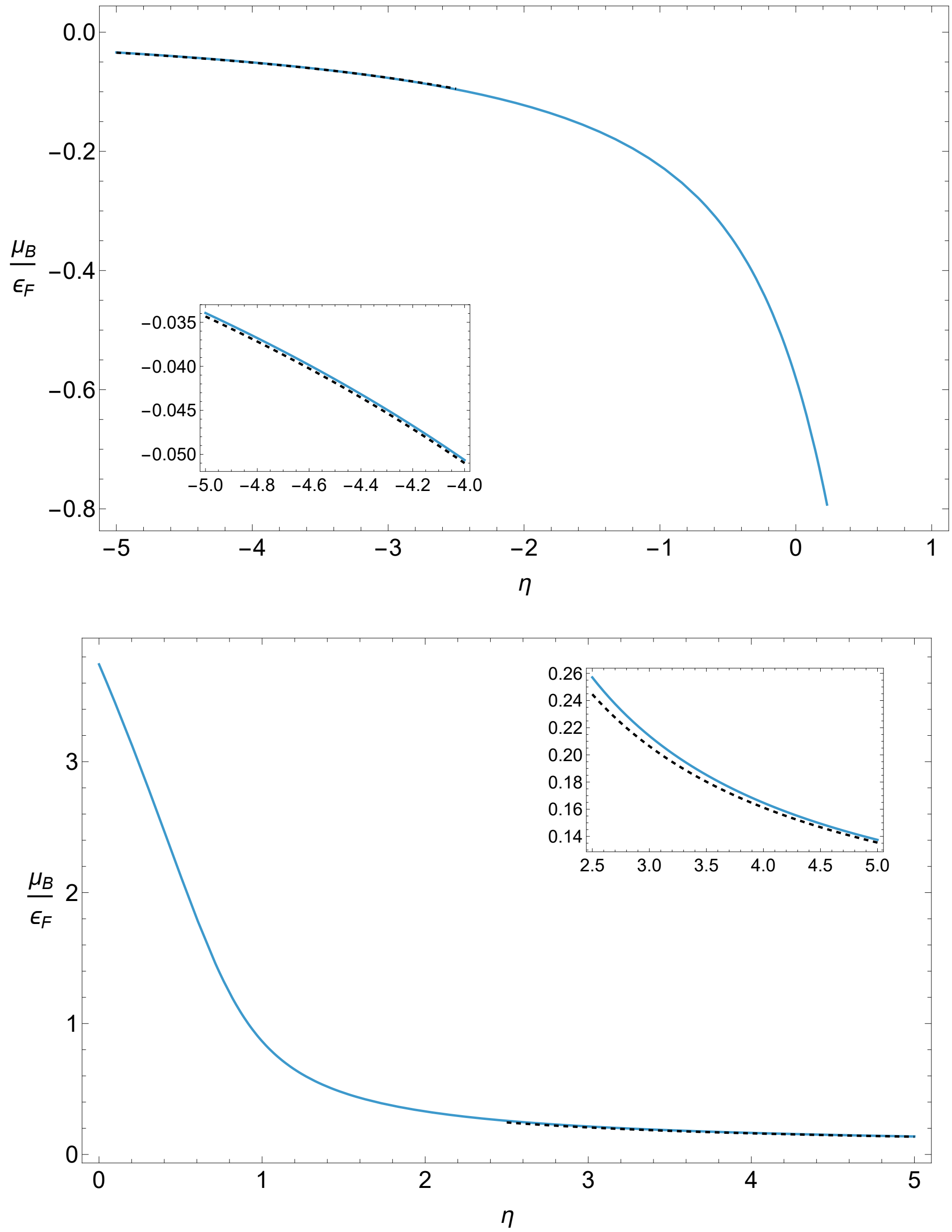

Figure 3.10: Bosonic chemical potential in the attractive (top) and repulsive (bottom) regimes, shown as functions of the interaction parameter $\eta$, with $b = 1$, $x = 1$ and $\zeta = 0.1$. The insets highlight weak coupling regions. The dashed curves show the weak coupling perturbative benchmark (3.39).

To assess the mechanical stability of the mixture, we evaluate the stability matrix:

$$M = \begin{pmatrix} \frac{\partial \mu_F}{\partial n_F} & \frac{\partial \mu_F}{\partial n_B} \\ \frac{\partial \mu_B}{\partial n_F} & \frac{\partial \mu_B}{\partial n_B} \end{pmatrix}. \tag{3.40}$$

Thermodynamic stability requires $M$ to be positive definite. This translates into the conditions:

$$\frac{\partial \mu_F}{\partial n_F} + \frac{\partial \mu_B}{\partial n_B} > 0 \quad \text{and} \quad \det(M) = \frac{\partial \mu_F}{\partial n_F}\frac{\partial \mu_B}{\partial n_B} - \frac{\partial \mu_F}{\partial n_B}\frac{\partial \mu_B}{\partial n_F} > 0. \tag{3.41}$$

We note that $\frac{\partial \mu_F}{\partial n_B}\frac{\partial \mu_B}{\partial n_F} > 0$, due to the thermodynamic identity $\frac{\partial \mu_F}{\partial n_B} = \frac{\partial \mu_B}{\partial n_F}$. The fulfilment of the second inequality in (3.41) then implies that $\frac{\partial \mu_F}{\partial n_F}$ and $\frac{\partial \mu_B}{\partial n_B}$ must have the same sign. The first inequality in (3.41) can then be replaced by $\frac{\partial \mu_F}{\partial n_F} > 0$, a requirement that, due to Fermi pressure, is always satisfied in our mixture. Therefore, our attention will focus on the second condition, $\det(M) > 0$, which is known to ensure stability against small density fluctuations in Bose-Fermi mixtures.

The results for the derivatives of the chemical potentials read

$$\frac{\partial \mu_F}{\partial n_F} = \frac{2\epsilon_F}{3n_F}\Big\{1 - \frac{1+b}{6b}\big[A(\eta) - \frac{1}{2}A''(\eta)\eta^2\big]x + \frac{8\zeta}{9\pi b}\big[2D'(\eta)\eta - \frac{1}{3}D''(\eta)\eta^2\big]x^2\Big\} \tag{3.42}$$

$$\frac{\partial \mu_B}{\partial n_B} = \frac{4\epsilon_F \zeta}{3n_F \pi b}\Big\{1 + 4D(\eta)\Big\} \tag{3.43}$$

$$\frac{\partial \mu_B}{\partial n_F} = \frac{\partial \mu_B}{\partial n_F} = \frac{\epsilon_F}{n_F}\Big\{\frac{1+b}{6b}\big[2A(\eta) - A'(\eta)\eta\big] - \frac{16\zeta\eta}{9\pi b}D'(\eta)x\Big\} \tag{3.44}$$

While the LOCV formalism is fully general in the boson-to-fermion density ratio $x = \frac{n_B}{n_F}$, previous studies such as [5] have explored only the small-$x$ limit to remain within the polaron regime. In the present work, however, we also explore the regime $x \sim 1$, where bosons and fermions are comparably dense, in order to understand the behaviour of the mixture beyond the polaron limit. This approach allows us to investigate many-body effects that are not captured near the polaron limit, although care must be taken in interpreting results in this regime.

In the polaron limit $x \to 0$ the critical value $\zeta_c$ for which $\det(M) > 0$ and thus the mixture is stable reads

$$\zeta_c(\eta, \gamma) = \frac{\pi(1+b)^2}{32b}\frac{\big[2A(\eta) - A'(\eta)\eta\big]^2}{\big[1 + 4D(\eta)\big]} \tag{3.45}$$

For $x > 0$, the analytical result for $\zeta_c$ is very notation heavy and for a fixed $\eta$ the determinant of the stability matrix is a parabola in $\zeta$

$$\det(M(\zeta)) = \left(\frac{\epsilon_F}{n_F}\right)^2 \big[c_0 + c_1\zeta + c_2\zeta^2\big], \tag{3.46}$$

where the coefficients take the values

$$c_0(\eta, b) = -\left(\frac{1+b}{6b}\right)^2 [2A(\eta) - A'(\eta)\eta] \tag{3.47}$$

$$\begin{aligned} c_1(\eta, b, x) = \; & \frac{8}{9\pi b}[1+4D(\eta)] + \frac{16x(1+b)}{27\pi b^2}[2A(\eta) - A'(\eta)\eta]D'(\eta)\eta \\ & - \frac{4x(1+b)}{27\pi b^2}[1+4D(\eta)][A(\eta) - \frac{1}{2}A''(\eta)\eta^2] \end{aligned} \tag{3.48}$$

$$c_2(\eta, b, x) = \left(\frac{8x}{9\pi b}\right)^2 [1+4D(\eta)][2D'(\eta) - \frac{1}{3}D''(\eta)\eta^2] - \left(\frac{16x}{9\pi b}\right)^2 (D'(\eta)\eta)^2 \tag{3.49}$$

Fig. 3.11 illustrates the mechanical stability condition for a three-dimensional Bose-Fermi mixture in both the attractive and repulsive regimes as solutions to $\det(M(\zeta)) > 0$. In these plots, the horizontal axis shows the dimensionless interaction parameter $\eta = 1/(k_F a_{BF})$, while the vertical axis reports $\zeta = k_F a_{BB}$, which characterizes the strength of the boson-boson interaction. The LOCV approximation predicts stability for values of $\zeta$ above the curves.

In the attractive case, the blue curve corresponding to $x = 0$ reproduces the well-known result by Zhai [5], describing the polaron limit. The present work extends this analysis by exploring finite concentrations $x > 0$. It is evident that as $x$ increases, the critical value $\zeta_c$ required to ensure mechanical stability decreases progressively, and the position of the local maximum shifts slightly towards higher $\eta$. This trend reflects the enhanced effect of boson-boson repulsion in stabilizing the mixture at finite boson density.

Conversely, in the repulsive case, the curves show a distinct behaviour: they rapidly diverge when approaching the unitary limit $\eta = 0$ from the right, indicating that stronger boson-boson repulsion is needed to counteract the attractive correlations that emerge near unitarity. Unlike the attractive case, increasing $x$ in the repulsive regime leads to a higher $\zeta_c$, highlighting the greater tendency towards mechanical collapse in the presence of more bosons when the Bose-Fermi interaction is repulsive.

Both sets of curves asymptotically recover the weak-coupling perturbative benchmark,

$$\zeta_c \to \frac{2}{\pi\eta^2}\left(1 + \frac{2}{\pi\eta}\right)^2, \tag{3.50}$$

which applies for equal masses and vanishing boson concentration ($x = 0$) [9]. Specifically, the attractive branch matches this prediction for large negative $\eta$, while the repulsive branch does so for large positive $\eta$.

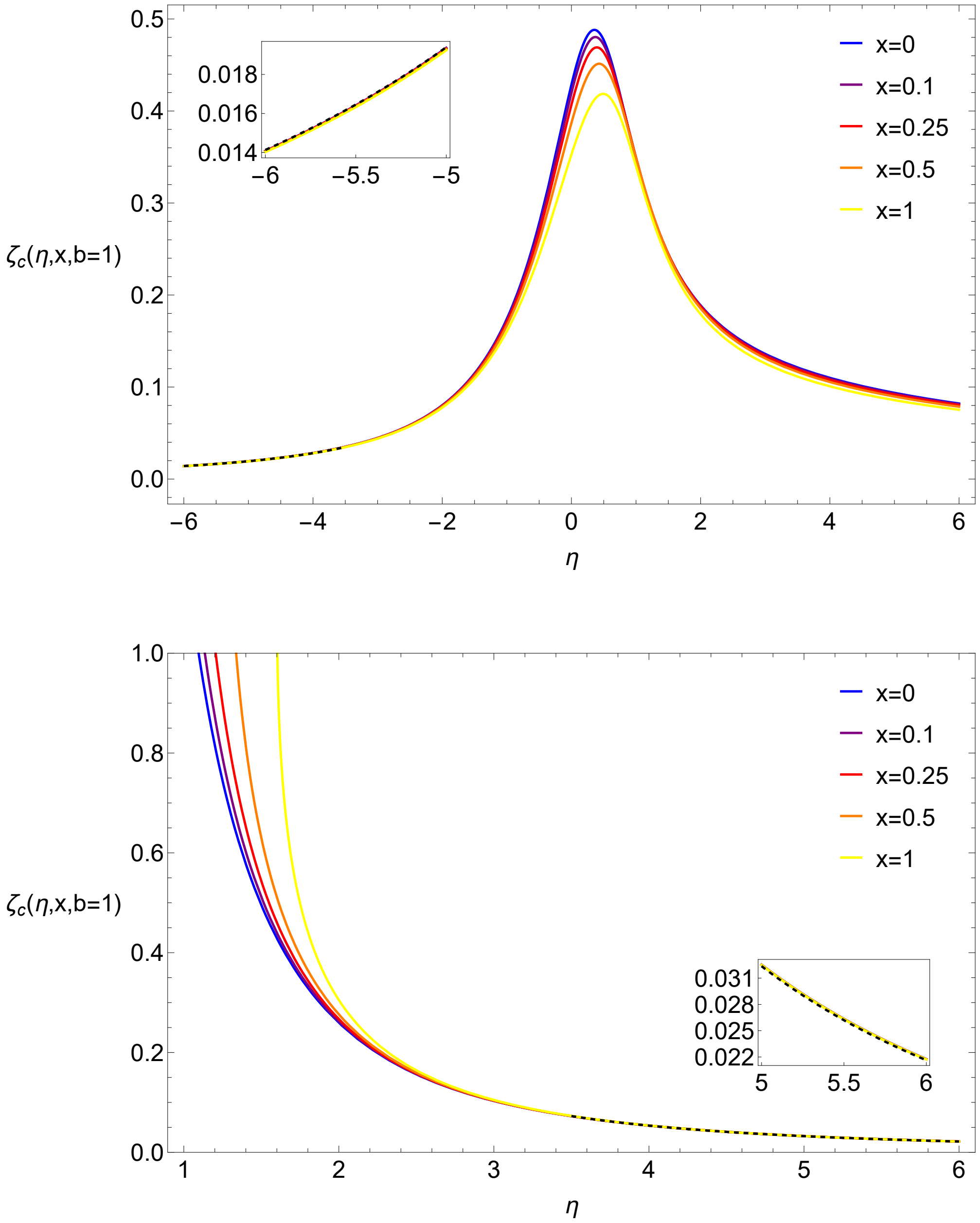

Figure 3.11: B-F stability curves for the critical boson-boson repulsion parameter $\zeta_c$ in the attractive (top) and repulsive (bottom) regimes, plotted as functions of the interaction boson-fermion parameter $\eta = 1/(a_{BF}k_F)$ for different values of the relative concentration of bosons $x$ and same masses $m_B = m_F$ ($b = 1$). The insets highlight weak coupling regions. The dashed curves show the weak coupling perturbative benchmark (3.50).

Fig. 3.12 shows the dependence of the critical parameter $\zeta_c$ on the mass ratio $b = m_B/m_F$ for a three-dimensional Bose-Fermi mixture in both the attractive and repulsive regimes. Here, the system is considered in the polaron limit $x = 0$ and each curve corresponds to a fixed value of $\eta$.

One observes a clear trend: for both interaction branches, $\zeta_c$ exhibits a broad and relatively flat minimum in the vicinity of $b \approx 1$, indicating that the mixture tends to be more stable when the masses of the two species are comparable. This feature highlights the role of mass balance in mitigating mechanical instability due to attractive or repulsive interspecies interactions.

At the same time, as the mass imbalance grows, either towards $b \ll 1$ or $b \gg 1$, the critical $\zeta_c$ increases, diverging in the extreme limits. This behaviour reflects the fact that a large disparity in masses enhances the tendency for either bosons or fermions to induce collapse or phase separation, requiring stronger boson-boson repulsion to maintain stability.

A similar trend is observed in the following two plots highlighted in Fig. 3.13, which analyse the same dependence of $\zeta_c$ on the mass ratio $b$, but for the case of equal concentrations of bosons and fermions ($x = 1$). The overall behaviour confirms that mixtures with comparable masses are more stable, while strong mass imbalance demands larger intra-boson repulsion to prevent collapse.

Finally, the last two plots in Fig 3.14 show the behaviour of the critical parameter $\zeta_c$ as a function of the concentration ratio $x$ for equal masses ($b = 1$), with different curves corresponding to various values of $\eta$. The plots extend from $x = 0$ to $x = 1$ and reveal that the curves remain nearly flat for $x < 1$, indicating that increasing the boson concentration has only a modest effect on the overall stability of the mixture within this range.

This systematic exploration completes a detailed map of the stability boundaries across interaction strengths, mass ratios, and concentration ratios, offering a clear reference for future studies on Bose-Fermi mixtures.

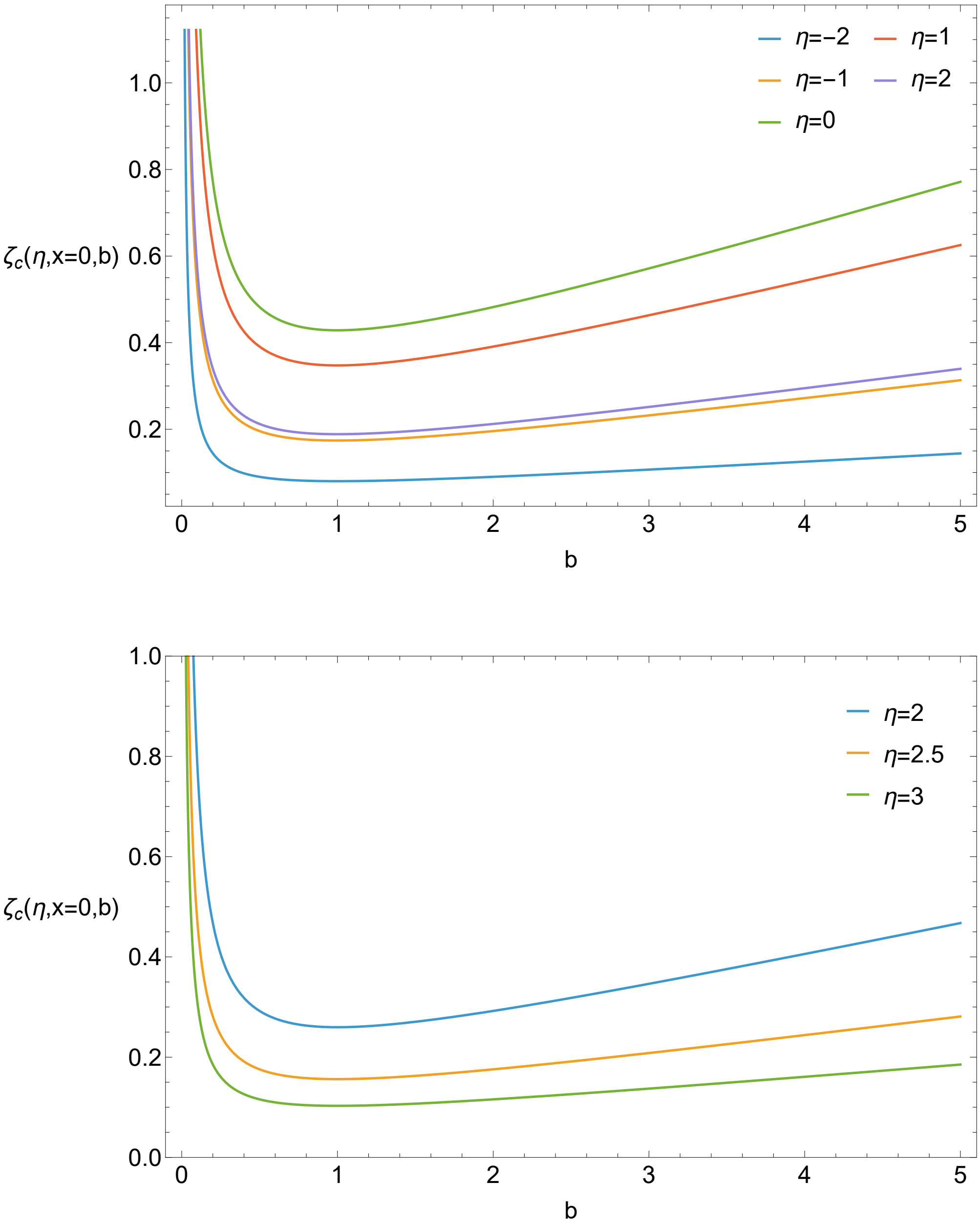

Figure 3.12: B-F stability curves for the critical boson-boson repulsion parameter $\zeta_c$ in the attractive (top) and repulsive (bottom) regimes, plotted as functions of the boson to fermion mass ratio $b = \frac{m_B}{m_F}$ for different values of the interaction parameter $\eta$ in the polaron limit $x = 0$.

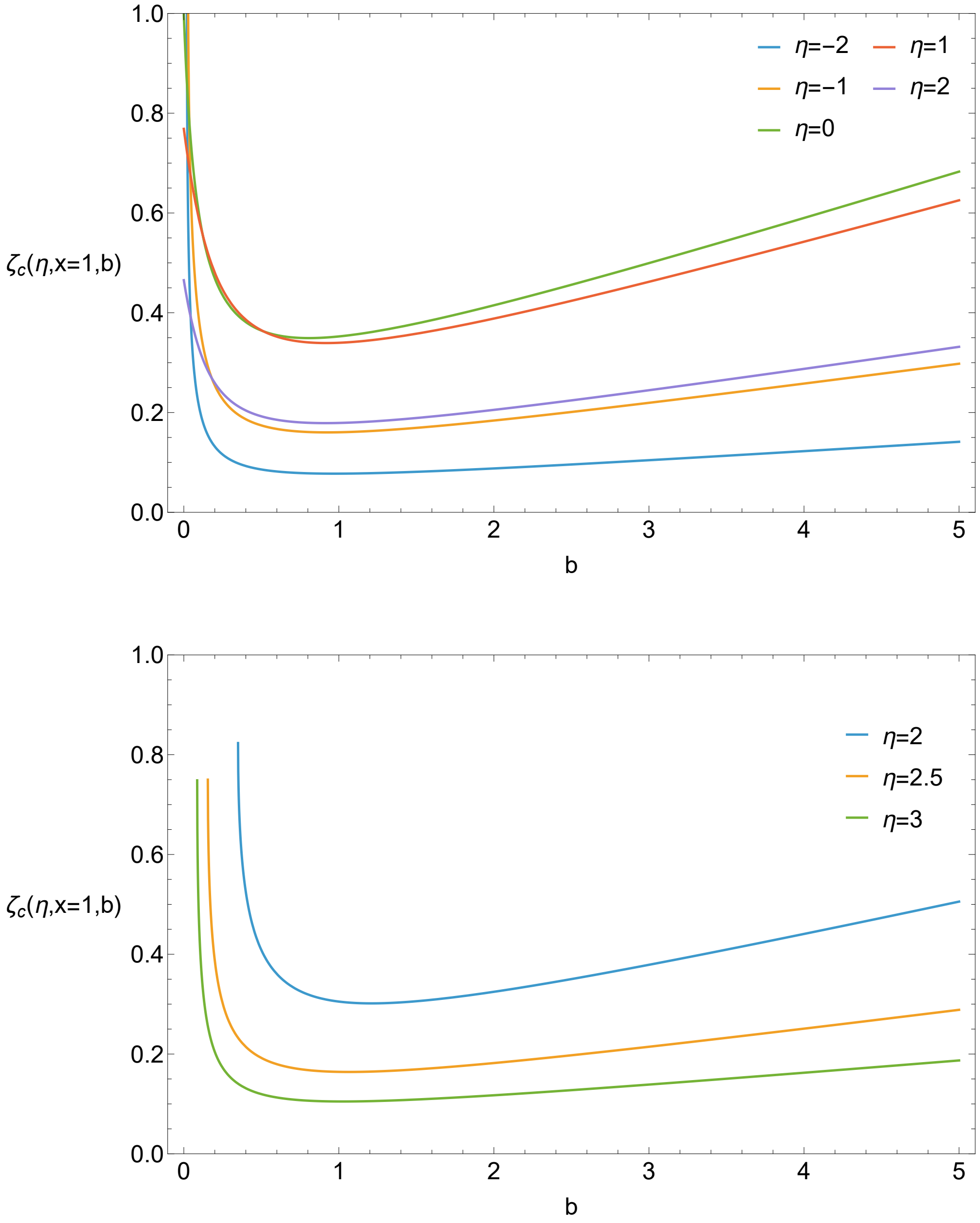

Figure 3.13: B-F stability curves for the critical boson-boson repulsion parameter $\zeta_c$ in the attractive (top) and repulsive (bottom) regimes, plotted as functions of the boson to fermion mass ratio $b = \frac{m_B}{m_F}$ for different values of the interaction parameter $\eta$ with an equal concentration of bosons and fermions ($x = 1$).

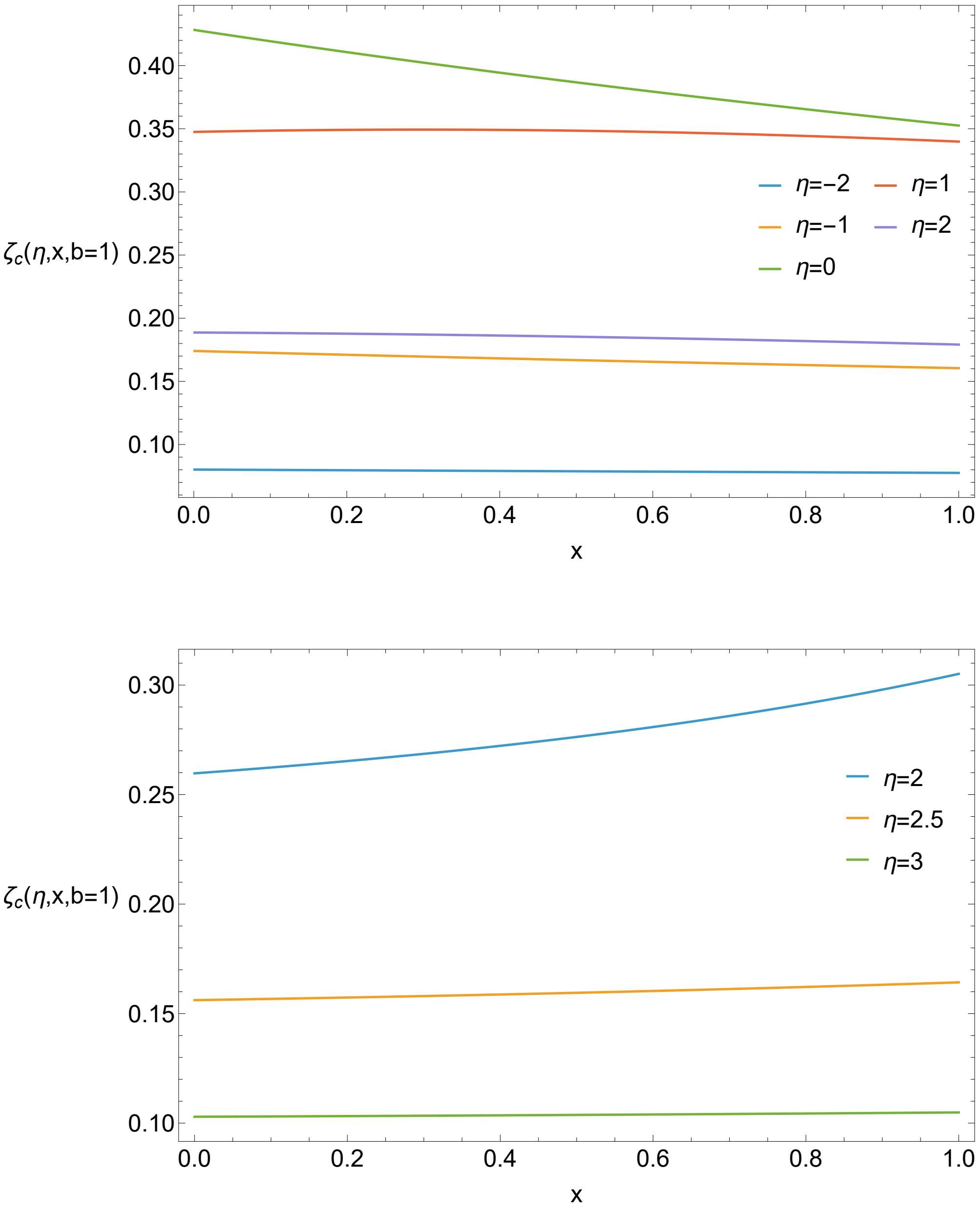

Figure 3.14: B-F stability curves for the critical boson-boson repulsion parameter $\zeta_c$ in the attractive (top) and repulsive (bottom) regimes, plotted as functions of the boson to fermion concentration ratio $x = \frac{n_B}{n_F}$ for different values of the interaction parameter $\eta$ with same masses $m_B = m_F$ $(b = 1)$.

## 3.4 2D LOCV equation

If we want to consider a Bose-Fermi mixture in 2 dimensions the real difference with respect to the 3D case starts from the LOCV equation. We start with the usual Jastrow-Slater variational wave-function

$$\Psi(\mathbf{r},\mathbf{R}) = \prod_{i,j} f(r_i - R_j)\Phi_{BG}(\mathbf{r})\Phi_{FG}(\mathbf{R}), \tag{3.51}$$

where now the free wave-function for the Bose and Fermi gas are of course normalized with an area instead of a volume

$$\Phi_{BG}(R_1, ..., R_{N_F}) = \left(\frac{1}{A}\right)^{\frac{N_B}{2}}. \tag{3.52}$$

$$\Phi_{FG}(R_1, ..., R_{N_F}) = \left(\frac{1}{A}\right)^{\frac{N_F}{2}} \| e^{ik_n \cdot R_m} \| = \langle \mathbf{R} | \Phi_{FG} \rangle \, . \tag{3.53}$$

By following the same steps, highlighted in (2.3,3.1) for calculating the expectation value of the hamiltonian $H_{BF}$, we end up with the same LOCV equation

$$\big[ - \frac{1}{2m_r}\nabla_r^2 + U_{BF}(r)\big] f(r) = \lambda f(r), \tag{3.54}$$

where, since $\nabla_r^2 = \frac{\partial^2}{\partial x^2} + \frac{\partial^2}{\partial y^2}$ is a 2-dimensional Laplacian, recalling (1.54) the substitution $u(r) = \sqrt{r} f(r)$ doesn't help much since we can't turn this equation into a simple 1D Schroedinger problem. Once the potential is set to be $U_{BF}(r) = U_0\delta(r)$, the solution for $f(r)$ for $r > 0$ will be in terms of Bessel functions as explained in (B.1.3).

### 3.4.1 Repulsive regime

We start with the repulsive regime ($\lambda > 0$) since is a bit easier to tackle than the attractive one (contrary to the $3D$ case), setting $\kappa = \sqrt{2m_r\lambda}$, we write the solution in terms of Bessel functions of the first and second kind of order zero

$$f(r) \propto c_1(\kappa)J_0(\kappa r) + c_2(\kappa)Y_0(\kappa r), \tag{3.55}$$

where $c_1$ and $c_2$ are factors to be determined.

By imposing now the 2D Bethe-Peierls boundary conditions [25]

$$\left[r\frac{d}{dr} - \frac{1}{\ln\left(\frac{r}{a_{BF}}\right)}\right]f(r) \xrightarrow{r \to 0} 0, \tag{3.56}$$

we find the proportionality between $c_1$ and $c_2$ giving

$$f(r) \propto J_0(\kappa r) - \frac{\pi}{2[\gamma + \ln\left(\frac{\kappa a_{BF}}{2}\right)]}Y_0(\kappa r), \tag{3.57}$$

where $a_{BF}$ is the 2D scattering length between bosons and fermions, which from now on we just call $a$ for simplicity, while $\gamma \simeq 0,577$ is the Euler-Mascheroni constant.

The LOCV boundary conditions $f(d) = 1$ and $f'(d) = 0$ must be imposed as well; starting from the first one we can get rid of the proportionality symbol and write

$$f(r) = \frac{J_0(\kappa r) - \frac{\pi}{2[\gamma+\ln\left(\frac{\kappa a}{2}\right)]}Y_0(\kappa r)}{J_0(\kappa d) - \frac{\pi}{2[\gamma+\ln\left(\frac{\kappa a}{2}\right)]}Y_0(\kappa d)}. \tag{3.58}$$

The second condition gives us the dependence of $\kappa$ on $d$ through the scattering length $a$ and involves Bessel's functions of order 1, it reads

$$J_1(\kappa d) = \frac{\pi}{2[\gamma + \ln\left(\frac{\kappa a}{2}\right)]}Y_1(\kappa d). \tag{3.59}$$

Last but not least, the $P(d) = n_F \int_{|r|<d} d^2r f(r)^2 \equiv 1$ constraint must be enforced. The solution of the integral of $f(r)^2$ in 2 dimensions is very complicated and it involves the Meijer G-function (B.2). With our $f(r)$ the integral can be written as

$$\begin{aligned}\int_{|\vec{r}|<d} d^2r f(r)^2 = 2\pi\Bigg\{ & 2d^2\left[J_0(\kappa d)^2 + J_1(\kappa d)^2\right]\left[(\gamma - \ln 2)^2 + \frac{\pi^2}{4} + \left(2\gamma + \ln\left(\frac{\kappa a}{4}\right)\right)\ln(\kappa a)\right] + \\ & + \frac{2\sqrt{\pi}}{\kappa^2}\left[\gamma + \ln\left(\frac{\kappa a}{2}\right)\right] G^{2,0}_{1,1}\left(\begin{matrix} \frac{3}{2} \\ 1, 1, 0 \end{matrix}\,\middle|\, (\kappa d)^2\right) + \\ & + \frac{\pi^{\frac{3}{2}}}{\kappa^2} G^{3,1}_{2,1}\left(\begin{matrix} 1, \frac{3}{2}, \frac{3}{2} \\ 1, 1, 1, \frac{3}{2} \end{matrix}\,\middle|\, (\kappa d)^2\right)\Bigg\} \Big/ \left[J_0(\kappa d) - \frac{\pi}{2[\gamma + \ln\left(\frac{\kappa a}{2}\right)]}Y_0(\kappa d)\right]^2,\end{aligned} \tag{3.60}$$

for $\kappa$ and $d$ strictly larger than 0; this result was obtained through the software Wolfram Mathematica 14.2 [33].

As we have done in 3D we introduce dimensionless quantities in order to obtain numerical results; in 2D the density of a spinless fermion gas reads $n_F = \frac{k_F^2}{4\pi}$ so by setting the dimensionless parameters $\eta = -\ln(k_F a)$ [12], $\bar{\kappa} = \frac{\kappa}{k_F}$, $\bar{d} = dk_F$ we get the following pair of equations to be solved simultaneously

$$J_1(\bar{\kappa}\bar{d}) = \frac{\pi}{2[\gamma - \eta + ln(\frac{\bar{\kappa}}{2})]} Y_1(\bar{\kappa}\bar{d}), \tag{3.61}$$

$$\begin{aligned} &\bar{d}^2\big[J_0(\bar{\kappa}\bar{d})^2 + J_1(\bar{\kappa}\bar{d})^2\big]\left[(\gamma - \ln 2)^2 + \frac{\pi^2}{4} + \left(2\gamma - \eta + \ln\left(\frac{\bar{\kappa}}{4}\right)\right)(\ln\bar{\kappa} - \eta)\right] + \\ &+ \frac{\sqrt{\pi}}{\bar{\kappa}^2}\left[\gamma - \eta + \ln\left(\frac{\bar{\kappa}}{2}\right)\right] G_{1,1}^{2,0}\left(\begin{matrix} \frac{3}{2} \\ 1, 1, 0 \end{matrix} \,\middle|\, (\bar{\kappa}\bar{d})^2\right) + \frac{\pi^{\frac{3}{2}}}{2\bar{\kappa}^2} G_{2,1}^{3,1}\left(\begin{matrix} 1, \frac{3}{2}, \frac{3}{2} \\ 1, 1, 1, \frac{3}{2} \end{matrix} \,\middle|\, (\bar{\kappa}\bar{d})^2\right) = \\ &= \left[J_0(\bar{\kappa}\bar{d}) - \frac{\pi}{2[\gamma - \eta + \ln(\frac{\bar{\kappa}}{2})]} Y_0(\bar{\kappa}\bar{d})\right]^2. \end{aligned} \tag{3.62}$$

as $\eta$ varies from weak to strong coupling, obtaining $\bar{\kappa}(\eta)$, $\bar{d}(\eta)$ as functions of the single variable $\eta$.

Once the numerical solutions for $\bar{d}(\eta)$ and $\bar{\kappa}(\eta)$ are obtained, they can be inserted into (3.58) to generate, the explicit correlation functions $f_\eta(r)$ for each value of $\eta$. These functions are shown in Fig. 3.15.

In two dimensions, the short-range behaviour of the correlation functions is logarithmic, leading to $f(r) \sim \log(r)$ as $r \to 0$. Consequently, the product $rf(r)$ vanishes in the limit $r \to 0$. This behaviour is consistently observed in the rescaled curves in Fig. 3.16, all of which tend to zero as $r/d \to 0$.

For completeness a plot of the pair correlation function $g(r) = f(r)^2$ is shown in Fig. 3.17. The plot is not compared to any other data since, to the best of our knowledge, no literature data currently exist for a $2D$ repulsive pair correlation function associated with the excited state (repulsive) of an attractive potential.

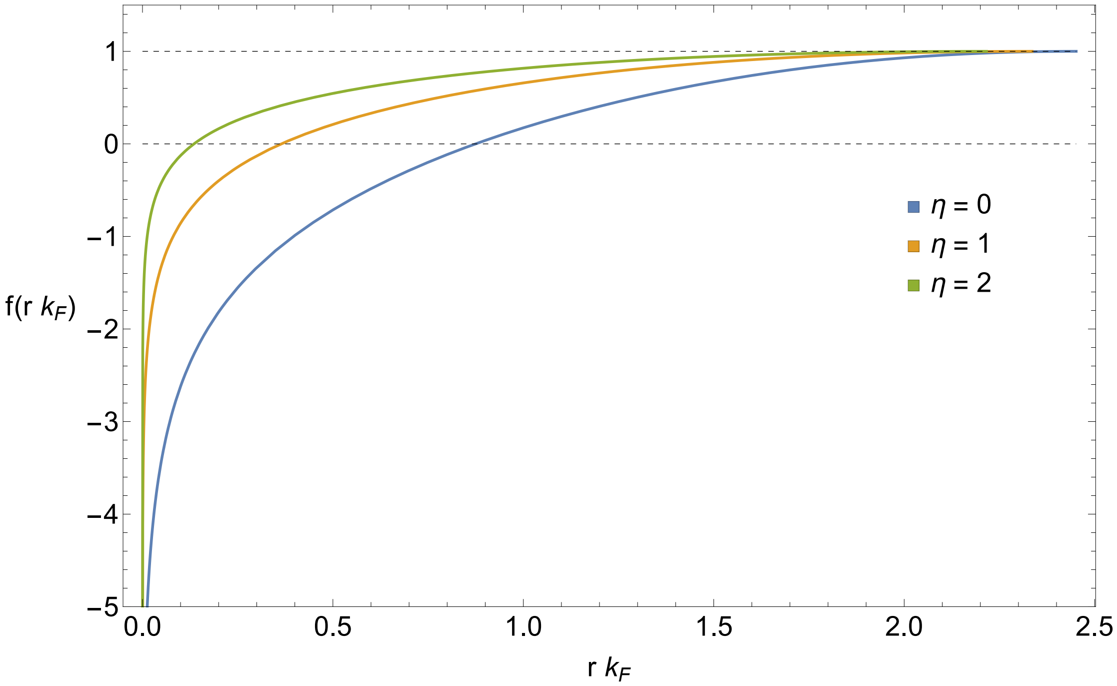

Figure 3.15: Correlation function $f(r)$ for the repulsive regime in two dimensions, shown for three representative interaction strengths: from $\eta = 0$ (strong repulsion) to $\eta = 2$ (weak repulsion). The plots illustrate how increasing repulsion enhances short-range exclusion shifting the position of the node to the right.

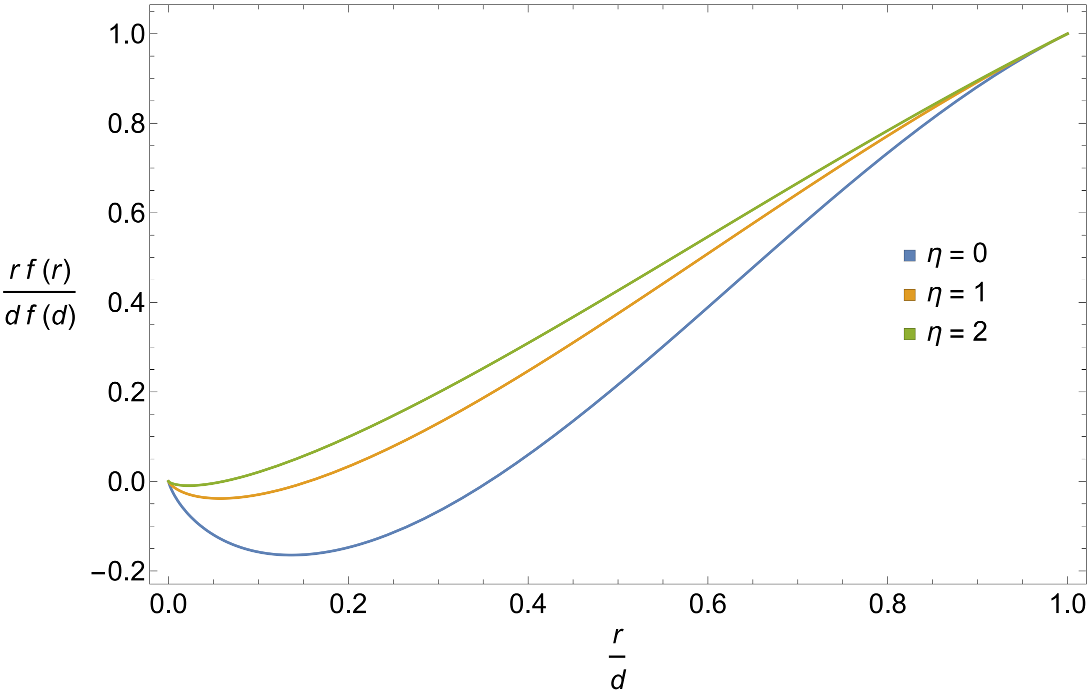

Figure 3.16: Rescaled correlation function $\frac{r}{d}\frac{f(r)}{f(d)}$ plotted as a function of the normalized distance $r/d$ for the repulsive regime in two dimensions. The curves are shown for three representative values of $\eta$ ranging from 0 to 2. All curves are normalized to end at the common point $(1, 1)$.

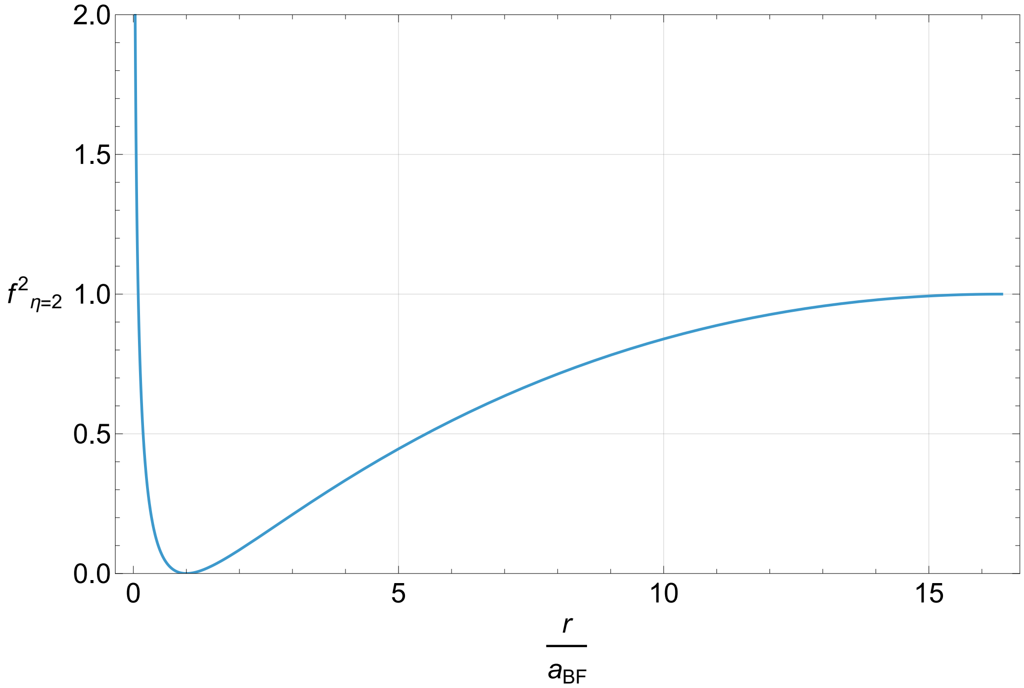

Figure 3.17: Pair correlation function $g(r) = f(r)^2$ in the repulsive 2D case, evaluated at $\eta = 2$. The horizontal axis is expressed in units of the two dimensional scattering length $a_{BF}$ associated with $\eta = 2$.

### 3.4.2 Attractive regime

From the repulsive solution it is straightforward to get the attractive solution ($\lambda < 0$) by performing the change of variables $\kappa \to ik$, by doing so we get

$$f(r) \propto J_0(ikr) - \frac{\pi}{2[\gamma + \ln\left(\frac{ika}{2}\right)]} Y_0(ikr). \tag{3.63}$$

It is convenient to switch to the modified Bessel functions $I_0$ and $K_0$ with real argument $kr$; using (B.9) and (B.10) one finds

$$f(r) \propto \left(1 - \frac{i\pi}{2\gamma + 2\ln\left(\frac{iak}{2}\right)}\right) I_0(kr) + \frac{1}{\gamma + \ln\left(\frac{iak}{2}\right)} K_0(kr). \tag{3.64}$$

such that the wave-function reads

$$f(r) = \frac{\left(1 - \frac{i\pi}{2\gamma+2\ln\left(\frac{iak}{2}\right)}\right) I_0(kr) + \frac{1}{\gamma+\ln\left(\frac{iak}{2}\right)} K_0(kr)}{\left(1 - \frac{i\pi}{2\gamma+2\ln\left(\frac{iak}{2}\right)}\right) I_0(kd) + \frac{1}{\gamma+\ln\left(\frac{iak}{2}\right)} K_0(kd)}, \tag{3.65}$$

once $f(d) = 1$ is enforced.

By imposing also $f'(d) = 0$ and $P(d) = 1$, after switching to dimensionless parameters one gets

$$I_1(\bar{k}\bar{d}) = \frac{1}{\left[\gamma - \eta + \ln\left(\frac{\bar{k}}{2}\right)\right]} K_1(\bar{k}\bar{d}) \tag{3.66}$$

$$\begin{aligned}
&\frac{1}{2}\bar{d}^2\left[I_0(\bar{k}\bar{d})^2 - I_1(\bar{k}\bar{d})^2\right]\left[\gamma - \eta + \ln\left(\frac{\bar{k}}{2}\right)\right]^2 + \\
&+ \frac{\sqrt{\pi}}{4\bar{k}^2} G^{3,1}_{1,1}\left(\begin{matrix} 1, \frac{3}{2} \\ 1, 1, 1, 0 \end{matrix} \middle| (\bar{k}\bar{d})^2\right) + \frac{1}{2\sqrt{\pi}\bar{k}^2}\left[\gamma - \eta + \ln\left(\frac{\bar{k}}{2}\right)\right] G^{2,1}_{0,1}\left(\begin{matrix} \frac{3}{2} \\ 1, 1, 0 \end{matrix} \middle| (\bar{k}\bar{d})^2\right) = \\
&= 2\left[K_0(\bar{k}\bar{d}) + \left[\gamma - \eta + \ln\left(\frac{\bar{k}}{2}\right)\right] I_0(\bar{k}\bar{d})\right]^2,
\end{aligned} \tag{3.67}$$

which are solved simultaneously as $\eta$ varies from weak to strong coupling, obtaining $\bar{k}(\eta)$, $\bar{d}(\eta)$ as functions of the single variable $\eta$. Equation (3.67) was obtained through the software Wolfram Mathematica 14.2 [33].

Once the numerical solutions for $\bar{d}(\eta)$ and $\bar{k}(\eta)$ are obtained, they can be inserted into (3.65) to generate, the explicit correlation functions $f_\eta(r)$ for each value of $\eta$. These functions are shown in Fig. 3.18.

In two dimensions, the short-range behaviour of the correlation functions is logarithmic, leading to $f(r) \sim \log(r)$ as $r \to 0$. Thus, the product $rf(r)$ approaches zero as $r \to 0$. As in the repulsive case this behaviour is consistently observed in the rescaled curves shown in Fig. 3.19, all of which tend to zero when $r/d \to 0$.

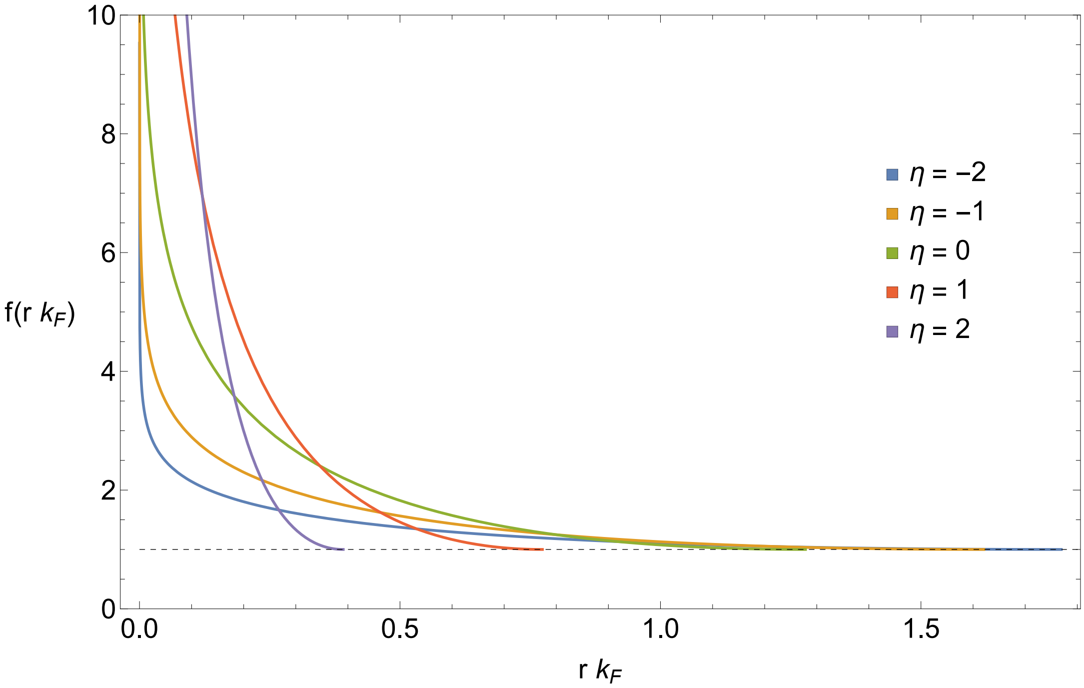

Figure 3.18: Correlation function $f(r)$ for the attractive regime in two dimensions, shown for five representative interaction strengths: from $\eta = -2$ (weak attraction) to $\eta = 2$ (strong attraction). As in $3D$ the healing length becomes progressively shorter as the attraction increases.

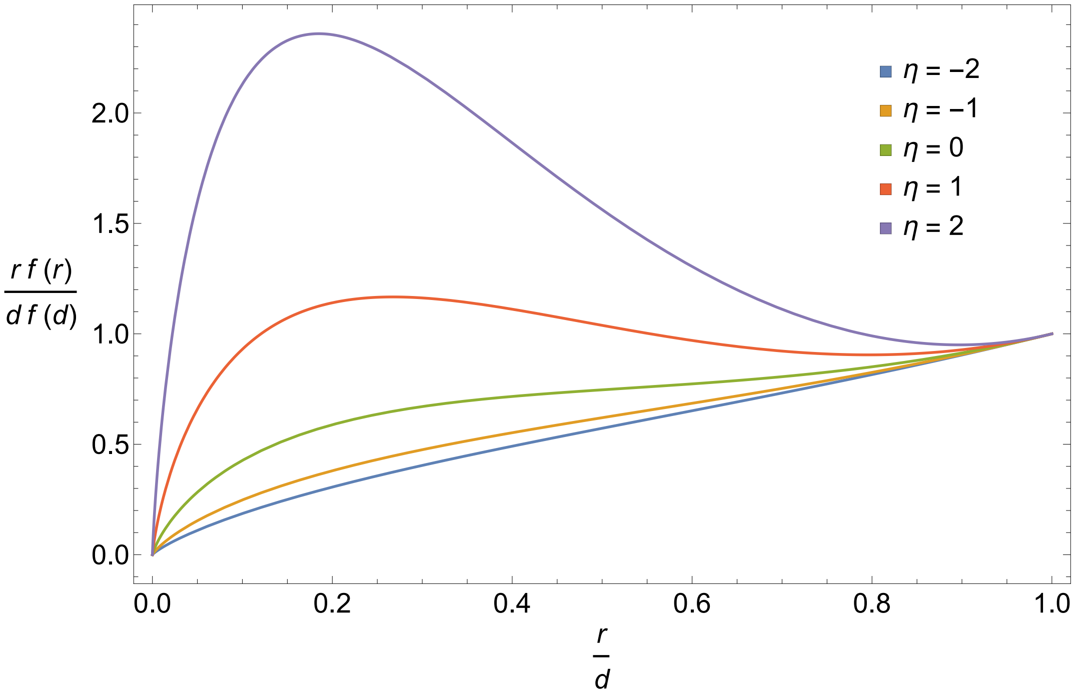

Figure 3.19: Rescaled correlation function $\frac{r}{d}\frac{f(r)}{f(d)}$ plotted as a function of the normalized distance $r/d$ for the attractive regime in two dimensions. The curves correspond to five representative values of $\eta$ from $-2$ to 2. All curves are normalized to end at the common point $(1, 1)$.

## 3.5 2D Energy Branches

We now analyse the energy spectrum of a Bose-Fermi mixture in two dimensions across interaction regimes.

Analogously to the 3D case, the energy density of the system is given by

$$\begin{aligned}\frac{\langle H_{BF}\rangle}{V} &= \mathcal{E}_F^0 + n_B n_F \int d^2x\, f(x)\left(-\frac{1}{2m_r}\nabla_x^2 + U_{BF}(x)\right) f(x) \\ &= \mathcal{E}_F^0 + n_B n_F \lambda \int d^2x\, f^2(x) = \mathcal{E}_F^0 + n_B\lambda,\end{aligned} \tag{3.68}$$

where, again, $\lambda$ is the pair interaction energy obtained from the two-body Schrödinger equation under the LOCV constraint.

In the attractive regime, the solution corresponds to a bound (non molecular) state with energy

$$\lambda^- = -\frac{k^2}{2m_r} = \frac{1+b}{2b} A^-(\eta)\,\epsilon_F, \qquad A^-(\eta) = -2\bar{k}^2, \tag{3.69}$$

while in the repulsive regime, the positive-energy scattering state gives

$$\lambda^+ = \frac{\kappa^2}{2m_r} = \frac{1+b}{2b} A^+(\eta)\,\epsilon_F, \qquad A^+(\eta) = 2\bar{\kappa}^2. \tag{3.70}$$

In 2D, the interaction parameter has the form $\eta = -\ln(a_{BF}k_F)$ [12]. The two lowest branches $A^-(\eta)$ and $A^+(\eta)$ correspond to solutions of the LOCV equation with zero and one node, respectively. Higher branches are possible but are not shown. The numerical results for $A^\pm(\eta)$ obtained from the 2D LOCV equation are plotted in Fig. 3.20. Recalling (2.12), the weak coupling benchmarks [30] are given by

$$A^+(\eta) \to \frac{1}{\tilde{\eta}}\left(1 + \frac{1-2\ln 2}{2\tilde{\eta}}\right) \quad \text{for} \quad \eta \gg 1, \tag{3.71}$$

$$A^-(\eta) \to \frac{1}{\tilde{\eta}}\left(1 + \frac{1-2\ln 2}{2\tilde{\eta}}\right) \quad \text{for} \quad \eta \ll 1, \tag{3.72}$$

and the curves show good agreement, with just a slight discrepancy. In particular, in the strong coupling limit the $A^-(\eta)$ curve closely follows the binding energy

$$A^-(\eta) \to E_B/E_F = -8e^{2\eta - 2\gamma_E} \quad \text{for} \quad \eta \gg 1, \tag{3.73}$$

where $\gamma_E$ denotes the Euler-Mascheroni constant.

The validity of the LOCV predictions in two dimensions can be further tested by comparison with both theoretical and experimental results available in the literature.

In Fig. 3.21, we compare the repulsive branch $A^+(\eta)$ with quantum Monte Carlo results obtained using a hard-disk interaction potential [34]. The agreement is excellent in the weakly interacting regime ($\eta \gtrsim 2$), where the LOCV framework is expected to be reliable. As the interaction strength increases, a very small but noticeable deviation appears, reflecting the limitations of the two-body Jastrow ansatz in the strong-coupling regime.

In Fig. 3.22, we show a second comparison, this time for the attractive branch $A^-(\eta)$, against experimental measurements of the polaron binding energy in a two-dimensional Fermi-Fermi mixture reported in Ref. [35]. Although the experiment involves a fermionic impurity, the comparison remains valid within the LOCV framework in the polaron limit, since it treats single-impurity correlations identically regardless of the associated statistics. The LOCV prediction accurately captures the measured polaron binding energy, just a small deviation is noticeable at intermediate coupling.

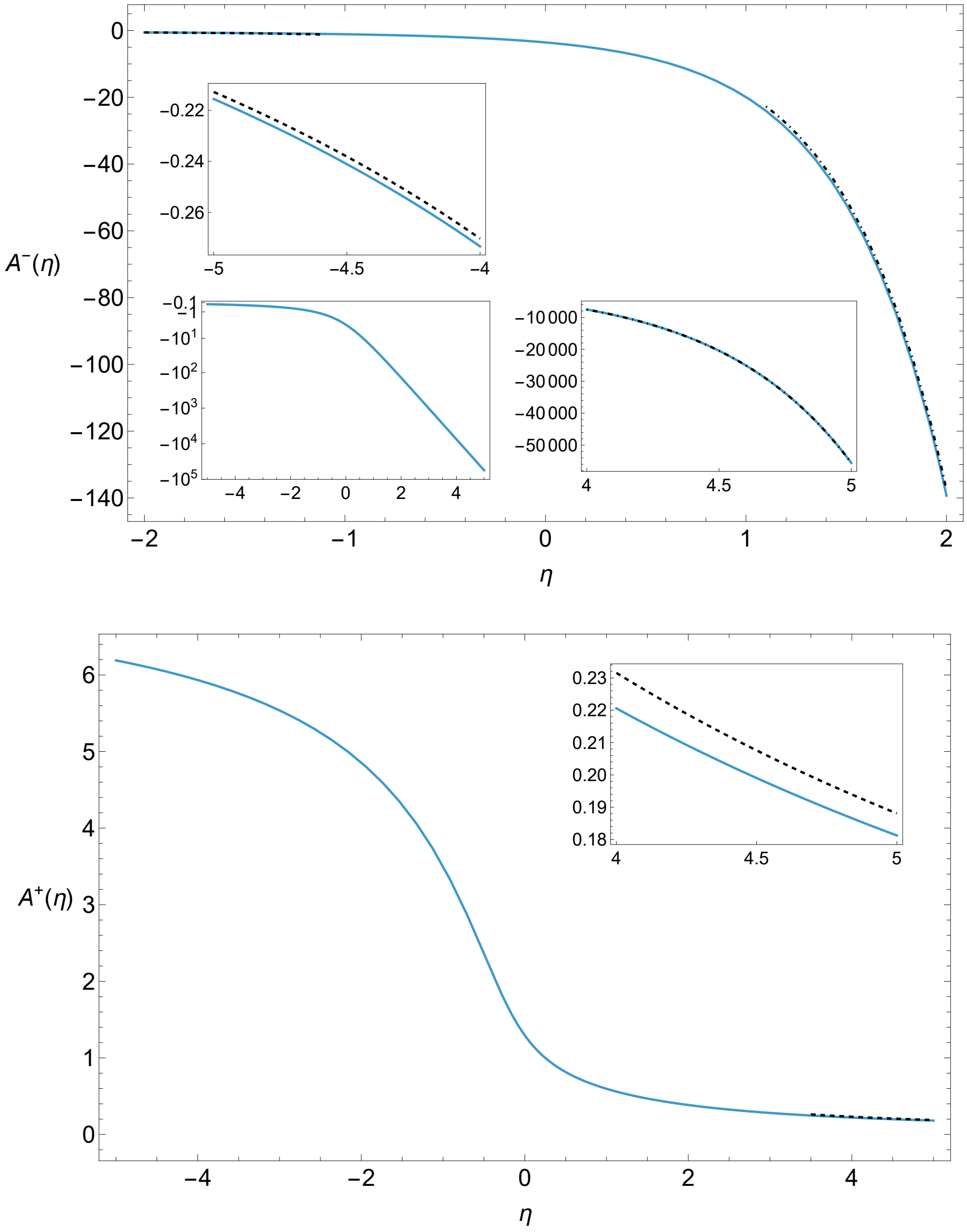

Figure 3.20: Dimensionless interaction energy per Bose-Fermi pair in the attractive ($A^-(\eta)$, top) and repulsive ($A^+(\eta)$, bottom) regimes in two dimensions, plotted as functions of the interaction parameter $\eta = -\ln(a_{BF}k_F)$. The various insets highlight weak and strong coupling regions and the interaction energy ($A^-(\eta)$, top) in logarithmic scale. The dashed curves show the weak coupling perturbative benchmarks (3.71,3.72). The dot-dashed curve shows the binding energy benchmark at strong coupling (3.73).

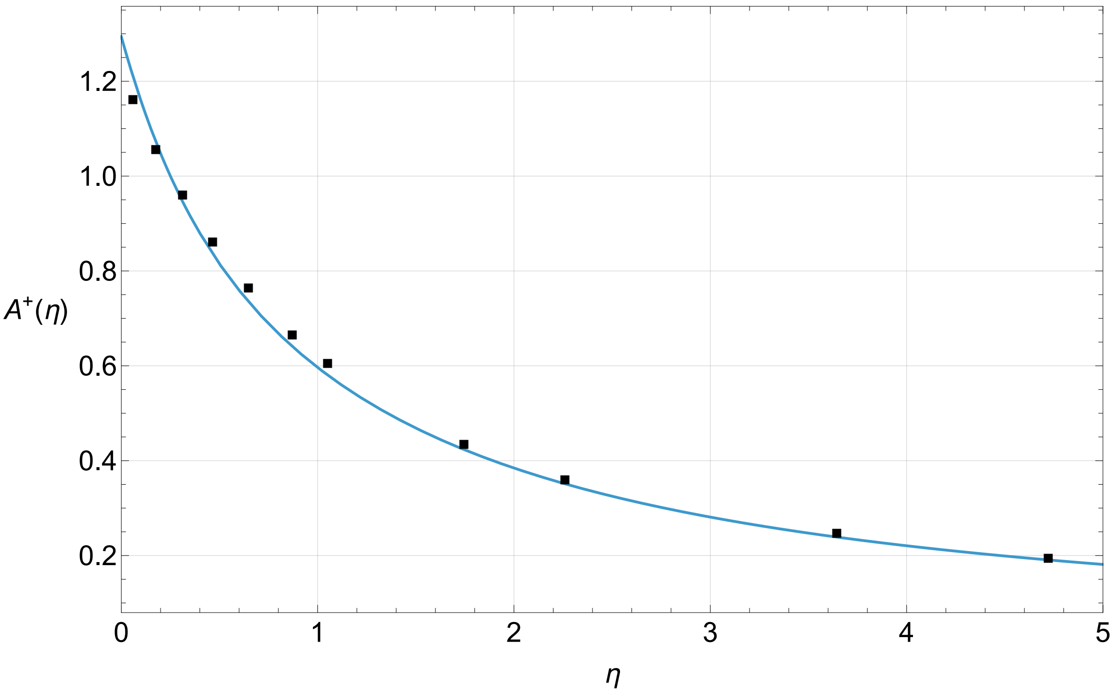

Figure 3.21: Comparison of the repulsive energy branch in the 2D case with quantum Monte Carlo data points associated to a hard-disk potential from [34]. The quantum Monte Carlo data is shifted here by the transformation from $\tilde{\eta}$ to $\eta$ 2.12. The LOCV curve shows good agreement.

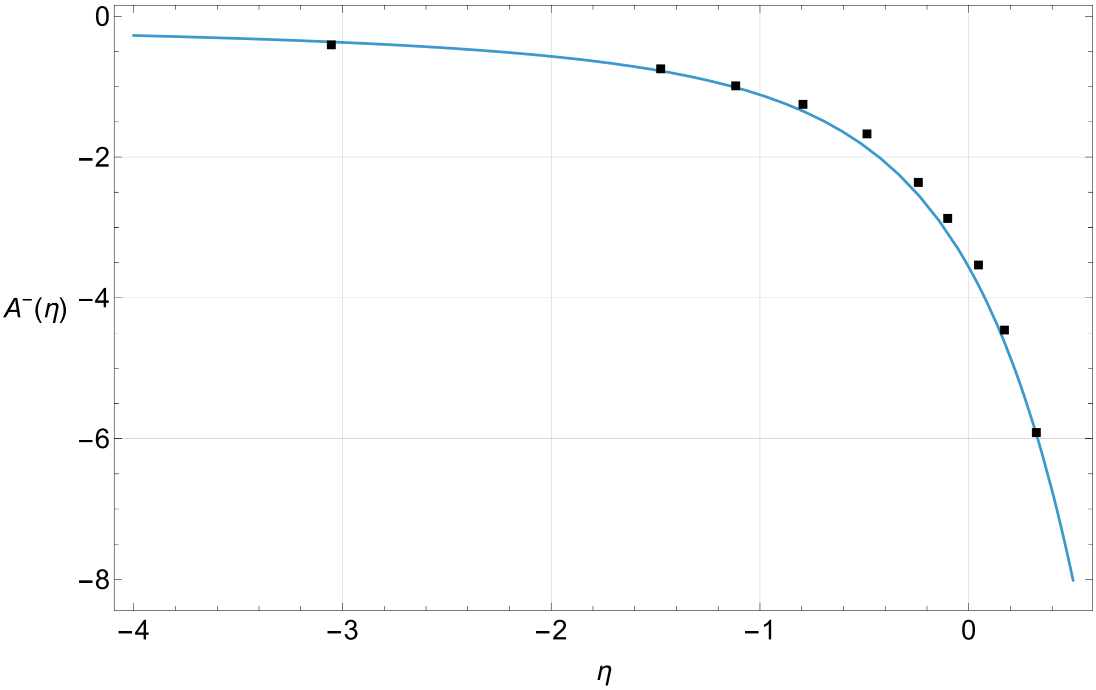

Figure 3.22: Comparison of the polaron binding energy in the 2D case with experimental data points from [35]. The experimental data is shifted here by the transformation from $\tilde{\eta}$ to $\eta$ 2.12. The theoretical curve shows good agreement.

## 3.6 2D Mixture stability

As in the 3D case, also in 2D, a mixture in which the only existing interaction is the one among bosons and fermions is not mechanically stable. One must thus enforce a repulsion between the bosons and as in 3D we will use a delta-like contact interaction

$$H_{BB} = \frac{1}{2}\sum_{\sigma\neq\sigma'} U_{BB}(r_\sigma - r_{\sigma'}) \xrightarrow{\textit{dilute limit}} \frac{1}{2} g_{BB} \sum_{\sigma\neq\sigma'} \delta^{(2)}(r_\sigma - r_{\sigma'}). \tag{3.74}$$

### 3.6.1 Boson-Boson Interaction Energy and Depletion Effects

Performing the same steps highlighted in the 3D calculation, see Section (3.3.1), we find that the same formula for the expectation value of $H_{BB}$ on $\Psi$ holds also in 2D

$$\frac{1}{V}\frac{\langle\Psi|\, H_{BB}\,|\Psi\rangle}{\langle\Psi|\Psi\rangle} = \frac{1}{2} g_{BB} n_B^2 \big[1 + 4 n_F \int d^2 r\; l(r)^2\big], \tag{3.75}$$

expressible in terms of the depletion $D(\eta) = \frac{n_{dep}}{n_B} = n_F \int d^2r\; l(r)^2$.

In the attractive case we substitute (3.65) into the formula and find

$$D(\eta)^- = 1 - \frac{1 - (\gamma - \eta + \ln\frac{\bar{k}}{2})[\frac{(\overline{dk})^2}{4} I_0(\overline{dk}) - \overline{dk} I_1(\overline{dk})] - \frac{(\overline{dk})^2}{4} K_0(\overline{dk}) - \overline{dk} K_1(\overline{dk})}{\bar{k}^2[K_0(\overline{dk}) + (\gamma - \eta + \ln\frac{\bar{k}}{2}) I_0(\overline{dk})]}. \tag{3.76}$$

In the repulsive case instead, substituting (3.58), the fraction of depleted bosons reads

$$D(\eta)^+ = 1 + \frac{\bar{d}^2}{4} - \frac{\frac{\bar{d}}{\bar{\kappa}} J_1(\bar{d}\bar{\kappa})(\eta - \gamma - \ln\frac{\bar{\kappa}}{2}) + \frac{2\pi}{\bar{\kappa}^2} G^{1,2}_{2,1}\left(\begin{matrix} 1, \frac{1}{2} \\ 1, 1, 0, \frac{1}{2} \end{matrix} \,\middle|\, (\frac{\bar{\kappa}\bar{d}}{2})^2\right)}{\pi Y_0(\bar{\kappa}\bar{d}) + [\eta - \gamma - \ln\big(\frac{\bar{\kappa}}{2}\big)] J_0(\bar{\kappa}\bar{d})}. \tag{3.77}$$

The corresponding plots are shown in Fig. 3.23. The functions $D^+(\eta)$ and $D^-(\eta)$ describe the boson depletion across all coupling regimes. In the weak coupling regime, the benchmark [30] is given by

$$D^+(\eta) \to \frac{\ln 2}{\tilde{\eta}^2} \quad \text{for} \quad \eta \gg 1, \tag{3.78}$$

$$D^-(\eta) \to \frac{\ln 2}{\tilde{\eta}^2} \quad \text{for} \quad \eta \ll 1, \tag{3.79}$$

Defined in terms of $\tilde{\eta}$ (2.12). A noticeable discrepancy is immediately apparent Fig. 3.23, as the LOCV method underestimates the fraction of depleted bosons.

This difference is likely due to the formula used for calculating the condensate fraction (3.30), which proves to be even less reliable in 2D than in 3D.

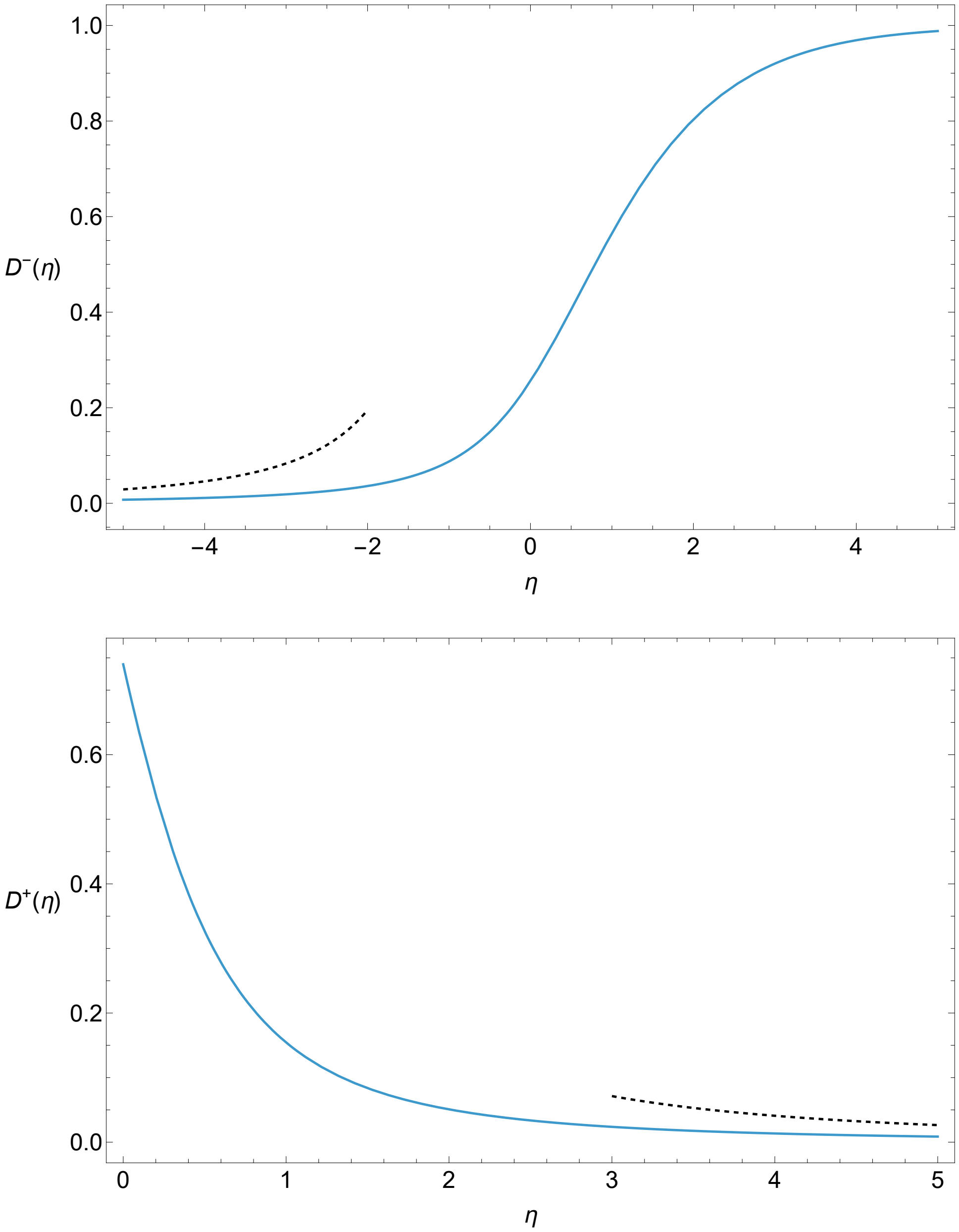

Figure 3.23: Relative quantum depletion of bosons in the attractive ($D^-(\eta)$, top) and repulsive ($D^+(\eta)$, bottom) regimes, plotted as functions of the interaction parameter $\eta = -\ln(a_{BF}k_F)$. The dashed curves show the weak coupling perturbative benchmarks (3.78,3.79).

### 3.6.2 Chemical Potentials and Mechanical Stability

With the perturbative correction coming from the bosons-boson interaction we can write the total energy of the 2D B-F mixture as

$$\frac{E}{V} = \frac{1}{2}\epsilon_F n_F + \frac{1+b}{2b}A(\eta)\epsilon_F n_B + \frac{1}{2}g_{BB}n_B^2\big[1+4D(\eta)\big], \tag{3.80}$$

and we will proceed to calculate the chemical potentials of the bosons and the fermions as in the $3D$ case. In that case we chose the pair of dimensionless parameters ($\eta_{3D} = k_F a_{BF}, \zeta = k_F a_{BB}$) in order to analyse the stability of the system; in 2D however the first parameter gets reframed into $\eta_{2D} = -\ln(k_F a_{BF})$ and for the second one we choose $\chi \equiv -\frac{1}{\ln n_B a_{BB}^2}$ related to $g_{BB} = -\frac{4\pi}{m_B}\frac{1}{\ln n_B a_{BB}^2}$ such that $g_{BB} = \frac{4\pi}{m_B}\chi$, as standard practice in $2D$ Bose gases [36]. One should restrict the results up to the coupling regime $n_B a_{BB}^2 < 0.04$ ($\chi < 0.31$) between the bosons to avoid clustering, as highlighted in [15] for a zero-range pseudo-potential.

By defining as usual $x = \frac{n_B}{n_F}$ and differentiating the energy density with respect to $n_F$ and $n_B$, we obtain the chemical potentials:

$$\mu_F = \frac{\partial}{\partial n_F}\left(\frac{E}{V}\right) = \epsilon_F\left\{1 + \frac{1+b}{2b}\big[A(\eta) - \frac{1}{2}A'(\eta)\big]x - \frac{2}{b}\chi D'(\eta)x^2\right\}, \tag{3.81}$$

$$\mu_B = \frac{\partial}{\partial n_B}\left(\frac{E}{V}\right) = \epsilon_F\left\{\frac{1+b}{2b}A(\eta) + \frac{1}{b}(2\chi + \chi^2)\big[1+4D(\eta)\big]x\right\}. \tag{3.82}$$

These expressions reflect how the chemical potentials depend on the interaction strength $\eta$, the mass ratio $b = \frac{m_B}{m_F}$, the relative concentrations $x$, and the boson-boson scattering length via $\chi$. The chemical potentials are shown in Fig. 3.24 and Fig. 3.25 for fixed $b = 1$, $x = 1$ and $\chi = 0.1$. In this regime, recalling (2.12), their perturbative benchmarks for the weak coupling [30] read

$$\frac{\mu_F}{\epsilon_F} \to 1 + \frac{1}{\tilde{\eta}}\left(1 + \frac{1}{\tilde{\eta}}\ln\frac{e}{2}\right), \tag{3.83}$$

$$\frac{\mu_B}{\epsilon_F} \to 2(0.1) + \frac{1}{\tilde{\eta}}\left(1 + \frac{1}{\tilde{\eta}}\ln\frac{\sqrt{e}}{2}\right), \tag{3.84}$$

the LOCV curves show good agreement.

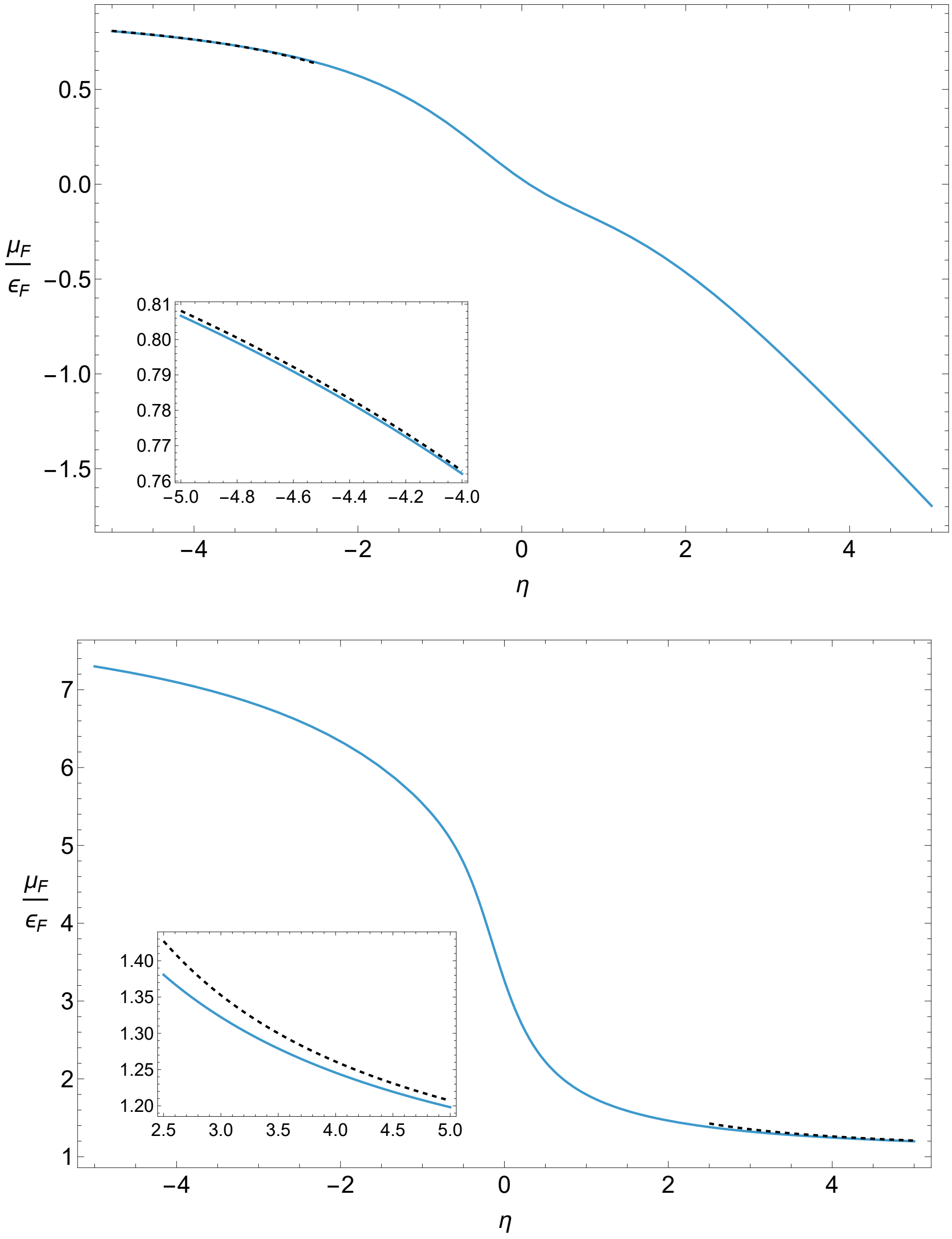

Figure 3.24: Fermionic chemical potential in two dimensions in the attractive (top) and repulsive (bottom) regimes, shown as functions of the interaction parameter $\eta$, with $b = 1$, $x = 1$ and $\chi = 0.1$. The insets highlight weak coupling regions. The dashed curves show the weak coupling perturbative benchmark (3.83).

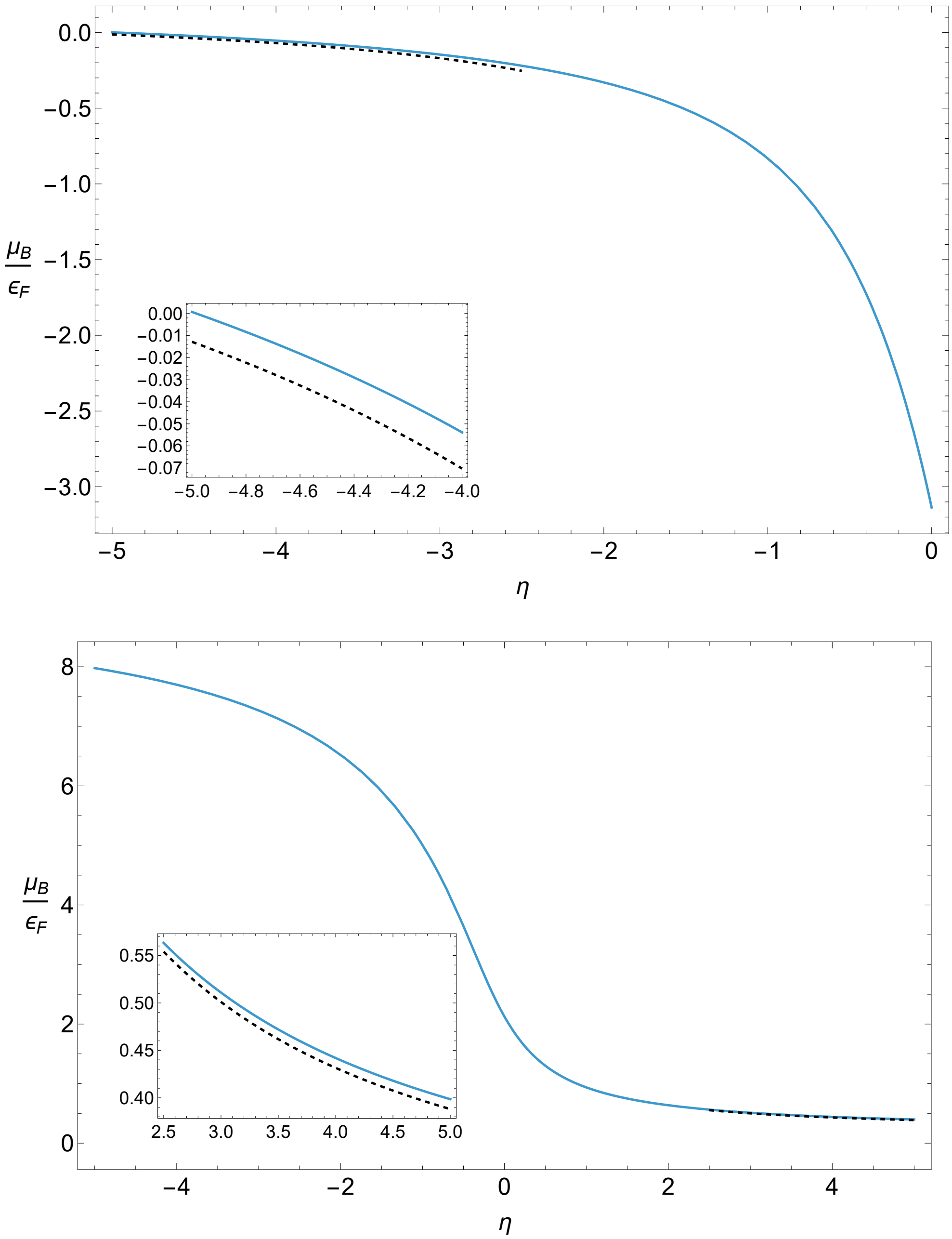

Figure 3.25: Bosonic chemical potential in two dimensions in the attractive (top) and repulsive (bottom) regimes, shown as functions of the interaction parameter $\eta$, with $b = 1$, $x = 1$ and $\chi = 0.1$. The insets highlight weak coupling regions. The dashed curves show the weak coupling perturbative benchmark (3.84).

We will now use the derivatives of the chemical potentials to calculate the stability matrix

$$M = \begin{pmatrix} \frac{\partial \mu_F}{\partial n_F} & \frac{\partial \mu_F}{\partial n_B} \\ \frac{\partial \mu_B}{\partial n_F} & \frac{\partial \mu_B}{\partial n_B} \end{pmatrix}. \tag{3.85}$$

The stability of the system requires $\frac{\partial \mu_F}{\partial n_F} > 0$, $\frac{\partial \mu_B}{\partial n_B} > 0$ and $\det(M) > 0$ for stability against small fluctuations. The results for the derivatives of the chemical potentials read

$$\frac{\partial \mu_F}{\partial n_F} = \frac{\epsilon_F}{n_F}\Big\{1 - \frac{1+b}{2b}\big[\frac{1}{2}A'(\eta) - \frac{1}{4}A''(\eta)\big]x + \frac{2}{b}\chi\big[D'(\eta) + \frac{1}{2}D''(\eta)\big]x^2\Big\}, \tag{3.86}$$

$$\frac{\partial \mu_B}{\partial n_B} = \frac{\epsilon_F}{n_F b}(2\chi + 3\chi^2 + 2\chi^3)\Big\{1 + 4D(\eta)\Big\}, \tag{3.87}$$

$$\frac{\partial \mu_B}{\partial n_F} = \frac{\partial \mu_B}{\partial n_F} = \frac{\epsilon_F}{n_F}\Big\{\frac{1+b}{2b}\big[A(\eta) - \frac{1}{2}A'(\eta)\big] - \frac{2}{b}(2\chi + \chi^2)D'(\eta)x\Big\}. \tag{3.88}$$

The first two stability conditions are easily satisfied, as explained in (3.3.2) and [9], while the condition on the determinant gives us the critical value $\chi_c$ for which the mixture is stable. The determinant of $M$ is a quartic in $\chi$

$$\det(M(\chi)) = \left(\frac{\epsilon_F}{n_F}\right)^2 \left[c_0 + c_1\chi + c_2\chi^2 + c_3\chi^3 + c_4\chi^4\right], \tag{3.89}$$

where the coefficients read

$$c_0 = -\left(\frac{1+b}{2b}\right)^2 \left(A - \frac{1}{2}A'\right)^2, \tag{3.90}$$

$$c_1 = \frac{2}{b}\left\{(1+4D) + \frac{1+b}{2b}\left[4D'\left(A - \frac{1}{2}A'\right) - \left(\frac{1}{2}A' - \frac{1}{4}A''\right)(1+4D)\right]x\right\}, \tag{3.91}$$

$$\begin{aligned} c_2 = \frac{1}{b}\Big\{&3(1+4D) + \frac{1+b}{2b}\left[4D'\left(A - \frac{1}{2}A'\right) - 3\left(\frac{1}{2}A' - \frac{1}{4}A''\right)(1+4D)\right]x \\ &+ \frac{4}{b}\left[(D' + \frac{1}{2}D'')(1+4D) - 4D'^2\right]x^2\Big\}, \end{aligned} \tag{3.92}$$

$$\begin{aligned} c_3 = \frac{2}{b}\Big\{&(1+4D) - \frac{1+b}{2b}\left(\frac{1}{2}A' - \frac{1}{4}A''\right)(1+4D)x \\ &+ \frac{1}{b}\left[3(D' + \frac{1}{2}2D'')(1+4D) - 8D'\right]x^2\Big\}, \end{aligned} \tag{3.93}$$

$$c_4 = \left(\frac{2}{b}\right)^2 \left[(D' + \frac{1}{2}2D'')(1 + 4D) - D'^2\right] x^2, \tag{3.94}$$

As expected the coefficient $c_0$ is always negative, which immediately shows that a minimum repulsion ($\chi \neq 0$) is needed in order to have $\det(M) > 0$.

The plots in Fig. 3.26 show the stability curve $\chi_c(\eta)$ for which $\det M(\chi_c) = 0$ for the two-dimensional Bose-Fermi mixture, both for the attractive and repulsive branches. Here, the mass ratio is fixed at $b = 1$ and different curves correspond to different boson-to-fermion concentration ratios $x$. The region of stability for the 2D B-F mixture is above the curve. In the attractive case, the curve initially grows with increasing $\eta$, exhibits a local maximum just beyond $\eta = 0$, then decreases slightly reaching a local minimum near $\eta \approx 1$, and eventually increases again indefinitely. This behaviour highlights a marked difference from the three-dimensional case: it is well-known that at large $\eta$ the mixture must eventually become stable, which the 3D LOCV curve correctly shows; however, the LOCV approach in 2D does not capture this stabilization at strong coupling, a limitation shared by other methods such as the T-matrix approach.

Interestingly, before the local minimum, the curve is generally higher for larger $x$, which is the opposite trend compared to the 3D scenario.

The repulsive branch in 2D instead behaves similarly to its 3D counterpart: the curves diverge as they approach the limit $\eta = 0$ from the right, and higher concentrations $x$ correspond to higher critical $\chi$ values.

Both plots reproduce the expected perturbative weak-coupling benchmark (to leading order), given by

$$\chi_c = \frac{1}{2\tilde{\eta}^2}\left(1 + \frac{1 - \ln 2}{\tilde{\eta}}\right)^2, \tag{3.95}$$

which is derived at the polaronic limit ($x \to 0$) and for equal masses ($b = 1$) [8], with the convention (2.12).

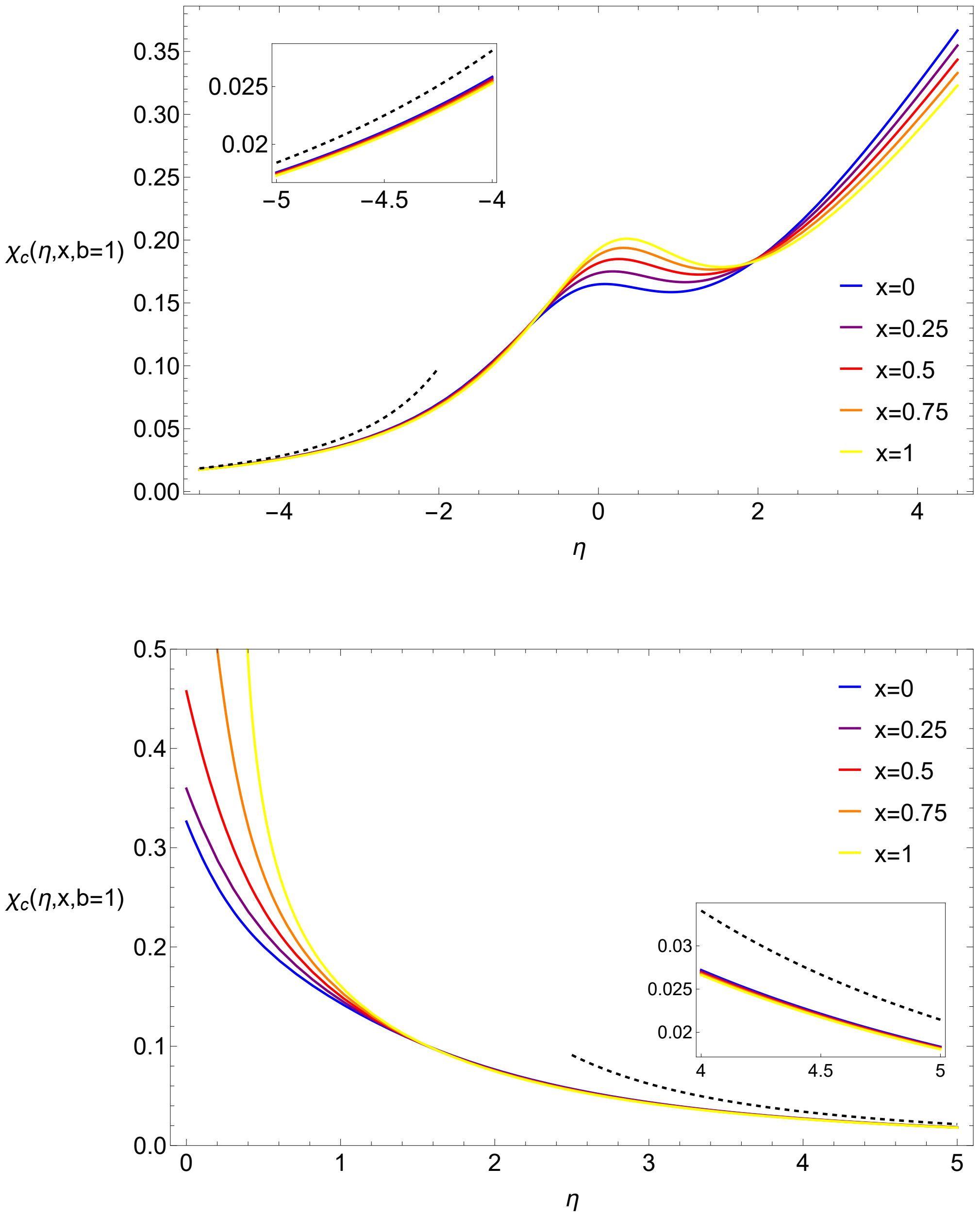

Figure 3.26: B-F stability curves for the critical boson-boson repulsion parameter $\chi_c$ in the attractive (top) and repulsive (bottom) regimes, plotted as functions of the interaction boson-fermion parameter $\eta = -\ln(a_{BF}k_F)$ for different values of the relative concentration of bosons $x$ and same masses $m_B = m_F$ ($b = 1$). The insets highlight weak coupling regions. The dashed curves show the weak coupling perturbative benchmark (3.95).

The next two plots in Fig. 3.27 display the critical value $\chi_c$ as a function of the mass ratio $b = m_B/m_F$ in the polaron limit ($x = 0$) for both the attractive and repulsive branches. Different curves correspond to different values of $\eta$. One observes a relatively flat minimum in the region around $b \approx 1$, indicating that the mixture tends to be more stable when the masses of the two species are similar. In both cases, the curves diverge as $b \to 0$ or $b \to \infty$, reflecting the increasing instability for very light or very heavy bosons relative to the fermions.

The next two plots in Fig. 3.28 show that, for equal concentrations ($x = 1$), the dependence of $\chi_c$ on the mass ratio $b$ remains similar: a broad minimum near $b \approx 1$ and divergence for large mass imbalance.

Finally, the last two plots in Fig. 3.29 illustrates the behaviour of $\chi_c$ as a function of the concentration ratio $x$ for fixed $b = 1$ and various $\eta$. The curves remain essentially flat throughout the range $x \in [0, 1]$, even more markedly than in the three-dimensional case, indicating that in two dimensions the mixture stability is only weakly influenced by the relative concentrations for $x < 1$.

This comprehensive set of results provides, for the first time within a variational non-perturbative framework, a detailed map of the stability conditions for two-dimensional Bose-Fermi mixtures. It highlights the peculiarities and limitations of the LOCV description in 2D and serves as a reference for future theoretical and experimental studies.

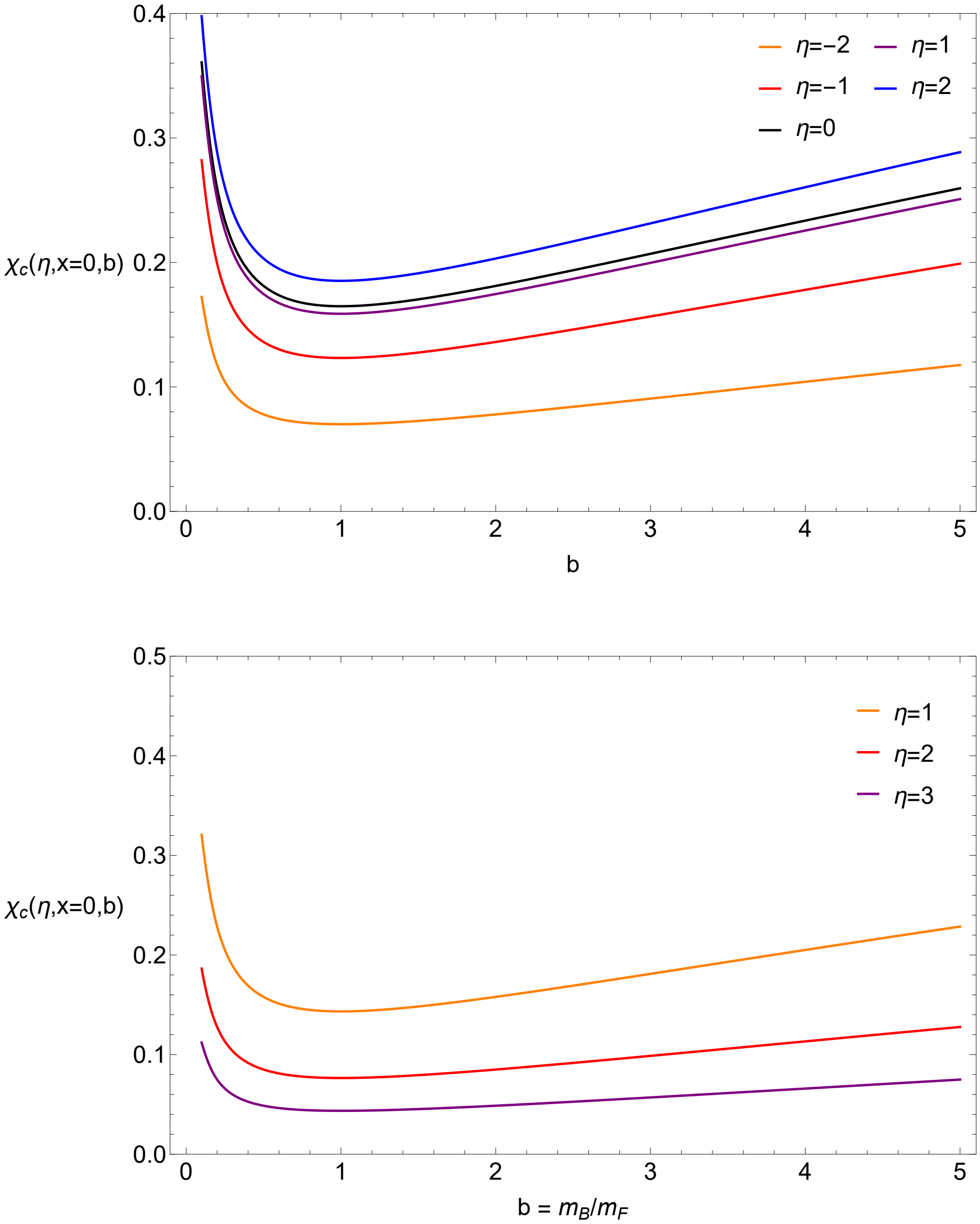

Figure 3.27: B-F stability curves for the critical boson-boson repulsion parameter $\chi_c$ in the attractive (top) and repulsive (bottom) regimes, plotted as functions of the boson to fermion mass ratio $b = \frac{m_B}{m_F}$ for different values of the interaction parameter $\eta$ in the polaron limit $x = 0$.

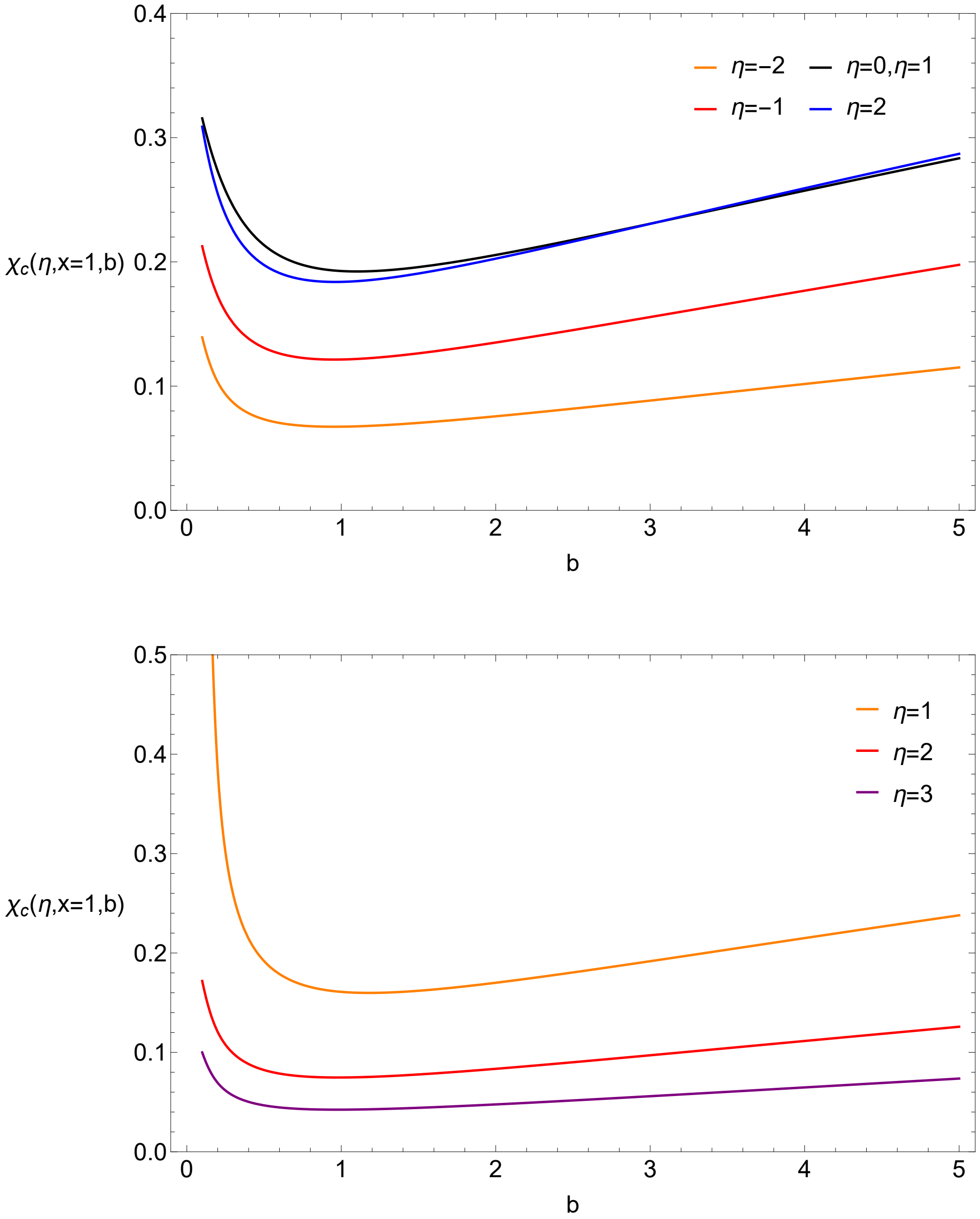

Figure 3.28: B-F stability curves for the critical boson-boson repulsion parameter $\chi_c$ in the attractive (top) and repulsive (bottom) regimes, plotted as functions of the boson to fermion mass ratio $b = \frac{m_B}{m_F}$ for different values of the interaction parameter $\eta$ with an equal concentration of bosons and fermions ($x = 1$).

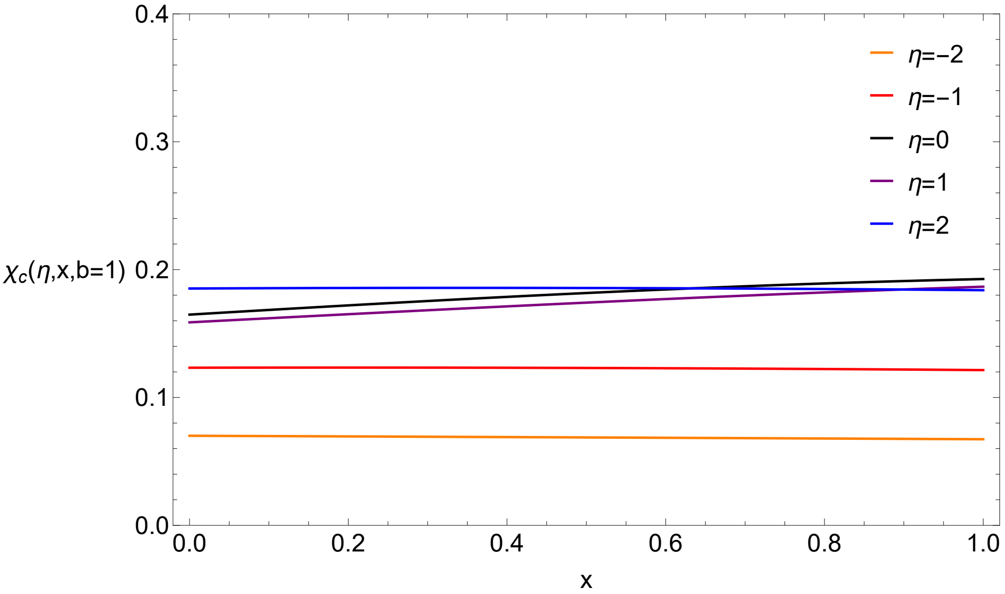

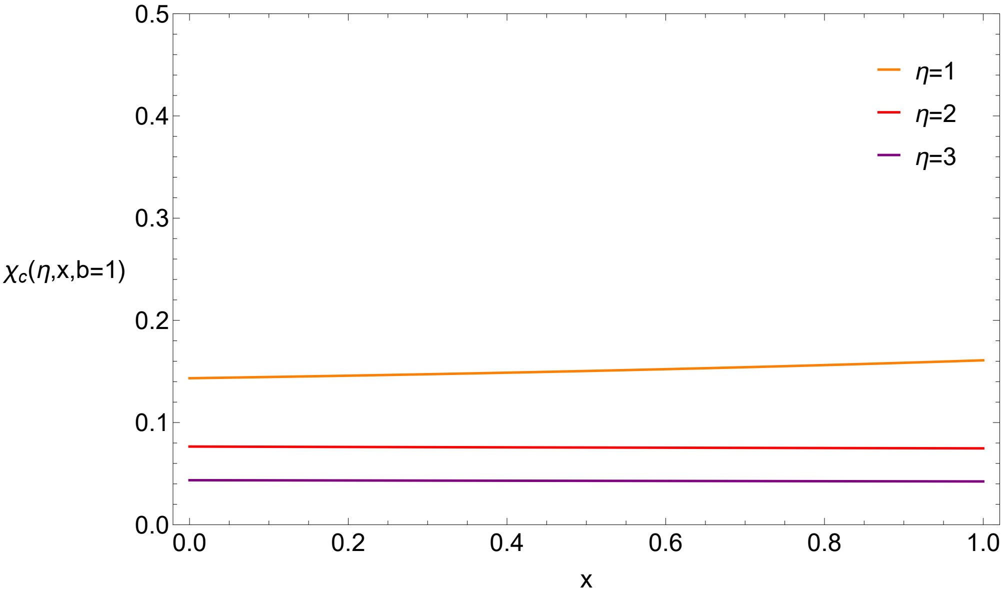

Figure 3.29: B-F stability curves for the critical boson-boson repulsion parameter $\chi_c$ in the attractive (top) and repulsive (bottom) regimes, plotted as functions of the boson to fermion concentration ratio $x = \frac{n_B}{n_F}$ for different values of the interaction parameter $\eta$ with same masses $m_B = m_F$ $(b = 1)$.

# Conclusions and Perspectives

In this thesis, we have carried out a comprehensive variational study of interacting Bose-Fermi mixtures, in three and two spatial dimensions, using the Lowest Order Constrained Variational (LOCV) method. This approach, well established in nuclear physics, has been adapted here to ultracold atomic gases, allowing us to capture two-body correlations beyond the perturbative regime.

In the three-dimensional scenario, we have verified the method's consistency with known results in the polaron limit of a single impurity and derived the stability conditions of the mixtures as a function of the interspecies interaction strength, the intraspecies boson-boson repulsion, the mass ratio, and the boson-to-fermion concentration. Our results reproduce the expected weak-coupling benchmarks and illustrate how stability depends on these parameters.

In two dimensions, a regime that has received much less attention in the literature, we have provided, to our knowledge, the first non-perturbative variational map of stability curves for two-dimensional Bose-Fermi mixtures. The results show good agreement with known perturbative limits at weak coupling but reveal intrinsic limitations of the LOCV framework at strong coupling, where the method does not fully capture the expected stabilization trend. As for the known three dimensional case, we find that the equal masses condition $m_B = m_F$ guarantees the maximum stability for a two dimensional Bose-Fermi mixture as well.

A notable strength of the LOCV method is its physical transparency: the correlation function clearly shows how the short-range behaviour and the healing length evolve with interaction strength, and dimensionality. However, this same structure also imposes constraints: by construction, the Jastrow-Slater ansatz used here cannot describe the actual formation of tightly bound Bose-Fermi molecules, as it only enforces pairwise correlations while keeping the particles as distinct entities.

Looking ahead, the LOCV description can be systematically improved. A first extension would include same-species correlation functions, one for fermion-fermion and one for boson-boson pairs, allowing the framework to better account for higher-order correlation effects and to approach the exact energy more accurately, especially in the strongly interacting regime, as highlighted in [22]. An even stronger promising direction would be to modify the variational ansatz itself, adopting a more flexible trial wave-function that explicitly allows the formation of Bose-Fermi molecular bound states, thereby bridging the gap between the atomic and molecular phase in a unified manner.

Overall, the results presented in this thesis provide a robust non-perturbative benchmark for understanding the stability and correlations of dilute Bose-Fermi mixtures across different dimensions and interaction regimes. They lay a foundation for more refined theoretical treatments and can guide future experimental explorations of strongly correlated quantum gases.

# Appendices

# Appendix A

# Slater rules

Expressing the many-body wave-function in terms of Slater determinants implies that, at some stage, one must evaluate matrix elements of the Hamiltonian and other operators between different determinants (in general). The systematic procedure for carrying out these calculations was developed by Slater and Condon and is now known as the *Slater–Condon rules.* For completeness, we briefly outline their derivation here.

Consider the Slater determinant

$$\|\Psi(x_1, x_2, \ldots, x_N)\| = \mathcal{A}\{a(x_1)b(x_2)\ldots c(x_N)\}, \tag{A.1}$$

expressed here with an antisymmetrizer $\mathcal{A} = \frac{1}{\sqrt{N!}}\sum_P \epsilon_P \mathcal{P}$ applied to single particle orthonormal spin orbitals

$$\langle a|a\rangle = \langle b|b\rangle = \ldots = \langle c|c\rangle\,, \quad \langle a|b\rangle = \langle a|c\rangle = \ldots = \langle b|c\rangle = 0. \tag{A.2}$$

Let's start by considering the simplest case, hence the norm of $\Psi$

$$\begin{aligned}\langle\Psi|\Psi\rangle =& \langle\mathcal{A}\{a(x_1)b(x_2)\ldots c(x_N)\}|\mathcal{A}\{a(x_1)b(x_2)\ldots c(x_N)\}\rangle \\ =& \langle\mathcal{A}ab\ldots c|\mathcal{A}ab\ldots c\rangle\end{aligned} \tag{A.3}$$

, since $\mathcal{A}$ is self-adjoint ($\mathcal{A} = \mathcal{A}^\dagger$) and satisfies $\mathcal{A}^2 = \sqrt{N!}\mathcal{A}$, we have

$$\begin{aligned}\langle\Psi|\Psi\rangle =& \big\langle ab\ldots c\big|\mathcal{A}^\dagger\mathcal{A}ab\ldots c\big\rangle = \big\langle ab\ldots c\big|\mathcal{A}^2 ab\ldots c\big\rangle \\ =& \sqrt{N!}\,\langle ab\ldots c|\mathcal{A}ab\ldots c\rangle = \langle ab\ldots c|\sum_P |\epsilon_P\mathcal{P}ab\ldots c\rangle\,.\end{aligned} \tag{A.4}$$

We then may expand the sum over permutations into classes consisting of zero transpositions (identity), single transpositions $ST$, double transpositions $DT$, triple transpositions $TT$, up to $n$ fold transpositions $NT$

$$\sum_P \epsilon_P \mathcal{P}ab\ldots c = ab\ldots c + ST + DT + \ldots + NT. \tag{A.5}$$

The identity or zero transposition contributes as

$$\langle ab\dots c|ab\dots c\rangle = \langle a|a\rangle \langle b|b\rangle \dots \langle c|c\rangle = 1, \tag{A.6}$$

while a particular $ST$, say $\mathcal{P}_{12}$, contributes as

$$\langle ab\dots c|ba\dots c\rangle = \langle a|b\rangle \langle b|a\rangle \dots \langle c|c\rangle = 0. \tag{A.7}$$

Indeed all $ST$, $DT$, etc will not contribute because a mismatch between the order on the right and on the left will result in an overlap between two orthogonal orbitals. So if the orbitals are orthonormal the Slater Determinant is normalized to 1.

Now consider the matrix element of an Hamiltonian $\langle\Psi|\, H\, |\Psi\rangle$, where the Hamiltonian

$$H = \sum_{i=1}^{N} f(i) + \sum_{i<j}^{N} g(i,j) = F + G \tag{A.8}$$

can be split in a sum of single-particle operators and a sum of two-particle operators. Since the antisymmetrizer commutes with the hamiltonian $[H, \mathcal{A}] = 0$, using (A.4) and (A.8) we have

$$\begin{aligned}\langle\Psi|\, H\, |\Psi\rangle &= \langle ab\dots c|\, H \sum_P |\epsilon_P \mathcal{P} ab\dots c\rangle \\ &= \langle ab\dots c|\, F \sum_P |\epsilon_P \mathcal{P} ab\dots c\rangle + \langle ab\dots c|\, G \sum_P |\epsilon_P \mathcal{P} ab\dots c\rangle .\end{aligned} \tag{A.9}$$

We will first evaluate the matrix element of the sum of one particle operators $F$. As above, we expand the sum over permutations into classes of transpositions

$$\langle\Psi|\, F\, |\Psi\rangle = \langle ab\dots c|\, F\, |ab\dots c + ST + DT + \dots + NT\rangle \tag{A.10}$$

and consider first the identity element

$$\begin{aligned}\langle ab\dots c| \sum_{i=1}^{n} f(i)\, |ab\dots c\rangle &= \langle a|\, f\, |a\rangle \langle b|b\rangle \dots \langle c|c\rangle + \langle a|a\rangle \langle b|\, f\, |b\rangle \dots \langle c|c\rangle + \dots \\ &\quad + \langle a|a\rangle \langle b|b\rangle \dots \langle c|\, f\, |c\rangle \\ &= \langle a|\, f\, |a\rangle + \langle b|\, f\, |b\rangle + \dots + \langle c|\, f\, |c\rangle .\end{aligned} \tag{A.11}$$

Considering again the single transposition term $\mathcal{P}_{12}$, we get

$$\begin{aligned}\langle ab\dots c| \sum_{i=1}^{N} f(i)\, |ba\dots c\rangle &= \langle a|\, f\, |b\rangle \langle b|a\rangle \dots \langle c|c\rangle + \langle a|b\rangle \langle b|\, f\, |a\rangle \dots \langle c|c\rangle + \dots \\ &\quad + \langle a|b\rangle \langle b|a\rangle \dots \langle c|\, f\, |c\rangle\end{aligned} \tag{A.12}$$

Clearly there is always a mismatch and since the overlap $\langle a|b\rangle = 0$, the contribution of $\mathcal{P}_{12}$ vanishes. In a similar fashion all matrix elements involving $ST$, $DT$, etc vanish. So the expectation value of the sum of one particle operators $F = \sum_{i=1}^{N} f(i)$ is given by

$$\langle\Psi|\, F\, |\Psi\rangle = \langle a|\, f\, |a\rangle + \langle b|\, f\, |b\rangle + \ldots + \langle c|\, f\, |c\rangle\,. \tag{A.13}$$

In general the expectation value of a sum of one-particle operators is the sum of the expectation values of the individual operators with respect to the elements of the Slater Determinant. By repeating the same calculation for the sum of two-particle operators $G = \sum_{i<j}^{N} g(i,j)$, one finds that the single transposition terms now indeed contribute and we have

$$\begin{aligned}\langle\Psi|\, G\, |\Psi\rangle = &\langle ab\ldots c|\sum_{i<j}^{N} g(i,j)\,|ab\ldots c + ST\rangle = \langle ab|\, g(1,2)(1-\mathcal{P}_{12})\,|ab\rangle + \ldots \\ &+ \langle ac|\, g(1,2)(1-\mathcal{P}_{12})\,|ac\rangle + \ldots + \langle bc|\, g(1,2)(1-\mathcal{P}_{12})\,|bc\rangle\,,\end{aligned} \tag{A.14}$$

while double, triple etc transposition terms still give zero. So by labelling the Slater determinant $\Psi$ using a general set of orthonormal spin orbitals $\{\varphi_i\}$

$$\Psi(1,2,\ldots,n) = \mathcal{A}\varphi_1(1)\varphi_2(2)\ldots\varphi_N(N), \tag{A.15}$$

we can write the matrix elements of the Hamiltonian $H$ as

$$\langle\Psi|\, H\, |\Psi\rangle = \sum_{i=1}^{N}\langle\varphi_i|\, f\, |\varphi_i\rangle + \sum_{i<j}^{N}\langle\varphi_i(1)\varphi_j(2)|\, g(1,2)(1-\mathcal{P}_{12})\,|\varphi_i(1)\varphi_j(2)\rangle \tag{A.16}$$

# Appendix B

# Special functions

## B.1 Bessel functions

In various parts of this work, solutions to radial differential equations naturally involve Bessel functions. Here, we briefly summarize the definitions and key properties of the Bessel functions of the first and second kind, as well as their modified counterparts.

The Bessel functions of the first kind $J_\alpha(x)$, and the second kind $Y_\alpha(x)$, are solutions to Bessel's differential equation:

$$x^2\frac{d^2y}{dx^2} + x\frac{dy}{dx} + (x^2 - \alpha^2)y = 0. \tag{B.1}$$

The function $J_\alpha(x)$ is finite at the origin for non-negative integer orders $\alpha$, while $Y_\alpha(x)$ (also called Neumann or Weber functions) represents the second linearly independent solution, which is singular at the origin.

Bessel functions appear frequently in problems with cylindrical or spherical symmetry, such as the radial part of the free-particle Schrödinger equation in two and three dimensions.

The Bessel functions of the first kind $J_\alpha(x)$ can be represented with the following series

$$J_\alpha(x) = \sum_{m=0}^{\infty} \frac{(-1)^m}{m!\Gamma(m+\alpha+1)} \left(\frac{x}{2}\right)^{2m+\alpha}, \tag{B.2}$$

or for integer values $\alpha = n \in \mathbb{N}$ via the Hansen-Bessel integral representation

$$J_n(x) = \frac{1}{\pi}\int_0^\pi d\tau \cos(n\tau - x\sin\tau). \tag{B.3}$$

For non-integer $\alpha$ the Bessel functions of the second kind $Y_\alpha(x)$ are related to $J_\alpha(x)$

by

$$Y_\alpha(x) = \frac{J_\alpha(x)\cos(\alpha\pi) - J_{-\alpha}(x)}{\sin(\alpha\pi)} \tag{B.4}$$

and for the case of integer $\alpha = n \in \mathbb{N}$ the function is defined by taking the limit as $\alpha$ tends to $n$

$$Y_n(x) = \lim_{\alpha \longrightarrow n} Y_\alpha(x) \tag{B.5}$$

### B.1.1 Hankel functions

Using the Bessel functions one can formulate two linearly independent solutions of the Bessel equation (B.1) via the Hankel functions of the first and second kind, defined repectively as

$$H_\alpha^{(1)} = J_\alpha(x) + iY_\alpha(x), \tag{B.6}$$

$$H_\alpha^{(2)} = J_\alpha(x) - iY_\alpha(x). \tag{B.7}$$

These linear combinations are also known as Bessel functions of the third kind.

### B.1.2 Modified Bessel functions

The modified Bessel functions of the first kind $I_\alpha(x)$, and the second kind $K_\alpha(x)$, are solutions to the modified Bessel equation:

$$x^2\frac{d^2y}{dx^2} + x\frac{dy}{dx} - (x^2 + \alpha^2)y = 0. \tag{B.8}$$

Unlike $J_\alpha$ and $Y_\alpha$, which oscillate for large arguments, the modified Bessel functions exhibit exponential growth $(I_\alpha(x))$ or decay $(K_\alpha(x))$ for real positive arguments. These functions naturally arise in problems with radial symmetry in imaginary or purely decaying contexts, such as the two-dimensional bound-state solutions discussed in this thesis.

The modified Bessel functions are related to the Bessel functions, for $-\pi < \arg(x) \leq \frac{\pi}{2}$, we have

$$J_\alpha(ix) = e^{\frac{\alpha\pi i}{2}} I_\alpha(x), \tag{B.9}$$

$$Y_\alpha(ix) = e^{\frac{(1+\alpha)\pi i}{2}} I_\alpha(x) - \frac{2}{\pi} e^{\frac{-\alpha\pi i}{2}} K_\alpha(x). \tag{B.10}$$

### B.1.3 Relation to the 2D LOCV equation

The free version of the Euler-Lagrange equation (3.54) in cartesian coordinates reads

$$-\frac{1}{2m_r}\left(\frac{\partial^2}{\partial x_1^2} + \frac{\partial^2}{\partial x_2^2}\right) f(x) = \lambda f(x), \tag{B.11}$$

for a spherically symmetric $f(x) = f(r)$ it can be rewritten in 2D polar coordinates as

$$-\frac{1}{2m_r}\left(\frac{\partial^2}{\partial r^2} + \frac{1}{r}\frac{\partial}{\partial r}\right) f(r) = \lambda f(r). \tag{B.12}$$

Now for $\lambda > 0$ we set $\kappa^2 = 2m_r\lambda > 0$ and we get the equation

$$f'' + \frac{1}{r}f' + \kappa^2 f = 0, \tag{B.13}$$

whose solutions corresponds to the Bessel functions $J_0(\kappa r)$ and $Y_0(\kappa r)$.

For $\lambda < 0$ we instead set $k^2 = -2m_r\lambda > 0$ and we get the equation

$$f'' + \frac{1}{r}f' - k^2 f = 0, \tag{B.14}$$

whose solutions corresponds to the modified Bessel functions $I_0(kr)$ and $K_0(kr)$.

The sign of the pair energy $\lambda$ determines which type of Bessel function appears in the free region. For the repulsive branch, where the solution represents a scattering state with positive energy ($\lambda > 0$), the radial equation reduces to the ordinary Bessel equation, and the solution is expressed in terms of oscillatory Bessel functions $J_0$ and $Y_0$.

In contrast, for the attractive branch, the pair energy is negative ($\lambda < 0$), indicating a bound state. In this case, the radial equation becomes the modified Bessel equation, and the physically acceptable solution is given in terms of the modified Bessel functions $I_0$ and $K_0$. The function $K_0$ ensures the proper exponential decay at large distances, consistent with the localized nature of the bound pair.

### B.1.4 Asymptotic Behaviours

For reference, the leading asymptotic forms for large arguments are:

$$J_\alpha(x) \sim \sqrt{\frac{2}{\pi x}} \cos\left(x - \frac{\alpha\pi}{2} - \frac{\pi}{4}\right), \quad Y_\alpha(x) \sim \sqrt{\frac{2}{\pi x}} \sin\left(x - \frac{\alpha\pi}{2} - \frac{\pi}{4}\right), \quad x \to \infty, \tag{B.15}$$

and

$$I_\alpha(x) \sim \frac{e^x}{\sqrt{2\pi x}}, \quad K_\alpha(x) \sim \sqrt{\frac{\pi}{2x}} e^{-x}, \quad x \to \infty. \tag{B.16}$$

These approximations are useful for analysing the behaviour of wave-functions in the asymptotic limits, very useful for the formulation of the scattering theory.

## B.2 Meijer G Function

The Meijer G-function which is a very general function intended to include most of the known special functions as particular cases

$$G_{p,q}^{m,n}\left(\begin{matrix} a_1, \dots, a_p \\ b_1, \dots, b_q \end{matrix} \middle| \, z \right) = \frac{1}{2\pi i} \int_L ds \frac{\prod_{j=1}^{m} \Gamma(b_j - s) \prod_{j=1}^{n} \Gamma(1 - a_j + s)}{\prod_{j=m+1}^{q} \Gamma(1 - b_j + s) \prod_{j=n+1}^{p} \Gamma(a_j - s)} z^s, \tag{B.17}$$

Where the $L$ in the integral represents the path to be followed while integrating and $\Gamma(s)$ is the gamma function, a shifted generalization of the factorial function to non-integer values. Three choices are possible for the path $L$ however the details are out of the scope of this thesis work, for more informations on this topic check [37].

# Bibliography

[1] C. J. Pethick and H. Smith. *Bose–Einstein Condensation in Dilute Gases.* Cambridge University Press, 2 edition, 2008.

[2] A.L. Fetter and J.D. Walecka. *Quantum Theory of Many-particle Systems.* Dover Books on Physics. Dover Publications, 2003.

[3] Cheng Chin, Rudolf Grimm, Paul Julienne, and Eite Tiesinga. Feshbach resonances in ultracold gases. *Rev. Mod. Phys.*, 82:1225–1286, Apr 2010.

[4] H.T.C. Stoof, D.B.M. Dickerscheid, and K. Gubbels. *Ultracold Quantum Fields.* Theoretical and Mathematical Physics. Springer Netherlands, 2014.

[5] Zeng-Qiang Yu, Shizhong Zhang, and Hui Zhai. Stability condition of a strongly interacting boson-fermion mixture across an interspecies Feshbach resonance. *Phys. Rev. A*, 83:041603, Apr 2011.

[6] G. Bertaina, E. Fratini, S. Giorgini, and P. Pieri. Quantum Monte Carlo Study of a Resonant Bose-Fermi Mixture. *Phys. Rev. Lett.*, 110:115303, Mar 2013.

[7] Marcel Duda, Xing-Yan Chen, Andreas Schindewolf, Roman Bause, Jonas von Milczewski, Richard Schmidt, Immanuel Bloch, and Xin-Yu Luo. Transition from a polaronic condensate to a degenerate Fermi gas of heteronuclear molecules. *Nature Physics*, 19(5):720–725, February 2023.

[8] Jacopo D'Alberto, Lorenzo Cardarelli, Davide Emilio Galli, Gianluca Bertaina, and Pierbiagio Pieri. Quantum Monte Carlo and perturbative study of two-dimensional Bose-Fermi mixtures. *Physical Review A*, 109(5), May 2024.

[9] Christian Gualerzi, Leonardo Pisani, and Pierbiagio Pieri. Mechanical stability of resonant Bose-Fermi mixtures, 2025. arXiv:2504.06681 [cond-mat.quant-gas].

[10] John R. Taylor. *Scattering Theory: The Quantum Theory of Nonrelativistic Collisions.* John Wiley and Sons, New York, 1972.

[11] Giancarlo Calvanese Strinati, Pierbiagio Pieri, Gerd Röpke, Peter Schuck, and Michael Urban. The bcs–bec crossover: From ultra-cold fermi gases to nuclear systems. *Physics Reports*, 738:1–76, 2018. The BCS–BEC crossover: From ultra-cold Fermi gases to nuclear systems.

[12] Andrea Guidini, Gianluca Bertaina, Davide Emilio Galli, and Pierbiagio Pieri. Condensed phase of Bose-Fermi mixtures with a pairing interaction. *Phys. Rev. A*, 91:023603, Feb 2015.

[13] S. Y. Chang, V. R. Pandharipande, J. Carlson, and K. E. Schmidt. Quantum Monte Carlo studies of superfluid Fermi gases. *Phys. Rev. A*, 70:043602, Oct 2004.

[14] G. E. Astrakharchik, J. Boronat, J. Casulleras, Giorgini, and S. Equation of State of a Fermi Gas in the BEC-BCS Crossover: A Quantum Monte Carlo Study. *Phys. Rev. Lett.*, 93:200404, Nov 2004.

[15] S. Pilati, J. Boronat, J. Casulleras, and S. Giorgini. Quantum Monte Carlo simulation of a two-dimensional Bose gas. *Phys. Rev. A*, 71:023605, Feb 2005.

[16] S. Pilati, G. Bertaina, S. Giorgini, and M. Troyer. Itinerant Ferromagnetism of a Repulsive Atomic Fermi Gas: A Quantum Monte Carlo Study. *Phys. Rev. Lett.*, 105:030405, Jul 2010.

[17] V.R. Pandharipande. Dense neutron matter with realistic interactions. *Nuclear Physics A*, 174(3):641–656, 1971.

[18] V.R. Pandharipande. Hyperonic matter. *Nuclear Physics A*, 178(1):123–144, 1971.

[19] Robert Jastrow. Many-Body Problem with Strong Forces. *Phys. Rev.*, 98:1479–1484, Jun 1955.

[20] S. Cowell, H. Heiselberg, I. E. Mazets, J. Morales, V. R. Pandharipande, and C. J. Pethick. Cold Bose Gases with Large Scattering Lengths. *Phys. Rev. Lett.*, 88:210403, May 2002.

[21] Henning Heiselberg. Bosons and fermions near Feshbach resonances. *Journal of Physics B: Atomic, Molecular and Optical Physics*, 37(7):S141–S153, March 2004.

[22] S. Y. Chang and V. R. Pandharipande. Ground-State Properties of Fermi Gases in the Strongly Interacting Regime. *Phys. Rev. Lett.*, 95:080402, Aug 2005.

[23] Kerson Huang. *Statistical Mechanics.* John Wiley & Sons, 2 edition, 1987.

[24] Sadhan Adhikari. Quantum scattering in two dimensions. *American Journal of Physics - AMER J PHYS*, 54, 04 1986.

[25] T. M. Whitehead, L. M. Schonenberg, N. Kongsuwan, R. J. Needs, and G. J. Conduit. Pseudopotential for the two-dimensional contact interaction. *Phys. Rev. A*, 93:042702, Apr 2016.

[26] Bethe, H. and Peierls, R. Quantum Theory of the Diplon. *Proceedings of the Royal Society of London Series A*, 148(863):146–156, January 1935.

[27] E. Krotscheck. Variational problem in Jastrow theory. *Phys. Rev. A*, 15:397–407, Jan 1977.

[28] V. R. Pandharipande and H. A. Bethe. Variational Method for Dense Systems. *Phys. Rev. C*, 7:1312–1328, Apr 1973.

[29] C. Lobo, A. Recati, S. Giorgini, and S. Stringari. Normal State of a Polarized Fermi Gas at Unitarity. *Phys. Rev. Lett.*, 97:200403, Nov 2006.

[30] L. Cardarelli. Ground-state properties of dilute Bose-Fermi mixtures in two and three dimensions. Master's thesis, Università degli Studi di Camerino, 2014.

[31] F. Scazza, G. Valtolina, P. Massignan, A. Recati, A. Amico, A. Burchianti, C. Fort, M. Inguscio, M. Zaccanti, and G. Roati. Repulsive Fermi Polarons in a Resonant Mixture of Ultracold $^6$Li Atoms. *Phys. Rev. Lett.*, 118:083602, Feb 2017.

[32] M.L. Ristig, P.M. Lam, and J.W. Clark. Condensate fraction and momentum distribution of liquid helium. *Physics Letters A*, 55(2):101–103, 1975.

[33] Wolfram Research, Inc. *Mathematica, Version 14.2.* Wolfram Research, Inc., Champaign, Illinois, USA, 2024. `https://www.wolfram.com/mathematica/`.

[34] S. Pilati, G. Orso, and G. Bertaina. Quantum Monte Carlo simulations of two-dimensional repulsive Fermi gases with population imbalance. *Phys. Rev. A*, 103:063314, Jun 2021.

[35] Marco Koschorreck, Daniel Pertot, Enrico Vogt, Bernd Fröhlich, Michael Feld, and Michael Köhl. Attractive and repulsive Fermi polarons in two dimensions. *Nature*, 485(7400):619–622, May 2012.

[36] M. Schick. Two-Dimensional System of Hard-Core Bosons. *Phys. Rev. A*, 3:1067–1073, Mar 1971.

[37] Erdélyi, Arthur and Magnus, Wilhelm and Oberhettinger, Fritz and Tricomi, Francesco G. *Higher Transcendental Functions. Vol. I.* McGraw-Hill Book Company, Inc., New York-Toronto-London, 1953.

[38] S. Giorgini, J. Boronat, and J. Casulleras. Ground state of a homogeneous Bose gas: A diffusion Monte Carlo calculation. *Phys. Rev. A*, 60:5129–5132, Dec 1999.

[39] David J. Griffiths and Darrell F. Schroeter. *Introduction to quantum mechanics.* Cambridge University Press, Cambridge ; New York, NY, third edition edition, 2018.

[40] Francesco Scazza, Matteo Zaccanti, Pietro Massignan, Meera M. Parish, and Jesper Levinsen. Repulsive Fermi and Bose Polarons in Quantum Gases. *Atoms*, 10(2):55, May 2022.

[41] S. Fantoni. Momentum Distribution of Boson and Fermion Systems in Jastrow Theory. *Nuovo Cim. A*, 44:191, 1978.

[42] Jesper Levinsen and Meera M. Parish. *Strongly interacting two-dimensional Fermi gases*, page 1–75. World Scientific, March 2015.

[43] Krzysztof Gawryluk and Mirosław Brewczyk. Mechanism for sound dissipation in a two-dimensional degenerate Fermi gas. *Scientific Reports*, 14(1), May 2024.

[44] Henning Heiselberg. *Crossovers in Unitary Fermi Systems*, page 49–97. Springer Berlin Heidelberg, October 2011.

[45] Raúl Bombín, Tommaso Comparin, Gianluca Bertaina, Ferran Mazzanti, Stefano Giorgini, and Jordi Boronat. Two-dimensional repulsive Fermi polarons with short- and long-range interactions. *Phys. Rev. A*, 100:023608, Aug 2019.

[46] Chang, Soon-Yong and Randeria, Mohit and Trivedi, Nandini. Ferromagnetism in the upper branch of the feshbach resonance and the hard-sphere fermi gas. *Proceedings of the National Academy of Sciences*, 108:51–54, 01 2011.

[47] Cosetta Baroni, Bo Huang, Isabella Fritsche, Erich Dobler, Gregor Anich, Emil Kirilov, Rudolf Grimm, Miguel A. Bastarrachea-Magnani, Pietro Massignan, and Georg M. Bruun. Mediated interactions between Fermi polarons and the role of impurity quantum statistics. *Nature Physics*, 20(1):68–73, October 2023.

[48] Edward Taylor, Shizhong Zhang, William Schneider, and Mohit Randeria. Colliding clouds of strongly interacting spin-polarized fermions. *Phys. Rev. A*, 84:063622, Dec 2011.

[49] Fumiaki Iwamoto and Masami Yamada. Cluster Development Method in the Quantum Mechanics of Many Particle System, II: Saturation of Nuclear Forces. *Progress of Theoretical Physics*, 18(4):345–356, 10 1957.

[50] G. Bertaina and S. Giorgini. BCS-BEC Crossover in a Two-Dimensional Fermi Gas. *Physical Review Letters*, 106(11), March 2011.

[51] H. Heiselberg. Itinerant ferromagnetism in ultracold Fermi gases. *Phys. Rev. A*, 83:053635, May 2011.

[52] Peng Zhang, Long Zhang, and Youjin Deng. Modified Bethe-Peierls boundary condition for ultracold atoms with spin-orbit coupling. *Physical Review A*, 86(5), November 2012.

[53] Piotr T. Grochowski, Tomasz Karpiuk, Mirosław Brewczyk, and Kazimierz Rzążewski. Breathing Mode of a Bose-Einstein Condensate Immersed in a Fermi Sea. *Phys. Rev. Lett.*, 125:103401, Sep 2020.

[54] S. Pilati and S. Giorgini. Phase Separation in a Polarized Fermi Gas at Zero Temperature. *Phys. Rev. Lett.*, 100:030401, Jan 2008.

[55] Milton Abramowitz and Irene A. Stegun. *Handbook of Mathematical Functions with Formulas, Graphs, and Mathematical Tables*. Dover, New York, ninth dover printing, tenth gpo printing edition, 1964.

[56] P G Averbuch. Zero energy divergence of scattering cross sections in two dimensions. *Journal of Physics A: Mathematical and General*, 19(12):2325, aug 1986.